Inclusive Neutron Analysis in MIPP Experiment

a technical report on the neutron analysis

Turgun Nigmanov, Michael Longo, Durga Rajaram, Dick Gustafson

University of Michigan

May 11, 2010

Abstract

We demonstrate that the Main Injector Particle Production (MIPP) experiment has the ability to detect neutrons with good energy resolution [1]. The most comprehensive measurements of inclusive neutron production cross sections were recently made by the NA49 collaboration using pp collisions at 158 GeV/c [2]. Using the Fermilab Main Injector proton beam we study the neutron production spectra at 58 GeV/c and 120 GeV/c with liquid hydrogen, beryllium, carbon, bismuth and uranium targets. This note describes the detailed analysis procedure for inclusive neutron production cross section measurements using data from the MIPP experiment.

Contents

1 Introduction

The neutron analysis is based on MIPP experimental data processed with MIPP software release "pass4f".

2 Interaction Targets

The target properties shown on Table 1.

name	A	d, cm	m, g	AD, g/cm^2	IL, %	$n_t \times 10^{23}$cm^{-2}	ρ(db)	ρ(MC)
H_2 liquid	1.008	14.0		0.991		5.922		
Beryllium	9.012	0.399	14.4	0.71	0.94	0.4744	1.779	1.848
Carbon	12.011	1.003	34.0	1.677	1.94	0.8408	1.672	2.000
Bismuth	208.98	0.173	34.25	1.69	0.87	0.0487	9.769	9.780
Uranium	238.03	0.1	38	1.875	?	0.0474	18.75	18.95

Table 1: The targets and their properties, where d - thickness in cm, m - mass in g, AD - areal density in g/cm^2, IL - interaction length and n_t is a number of nucleus per cm^2.

The n_t quantity in Table was calculated as:

$$n_t = \frac{N_A \times density \times thickness}{A},$$

where N_A is Avogadro number, density $\times$ thickness is an areal density AD and A is a target atomic weight.

Figure 1 shows the nuclear target positions within the "target wheel" vs run number for 58 GeV/c (on left) and 120 GeV/c (on right) data.

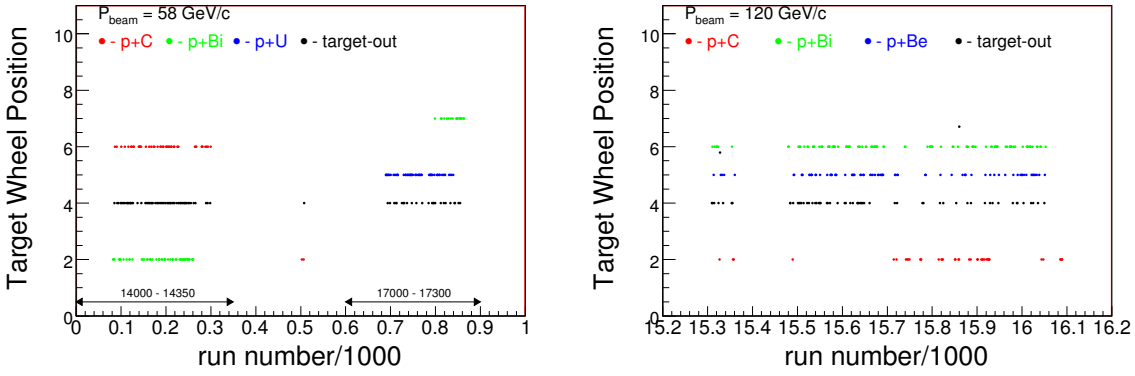

Figure 1: The nuclear target positions within the "target wheel" vs run number for 58 GeV/c (on left) and 120 GeV/c (on right) data.

3 Event Selection

The neutron analysis was done using a "good" event sample. It means that each event should pass some preliminary conditions:

- No more than 30 tracks per event
- EMCAL and HCAL detectors status should have readout
- "Good" beam track
- Trigger scintillator is on
- Use events with reliable tracking conditions

Each event was tested for "clean" conditions: no more than 30 tracks and valid EMCAL and HCAL status. We used data when "SciHi" scintillator trigger was available and it's conditions (HV, threshold) were stabilized. According to [3] such conditions are started from run number 13267. Efficiencies for each above mentioned cuts are summarized in Tables 3 and 4.

3.1 Selection of "good" beam track

The beam track selection was done according to following criteria:

- Use events with single beam track
- Reduce unreconstructed second beam tracks: nBeamCrossings$\leq$4
- Apply beam track time cut
- Use beam track segment "xbc3[3]" and track slopes
- Project it to Z_{tgt} and apply a specific spot size cut depending on the target type and beam momenta
- Beam divergence cut

The proton beam track time distributions are presented in Figure 2 for 58 GeV/c and 120 GeV/c momenta. Plots clearly shows the presence of the bucket structure, with about 19 ns separation and half width of 9.5 ns. Buckets closest to central bucket are at -12 ns and at 24 ns. Hence we set cuts at -2 ns and at 15 ns.

The fraction of events when the beam track is off-time is 2.5%. The time gates for the tracking system and calorimeters are wider than for the BC1-3 beam chambers. Hence the actual contribution to the neutron candidates from other buckets might be more significant.

Selection of the transverse position cut for the incident beam is based on the beam spot at the center of the target. This is a good approach for the thin target data. But

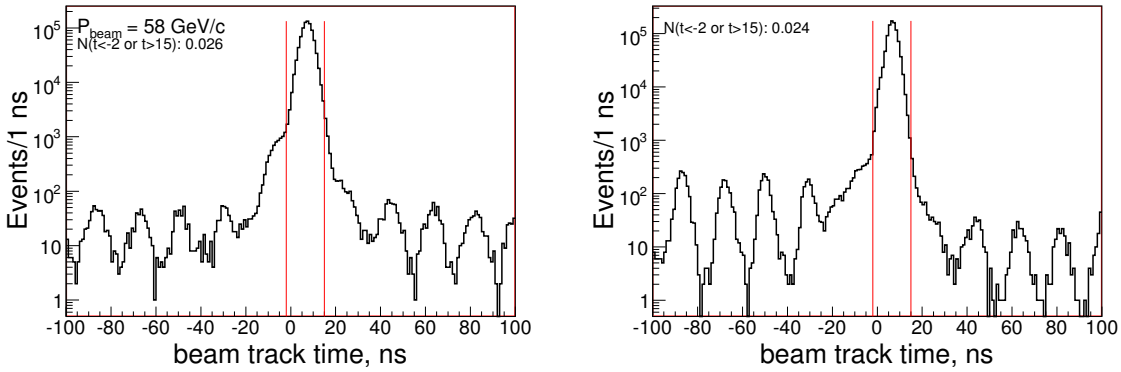

Figure 2: The beam track time distributions for 58 GeV/c (on left) and for 120 GeV/c protons (on right). The time info is based on the beam chambers. The red lines illustrate the selected time cut: time should be within -2 ns $< t <$ 15 ns.

for the liquid hydrogen data we need to follow the LH2 tube position and its radius. We also found that part of the transport pipes are shadowing the LH2 volume. For the shadowed area we might expect that the beam track with some probability might interact with pipe and disappear. Then the incident beam might be overestimated. The best solution is to drop the beam tracks in this area. The details on this matter are described in Appendix A.

In order to calculate the beam spot we used the beam track segment "xbc3" and its slopes. We assumed that these parameters are less biased to the tracks downstream of the target. The beam positions shown in Figure 3 for 58 GeV/c and in Figure 5 for 120 GeV/c protons at Z of the thin target. The red lines show what was selected as the beam spot center, (X_o and Y_o). We used a cut of R $\leq$ 2.0 cm for 58 GeV/c and R $\leq$ 0.8 cm for 120 GeV/c beam, in order to eliminate the beam halo. This cut drops about 3% of events (using 120 GeV/c). The beam spot position for 58 GeV/c data was considered as run dependent (see Fig. 6).

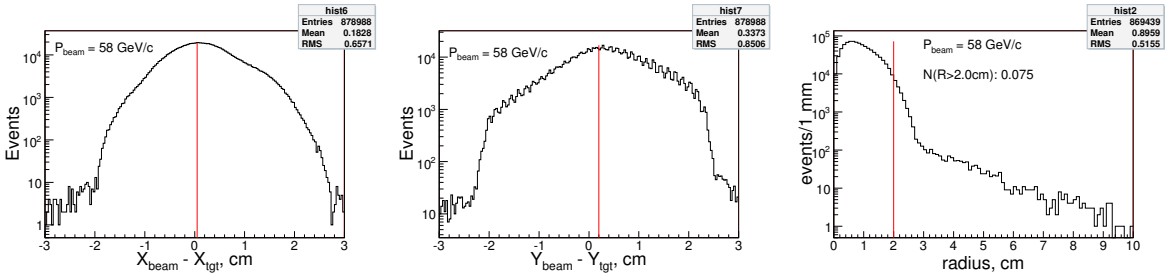

Figure 3: The beam track position distributions at Z of thin target using 58 GeV/c protons. The red lines on left and in middle plots illustrate the average beam spot center, X_o and Y_o. The right plot shows the distance between target center and the position of the particle. The red line there shows the radius cut position.

The 58 GeV/c beam divergences shown in Figure 4.

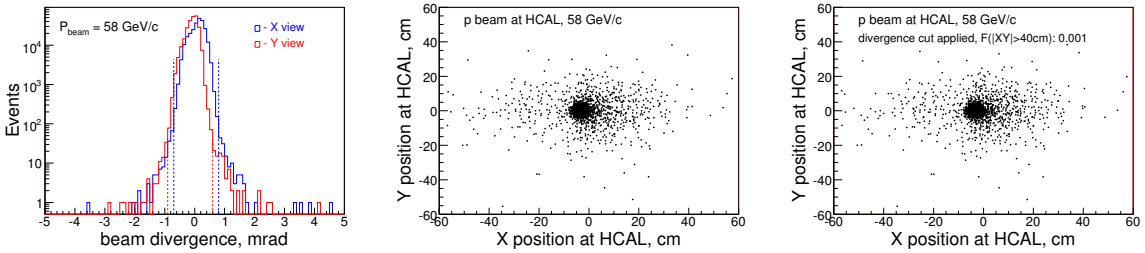

Figure 4: Left plot: the beam track divergence distributions for 58 GeV/c protons. Middle plot: track projections at HCAL for beam triggers and single track events. Right plot: same as on middle except that the divergence cut applied: from -0.7 up to 0.8 mrad in X-view and from -0.9 up to 0.6 mrad in Y-view.

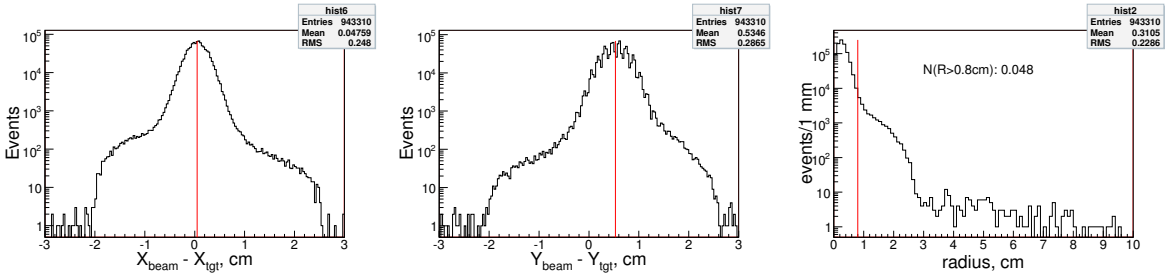

Figure 5: The beam track position distributions at Z of carbon (2%) target using 120 GeV/c protons. The red lines on left and in middle plots illustrate the selected beam spot center, X_o and Y_o. The right plot shows the distance between beam center and the position of the particle. The red line there shows the radius cut position.

Selected beam spot centers (X_o,Y_o) and radius values for the different beam settings and targets are presented in Table 2.

The beam track transverse position and the width variations at the Z Z_{tgt} vs run number presented in Figure 6. So, we required that both distances: from the beam mean position up to the particle and particles distance from the beam axis should be less than 2.0 cm.

3.2 Trigger Scintillator

Our neutron analysis would be based on the trigger scintillator. Figure 7 illustrates the scintillator trigger behavior vs the run number.

The left plot in Fig. 7 is "SciHi" rate vs run number for 58 GeV/c data, right plot - for 120 GeV/c data. By viewing "SciHi" rates we conclude that some runs are not useful for the neutron analysis: runs where rate is equal to 0 or below of the

beam momentum	X_o,cm	$Y_o$cm	Radius, cm	ϵ_{beam}
58 GeV/c, LH				
58 GeV/c, thin	0.05	-0.2	2.0	0.92
84 GeV/c, LH				
120 GeV/c, thin	0.05	0.53	0.8	0.95

Table 2: Selected spot center (X_o,Y_o) and radius values used as the transverse position cut for counting of incident protons. Last column represents the combined efficiency of the beam track time, divergence and radius cuts.

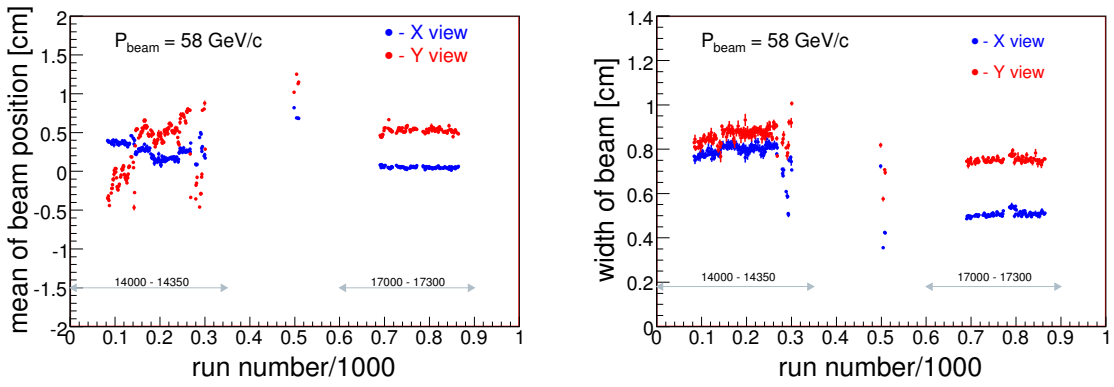

Figure 6: The beam track transverse position (on left) and width (on right) distributions vs run number at Z of thin target using 58 GeV/c protons.

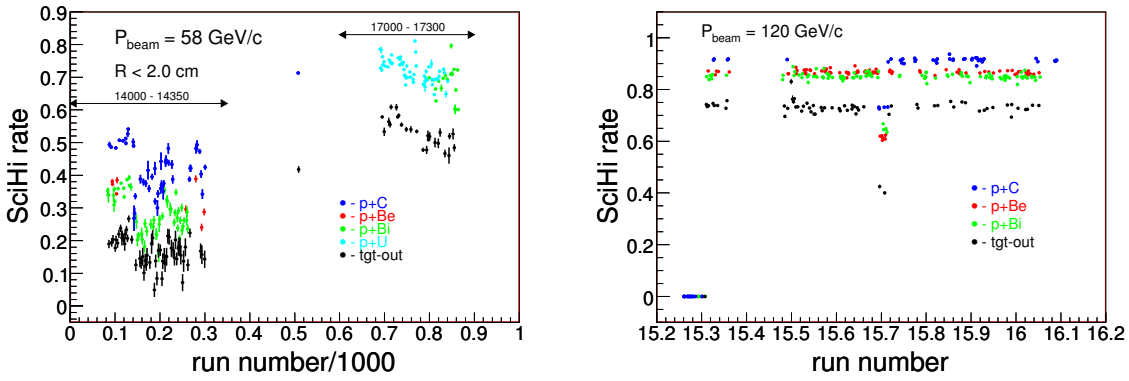

Figure 7: "SciHi" fires normalized per single proton interaction vs the run number: at 58 GeV/c (on left) and at 120 GeV/c (on right).

respective band. For 58 GeV/c data (left plot) we see that "SciHI" rate in run range between 14060 and 14300 are systematically lower by at least factor of 2 than for data with runs above 17000. What is a reason for that? Study shows that if we require a reasonable Z cut on 58 GeV/c data, then the "SciHi" rate would be more uniform. Figure 8 illustrates the case when -4cm< Z_{vtx} <2cm requirements made for the 58 GeV/c data. The remained run dependence can be explained by the beam width and the transverse position variations.

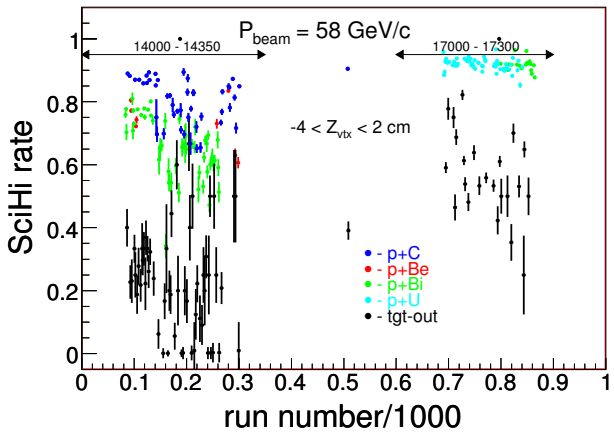

Figure 8: "SciHi" fires rate per proton interactions vs the run number, 58 GeV/c data

Figure 9 illustrates the scintillator trigger rate per single incident proton beam vs the run number.

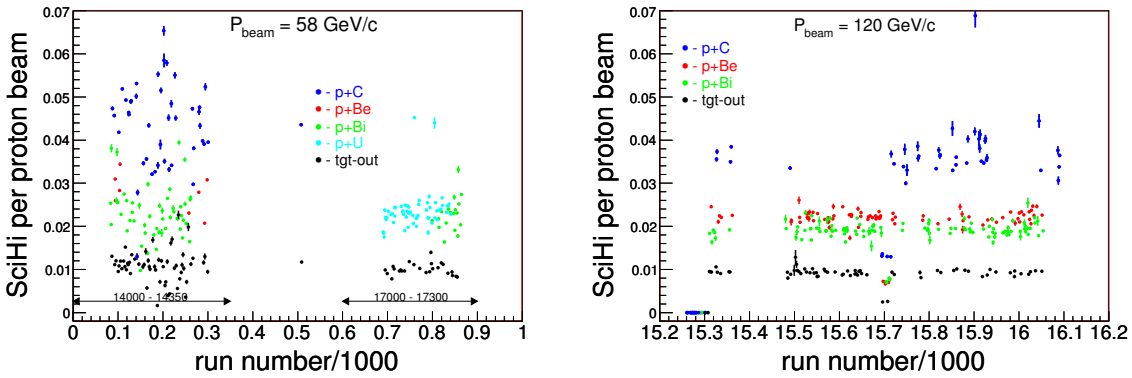

Figure 9: "SciHi" fires normalized per single incident proton beam vs the run number. Left plot - 58 GeV/c, right - 120 GeV/c data.

3.3 Selection of events with reliable tracking conditions

We found that in a relatively small fraction of events the sum of momenta of tracks is significantly higher than the beam momentum. Figure 10 illustrates the sum of momenta of the charged tracks in event using 120 GeV/c proton beam incident on carbon 2% target. The tracks from the primary vertex were used to make this plot.

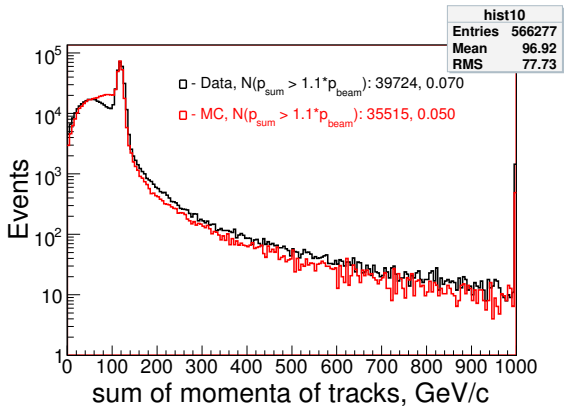

Figure 10: The sum of momenta of the charged tracks in event using the p+C interactions at 120 GeV/c for data (black) and Monte Carlo (red). Calculated sum based on the tracks which belong to the primary vertex.

The fraction of the events when the sum of momenta exceeds $1.1p_{beam}$ are 7.0% data and 5.0% for Monte Carlo. It is obvious that events, where the momentum conservation law is violated, might be useful for special studies, but not for cross section measurements. Thus, we identified a special category of events in which MIPP detector and software do not allow us to perform physics analysis. Speaking of the neutron analysis momentum conservation is one of the key requirements. Hence we drop those events before counting of the incident protons.

3.4 Beam track selection cut efficiencies

Beam track selection cut efficiencies are summarized in two Tables: Table 3 for the thin target data and Table 4 for the liquid hydrogen data.

3.5 Counting of incident protons

The counting of incident protons was done for events which passed all above discussed selection requirements. The incident proton counting was based on two methods: the proton beam prescalers (rs→trigps[6]+1) and direct scalers (spill→gatedTrigBit[6]), where "rs" represents the run summary pointer and "spill" - spill summary. First proton counter was incremented by each "good" event times the proton beam prescaler, second - direct accumulating of given scaler. If beam trigger event was failed by

cut name	N(58-thin)	EFF(58-thin)	N(120-thin)	EFF(120-thin)
Total events	1667211		2615429	
nTrks>30	1543447	0.926	2518598	0.963
Calo status	1543447	1.000	2518592	1.000
Is beam trk?	1477568	0.957	2470960	0.981
Single beam trk	869439	0.558	2011903	0.814
nCrossing < 5	685526	0.788	1674480	0.832
radius-1<2.0cm	670633	0.978	1618680	0.967
radius-2<2.0cm	653655	0.975	1618680	1.000
track time	646536	0.989	1610870	0.995
trk divergence	645172	0.998	1610784	1.000
P<1.1P$_{beam}$	602133	0.933	1509270	0.937
Total efficiency		0.361		0.577
Proton fraction	246413	0.409	1499105	0.993

Table 3: Beam track selection cut efficiencies and proton fractions for the thin target data.

cut name	N(58-LH2)	EFF(58-LH2)	N(84-LH2)	EFF(84-LH2)
Total events	802616		916581	
nTrks>30	772373	0.962	847790	0.925
Calo status	772373	1.000	847787	1.000
Is beam trk?	745447	0.965	826374	0.975
Single beam trk	480130	0.644	590770	0.715
nCrossing < 5	386237	0.804	492143	0.833
ellipse cut	300063	0.777	364479	0.741
track time	291234	0.971	363265	0.997
trk divergence	290707	0.998	362342	0.997
P<1.1P$_{beam}$	275275	0.947	328733	0.907
Total efficiency		0.343		0.359
Proton fraction	92414	0.336	202371	0.616

Table 4: Beam track selection cut efficiencies and proton fractions for the liquid hydrogen data.

some reasons: the track time is off or the calorimeter status is not readable, then the scaler subtraction was applied. For the test purpose we count the incident protons in two ways: in first - without subtraction applied (in Table 5) and second - with the correction for those protons which was rejected by some reason(s) - in Table 6.

target	$p_{beam}, GeV/c$	prescaler bit	direct scalers	ratio
H_2	20	6863900	6712290	1.023
Empty Cryo	20	1077263	1055900	1.020
H_2	58	55527097	55046896	1.009
Empty Cryo	58	12250227	11941328	1.026
Beryllium	58	4435167	4448628	0.997
Carbon	58	16159654	16011182	1.010
Bismuth	58	33625880	32735965	1.027
Uranium	58	71706424	69833283	1.027
Empty thin	58	26332939	25641913	1.027
H_2	84	71645485	69168883	1.036
Empty Cryo	84	24199480	22290732	1.086

Table 5: The number of incident protons calculated with two methods: accumulating the direct scaler and using the proton prescaler. Data selection: all data events without any rejections.

4 Vertex Method Selection

MIPP software has two options for fitting of the interaction point - a vertex. They are "dafit" and "confit". The first one has an advantage on the transverse and total momentum resolution. The second option, "confit", uses what was done by the first method and then refits incoming and outgoing track parameters simultaneously. We select this method because it has a better resolution in Z direction. Using the "confit" method we are better able to reduce (subtract) backgrounds due to interactions with the trigger scintillator. The neutron analysis is not sensitive to the track momentum resolution, which might be gained by using the "dafit" method, because the neutron momentum resolution is defined by the calorimeter.

For the neutron analysis we required that the incident protons should interact within the target region. This case was named as "primary vertex" selection. We applied both transverse and longitudinal vertex position cuts. For the transverse position cut we used the same cut as for the beam track with a slightly bigger radius to account the possible multiple scattering of the incident particle between DC3 and the target. But there are some vertices's with the transverse positions are way off (2-3 cm and more away from the edge of the beam spot). This effect is present for the multi track (n$\geq$5) vertices's too. At this moment we have only one explanation: misreconstracted vertex and or tracking.

target	p_{beam}, GeV/c	prescaler bit	direct scalers	ratio
H_2	20*	2215467	2063857	1.07
Empty Cryo	20*	397364	376001	1.06
H_2	58	17156645	16572320	1.03
Empty Cryo	58	2877699	2740163	1.05
Beryllium	58	2207422	2220883	0.99
Carbon	58	8751838	8603366	1.02
Bismuth	58	17164512	16274597	1.05
Uranium	58	32643688	30770547	1.06
Empty thin	58	12397130	11706104	1.06
H_2	84	31372847	28896245	1.09
Empty Cryo	84	10962656	9053908	1.21
Beryllium	120	19864149		0.08
Carbon	120	5542062		0.07
Bismuth	120	21559032		0.08
Empty thin	120	8004477		0.15

Table 6: The number of incident protons calculated with two methods: accumulating the direct scaler and using the proton prescaler. Results presented for different momenta and targets. Both results were corrected for protons which was rejected by some reason(s). Last column represents the ratio of two approaches. For 120 GeV/c it was estimated using runs, where the spill info was reliable. *Note: studies with RICH detector indicates that the pion contamination on 20 GeV/c proton beam is about 25%.

The fraction of the off-spot events for different beam momenta and targets are presented in Table 7. Using this data we might assign the systematic uncertainty or apply correction?

p_{beam} / target	H_2	Be	C	Bi	U
58 GeV/c	0.066	0.093	0.072	0.067	0.046
84 GeV/c	0.114				
120 GeV/c		0.019	0.015	0.021	

Table 7: The fraction of events when the transverse position of primary vertex was out of the beam spot.

The longitudinal (along Z direction) position cut depends on the length of the target. The vertex resolution in Z direction for the track multiplicity of 2 is about 3 cm (half width). Hence we are not capable of separating the interactions with the target from the interactions with the trigger scintillator, (about 2 cm from each other). Thus, we selected as the Z cut for the thin target -4 cm upstream of the target center and +4 cm downstream of the trigger scintillator. For the liquid hydrogen target data the Z cut was ±15 cm around the center of liquid hydrogen tube. The Z cut was applied for the primary vertices with any charged track multiplicity except single straight through track. In the primary vertex with the multiplicity of 1 the track is considered as a straight through if momentum was greater than 15 GeV/c. Figure 11 shows the longitudinal position distribution for the 120 GeV/c protons striking the carbon 2% target using both "dafit" and "confit" vertex methods. The trigger conditions: both proton beam and proton interaction triggers were used to make these plots.

The peak at about 0.4 cm represents the interactions with carbon 2% target, the peak at 2.5 cm indicates the interactions with trigger scintillator. The dashed plot illustrates the target-out only case. One can see from the plots that "confit" has sharper peaks. Due to of that we decided that it is better for the neutron analysis. The captions in plots allow to tell what is the fraction of interactions within the target region and downstream of the trigger scintillator. For example, using the "confit" plot we can read that the occupancy of both peaks (-2.5$< Z <$5.0 cm) is about 53%. The events with Z<-2 cm has occupancy of 36%. They represent the single beam track events where the Z value was assigned to be from -17 cm through -2 cm. The interactions downstream of the trigger scintillator are of 11%. They represent the interactions within the TPC volume. The surviving rate of events after both transverse and longitudinal vertex position cuts for this beam and target are 0.892 with "confit" and 0.887 with "dafit" vertex methods, respectively.

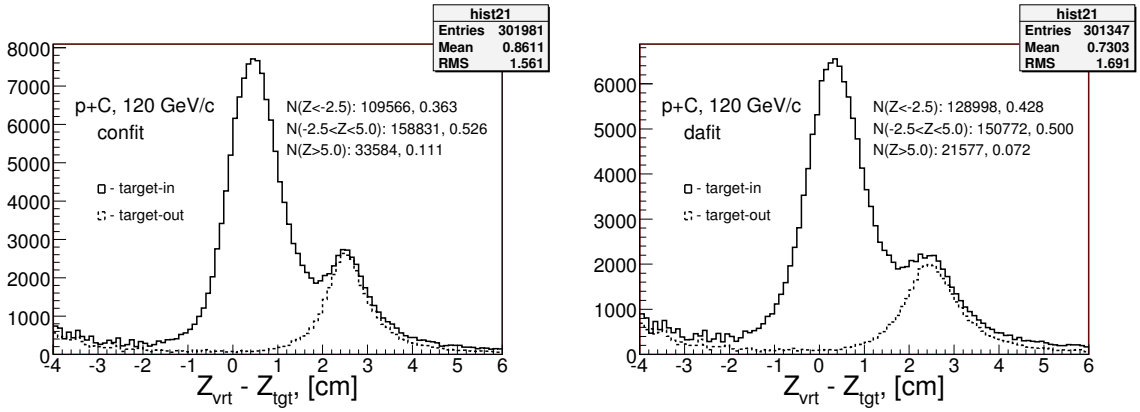

Figure 11: The longitudinal (along Z direction) position distribution for the 120 GeV/c protons striking the carbon 2% target with "confit" (on left) and "dafit" (on right) vertex fit methods. The solid line plot illustrates the target-in and dashed - target-out data. One can see from these plots that the "dafit" method has broader signal and background peaks.

5 Sum of Momenta: "confit" vs "dafit"

We knew that the "confit" vertex method drops an off-time track from the primary vertex list. It raised questions: how valid the time assignment for the track? What would be with the sum of momenta of tracks in case if this assignment is false? Remind that value of sum in use for the neutron selection. How to distinguish cases when drop was true and when it false? If it is the false then how recognize a right track in an unused list and bring it to the momentum balance?

Below we describe the study we performed in order to answer above questions. We select a control sample, run 15742 p+C interactions at 120 GeV/c. This control sample was processed with both "confit" and "dafit" vertex methods. We trying to see what are differences between these approaches. A comparison made on the event-by-event basis considering tracks from the primary vertex only. Figure 12 shows two plots: the sum of momenta of tracks (on left) and the differences for the sum between "confit" and "dafit".

The left plot on Figure 12 shows that the "confit" has a little higher occupancy at a peak and it below of "dafit" at low p_{sum} region. Plot indicates that the Δp_{sum} in 6% of cases might exceed 10 GeV/c. Due to of drop one might expect to see a tail on negative side. But the distribution tells that the tail on the positive side is not less, but a little higher. What is an explanation on that? An analysis shows that the major part of events are due to some issues with the "dafit" method. Remaining part caused by the reforming of the vertex. Figure 13 show the track multiplicity and the multiplicity differences for the same primary vertex between the both vertex methods.

Figure 13 right plots clearly shows the track drops by "confit". For drop the

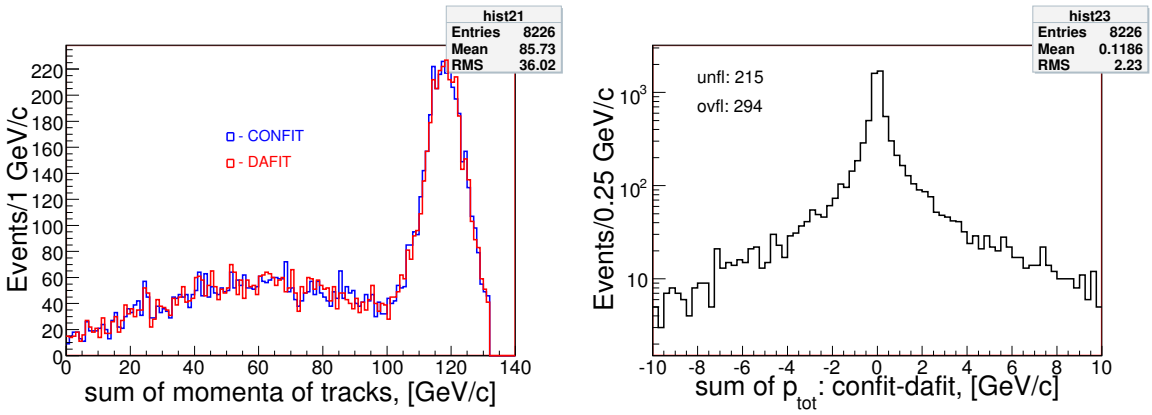

Figure 12: Left plot represents the sum of momenta of tracks. Right plot shows the differences for the sum of momenta of tracks between "confit" and "dafit"

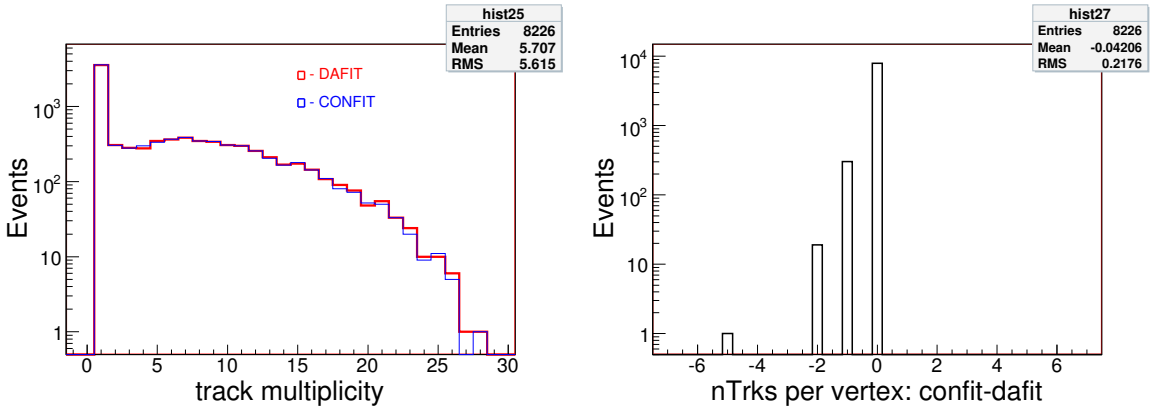

Figure 13: Left plot - the track multiplicity distributions for the primary vertex with "dafit" and "confit" methods. Right plot - multiplicity difference distribution.

difference became negative. We identified 323 multiplicity changes for 8226 considerations, about 4%. Drops occur in 303 events for 1, in 19 events for 2 and in 1 event for 5 tracks. Thus, the "confit" method slightly reduce the multiplicity of the charged tracks, but in another hand it keeps the momentum balance same as "dafit". However, our concerns are events on the negative tail, including underflows. By viewing the underflow events - 24 candidates, which associated with track drops, we found: 11 out of 24 - are looks a real off-time tracks, they have no match with RICH. We knew that RICH has a tight, ±50 ns, time gate. 22 events out of 24 are cases when dropped track(s) used to form another vertex with different the vertex position. One event out of 24 is case when one off-time track is present in the vertex, but another off-time was dropped. Finally, we bring the dropped track back to the primary vertex list, if it has match with RICH ring position within ±3 cm and has match with vertex within 0.8 cm in the transverse plane. For an example, in p+C interaction run 15359 event 2499 has a track with time 494 ns and momentum of 84 GeV/c which was dropped from the primary vertex. We found that for this track there is an unused RICH ring within 2.2 cm. Also, the track - vertex distance appear to be 0.3 cm. Figure 14 shows the track multiplicity per the primary vertex (blue plot). A red plot shows the multiplicity when "off-time" track was brought back to the vertex and it was in match with RICH ring. The distribution made using p+C interactions at 120 GeV/c. The fraction of events when the multiplicity was updated is 2.3%.

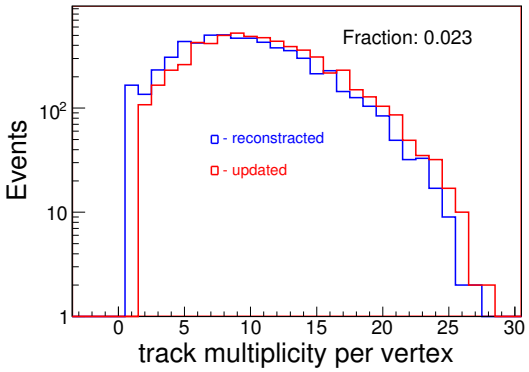

Figure 14: The track multiplicity per the primary vertex (blue plot). Red plot shows the multiplicity when the "off-time" track was brought back to the vertex and it was in match with RICH ring. The distribution was made using p+C interactions at 120 GeV/c.

6 Segment 456 Track Usage

What is a tracking efficiency? We have no information on this matter so far. But by viewing the neutron candidates on an "event display" tool we found a few missing

tracks. In one of such events we found that if we will use an unused track from the downstream segment track, then it would perfectly match with the EMCAL hits and unused RICH ring. Hence we decided to include to our track collection unused tracks from the downstream segment, which was named as a segment 456 track. There are some code modifications was needed to achieve this goal [4]. Since "pass4c" processed DST data has such option. Now we will discuss how to use it for the neutron analysis.

The problem with the segment 456 track is that the momentum information is not supported by the MIPP software. But RICH - track match procedure require the knowledge of the particle momentum vector, which used to pass the light through set of mirrors. We can assign a Pz momentum component for the track using the missing momentum in event. It can be done only if there is a single segment 456 track. Px and Py values can by calculated using the track slopes. Then the RICH ring and segment 456 track match procedure is following:

- Select single track events
- Assign Pz from the missing momentum in the primary vertex: p_{beam} - $\sum p_{trk}$
- Calculate Px and Py using Pz and track slopes
- Apply the RICH ring position prediction function - PredictRingCenter
- Use average mirror offsets in X and Y views
- Test for the segment 456 track - RICH ring match (within 2 cm)

Figure 15 shows two plots: the RICH ring (on left) and the segment 456 track (on right) multiplicities. Both plots illustrate what was reconstructed by these detectors but did not fall into the global track stream.

For the given p+C interaction data at 120 GeV/c on average the segment 456 track and the unused RICH ring availabilities are about 32% and 22%, respectively. The numbers from captions on Figure 15 allow to calculate the segment 456 track - RICH ring match efficiency: $\epsilon = 7944 / 28249 = 0.281$. The low efficiency indicates that the segment 456 track in most of the cases is a fake. For example, the fraction of events, when the number of hits on this track equal to 8, is about 45%. In this subsample the track can be made using 4 hits from DC4, nothing from PWC5 and 4 hits from PWC6. Another example, if we require 9 hits on the segment 456 track, then the match efficiency rises to 36%. But some of the fake tracks survive. The main reason for the fakes is that PWC6 is very noisy. Thus, we might accept only those segment 456 tracks, which match with the RICH ring position. Only those tracks were considered for the neutron analysis. For an example, in p+C interaction run 15327 event 2441 for the single segment 456 track particle momentum of 97 GeV/c was assigned. Then it was found to be in match with RICH ring within 0.8 cm and with the EMCAL shower too. Figure 16 shows the assigned momentum distribution for the segment 456 tracks when match with RICH ring is on. The distribution made using p+C interactions at 120 GeV/c. The fraction of such events is 2.3%.

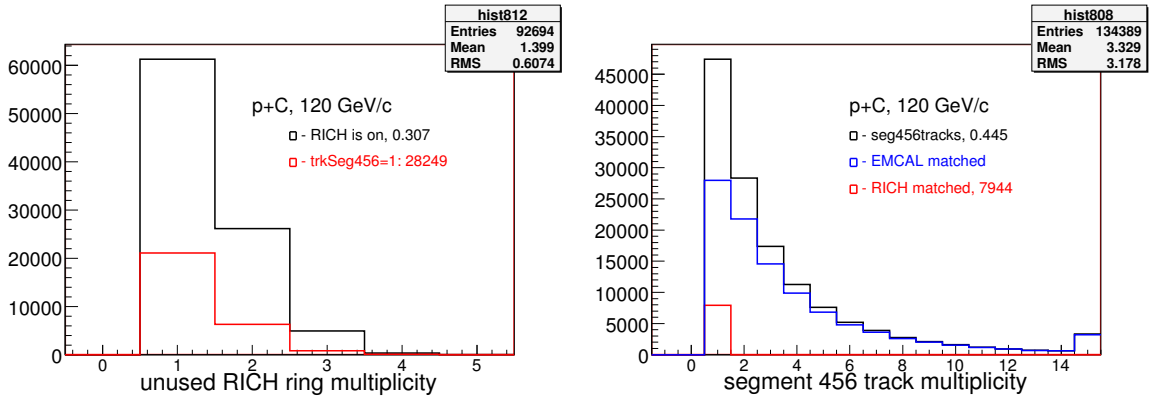

Figure 15: Left plot represents the RICH ring multiplicity: black plot indicates the multiplicity of unused rings (rate is about 0.22), the red plot shows cases when it associated with a single segment 456 track. The right plot shows the segment 456 track multiplicity: the black plot represents the total occupancy (rate is about 0.32). The blue and red plots show cases when it matches with EMCAL and RICH respectively.

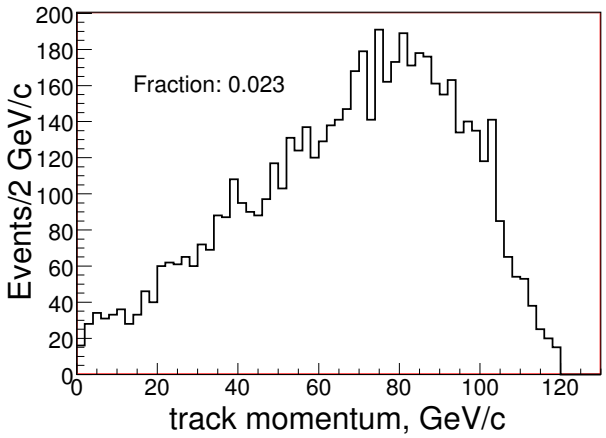

Figure 16: The assigned momentum distribution for segment 456 tracks when it matches with a RICH ring. The distribution was made using p+C interactions at 120 GeV/c..

7 Missing Total Momentum

Before discussing the neutron selection we might try to answer the question: is there any room for the neutrons in our data? We can answer this question by viewing the missing momentum distribution. Figure 17 represents the missing momentum for two proton beam momenta: 58 GeV/c (on left) and 120 GeV/c (on right). The missing momentum is $\Delta p = p_{beam} - \sum p_{trk}$ quantity, where $\sum p_{trk}$ is based on tracks from the primary vertex.

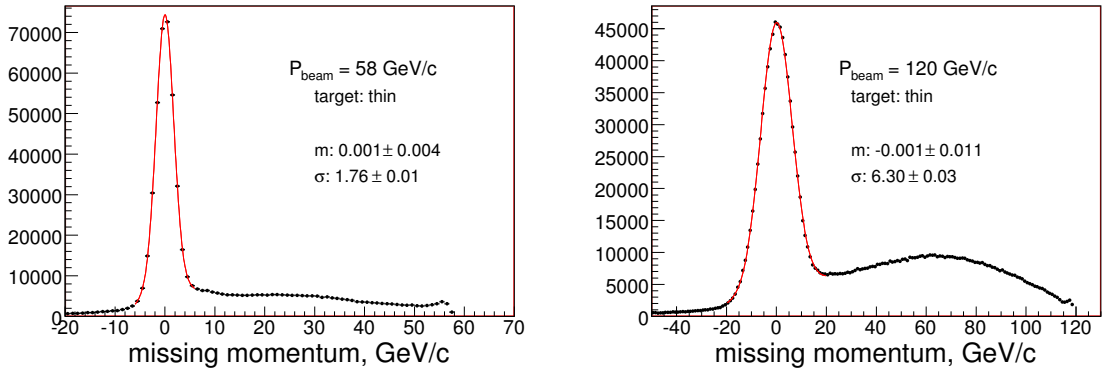

Figure 17: The missing total momentum distributions for two proton beam momenta: 58 GeV/c (on left) and 120 GeV/c (on right). The missing total momentum represents $\Delta p = p_{beam} - \sum p_{trk}$ quantity, where $\sum p_{trk}$ is based on tracks from the primary vertex.

The negative tail of the distribution in Figure 17 represents the cases when $\sum p_{trk}$ is significantly higher than the beam momentum. The peak represents cases when $p_{beam} \approx \sum p_{trk}$. The width of the peak reflects the momentum resolution integrated over all outgoing tracks. The cases with p_{missed} >7 GeV/c (on left) and p_{missed} >20 GeV/c (on right) represents the room for neutrals in the event. According to this data almost every third event for left plot and every second event for right plot are associated with neutrals production, where neutrons are a subsample of these neutrals.

8 Missing Transverse Momentum

Here we like to find out that is any an advantage on the neutron selection by using the missing transverse momentum value? Figure 18 represents the p_T differences between the combined transverse momentum of all outgoing tracks in the primary vertex and incoming beam track. Plots made using the p+C interactions at 120 GeV/c for the different bin size in Δp_T: 0.25 GeV/c (on left) and 0.01 GeV/c (on right).

The blue plot in Fig. 18 made for events after the vertex Z position cut applied, the red plot - events passed the neutron selection requirements (details are on next

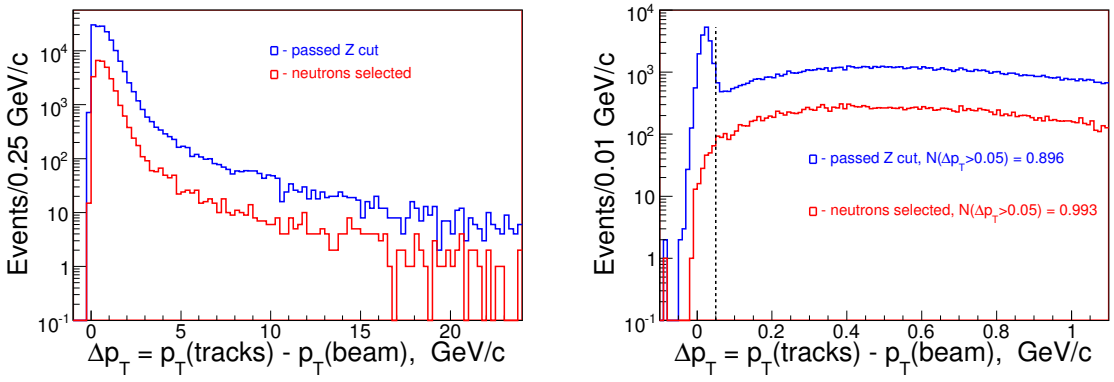

Figure 18: The missing transverse momentum distributions using the p+C interactions at 120 GeV/c. The missing transverse momentum represents $\Delta p_T = p_T^{trk}$ - p_T^{beam} quantity, where p_T^{trk} is based on tracks from the primary vertex. Left plot done with 0.25 GeV/c and right with 0.01 GeV/c bin sizes, respectively.

section). Plots illustrate that with and without the neutron selection requirements behavior of distributions are pretty much similar, except $0 < \Delta p_T < 0.05$ GeV/c region. The peak at low missed momentum region illustrate the presence of the beam straight through events. Plots made with interaction trigger and SciHi suggests that by applying the $\Delta p_T > 0.05$ GeV/c cut we might exclude the beam straight throughs. The caption in the right plot tells that 89.6% of events would survive this cut. While it cutting only 0.7% of neutron sample.

How this peak will looks like for the unbias data (beam triggers without SciHi requirement)? Figure 19 represents such cases for 58 GeV/c (on left) and for 120 GeV/c (on right) using all thin targets data.

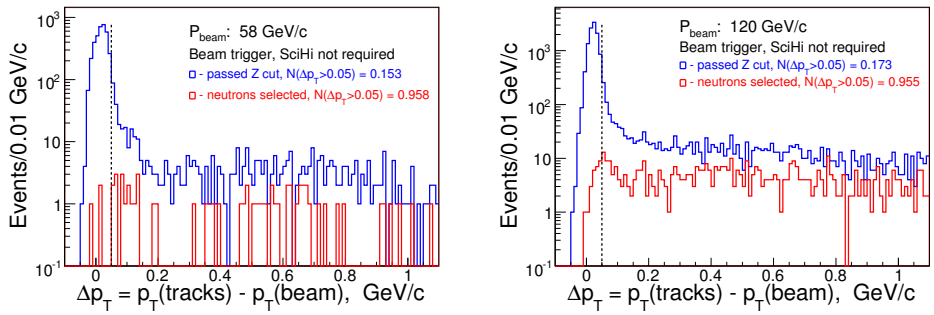

Figure 19: The missing transverse momentum distributions using the thin targets at 58 GeV/c (on left) and at 120 GeV/c (on right). Plots suggests that the straight through partially will remain there. Most effective cut might be 0.015 GeV/c.

We do not expect that the transverse momentum cut would be useful for Monte

Carlo samples. As indicated in Figure 20 by applying this cut we just slightly reducing the statistics.

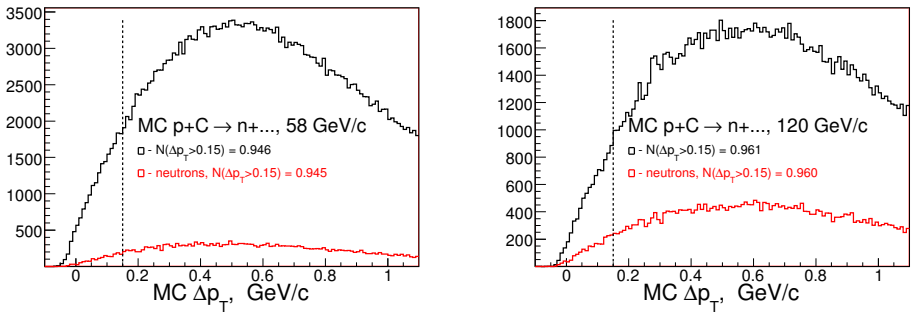

Figure 20: The missing transverse momentum distributions for Monte Carlo samples at 58 GeV/c (on left) and at 120 GeV/c (on right).

9 Neutron Selection Requirements

Below we summarize cuts applied after the event selection listed in Section 3.

- use the primary vertex only
- transverse position of vertex for thin targets is same as radius of the incoming beam: 0.8cm for 120 GeV/c and 2.0cm for 58 GeV/c
- longitudinal position is within -4cm $< Z_{vtx} <$ 6cm for thin targets and $\pm$15 cm for the liquid hydrogen target
- missing transverse momentum cut: Δp >0.15 GeV/c

Finally, neutron selection requirements are:

- Proton interaction bit in the prescaled trigger word is on
- "SciHi" trigger bit in the raw trigger word should be on
- Choose the lowest momentum value of neutron $P_n(min)$ for given beam settings using the missing momentum distribution.
- There is no charged track with P>0.7*P_{beam}
- Include the segment 456 track to the momentum balance if it points to HCAL and matches with a RICH ring

- Momentum balance requirement: $(\sum P_{tracks} + \mathrm{P}_n - \mathrm{P}_{trkHcal}) < 1.2 * \mathrm{P}_{beam}$, where $\sum P_{tracks}$ is the total momentum of all charged tracks in event, P_n is the neutron momentum and $\mathrm{P}_{trkHcal}$ is the combined momentum of charged tracks pointing to the HCAL. Term $\mathrm{P}_{trkHcal}$ is a subsample of $\sum P_{tracks}$ and it needs to be subtracted in order to avoid double counting.

- Candidate should have sufficient deposition to calorimeter compared with the sum of momenta of tracks pointing to calorimeter: $(P_n - P_{trkHcal}) > 3\sigma$, where σ represents the HCAL energy resolution

The neutron momentum is: $\mathrm{P}_n = \mathrm{E}_{hcal} + \mathrm{E}_{emcal} - (\mathrm{P}_{trkHcal} - \mathrm{E}_{trksEmcal})$, where E_{hcal} is an energy deposition into HCAL, E_{emcal} is projected energy losses of neutrons in EMCAL, $\mathrm{P}_{trkHcal}$ is tracks momentum pointing to HCAL and $\mathrm{E}_{trksEmcal}$ is track energy lost in EMCAL. The neutron energy scale normalization and the estimated E_{emcal} values based on protons are described in Appendix B.

Neutron counting: each candidate event accumulated with a weight, where weight is the proton interaction prescaler on run-by-run basis.

What is the minimum neutron momentum to choose? To answer for this question we will review more closely the missing total momentum distribution. Figure 21 represents the missing momentum for two proton beam momenta: 58 GeV/c (on left) and 120 GeV/c (on right) with different cuts.

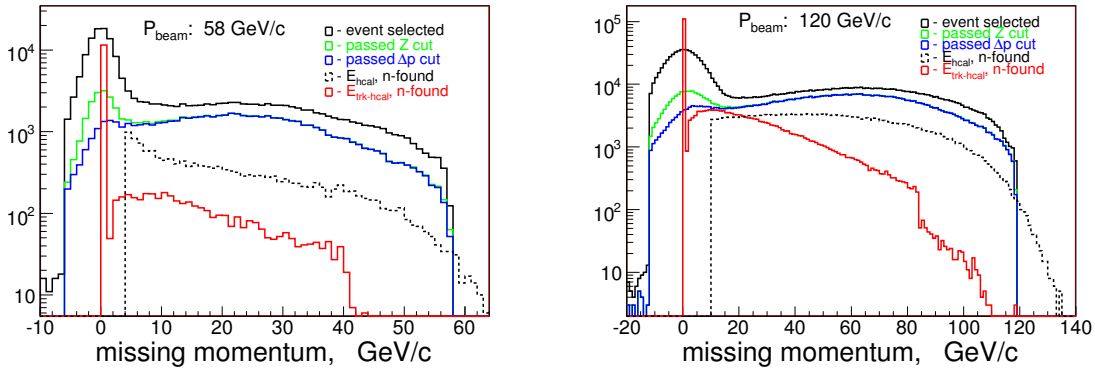

Figure 21: The missing total momentum distributions for two proton beam momenta: 58 GeV/c (on left) and 120 GeV/c (on right) with different cuts. Black plot - events passed the selection requirements discussed in section 3. Green plot - passed the vertex Z position cut, blue plot - passed the transverse momentum cut. Dashed black plot - energy deposited into HCAL for the neutron sample. Red plot - sum of tracks momenta pointing to HCAL fiducial.

Figure 22 shows the neutron spectrum with carbon target at 58 and 120 GeV/c, where the neutron minimum momentum selected as 4 GeV/c and 10 GeV/c, respectively.

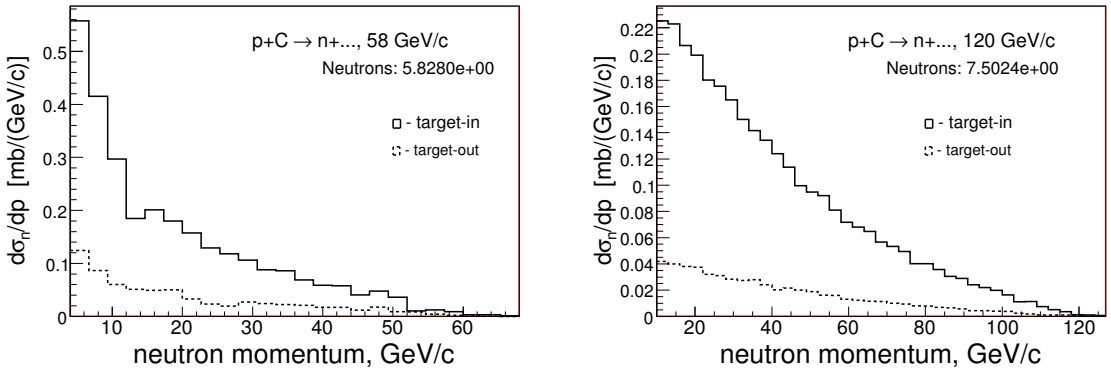

Figure 22: The neutron momentum distributions using p+C interactions at 58 GeV/c and 120 GeV/c, where the neutron minimum momentum selected as 4 GeV/c and 10 GeV/c, respectively.

10 Neutron Uncorrected Spectra

Below we present the uncorrected neutron spectra from various targets using 20 GeV/c, 58 GeV/c, 84 GeV/c and 120 GeV/c proton beams. The measurements were done using liquid hydrogen, Beryllium, Carbon, Bismuth and Uranium targets. Uncorrected means that we have not applied yet the trigger efficiency, calorimeter acceptance, and other corrections.

Our longitudinal vertex position resolution not allow to distinguish interactions at target versus interactions with the trigger scintillator. Due to of that we measured the neutron spectra also with the target-out case and then applied the subtraction procedure. For proper subtraction both target-in and target-out samples are normalized to same number of the incident proton beam particles.

10.1 Spectra at 20 GeV/c

Figure 23 shows the neutron spectrum with liquid hydrogen target at 20 GeV/c.

10.2 Spectra at 58 GeV/c

Figure 24 shows the neutron spectrum with liquid hydrogen target at 58 GeV/c.

Figure 25 shows the neutron spectrum with beryllium target at 58 GeV/c.

Figure 26 shows the neutron spectrum with carbon target at 58 GeV/c.

Figure 27 shows the neutron spectrum with bismuth target at 58 GeV/c.

Figure 28 shows the neutron spectrum with uranium target at 58 GeV/c.

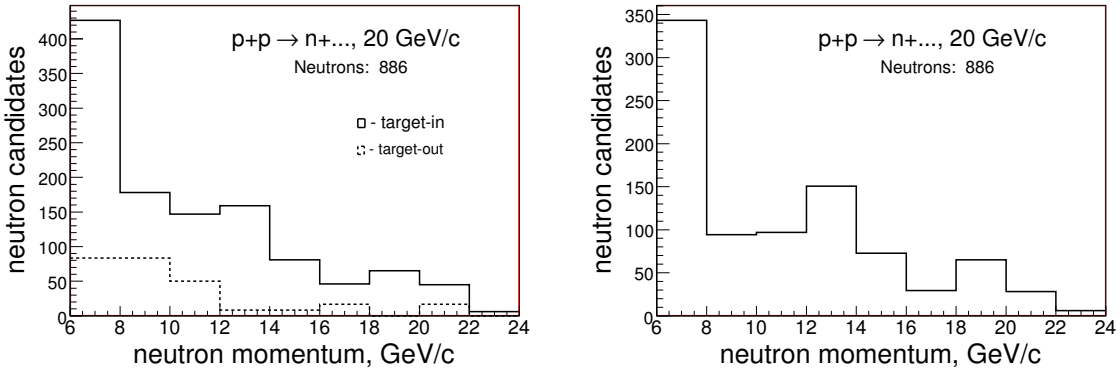

Figure 23: The neutron momentum distributions using p+p interactions at 20 GeV/c. Left plot represents both the target-in and target-out data. The right plot shows the neutron spectrum when the target-out subtraction was applied.

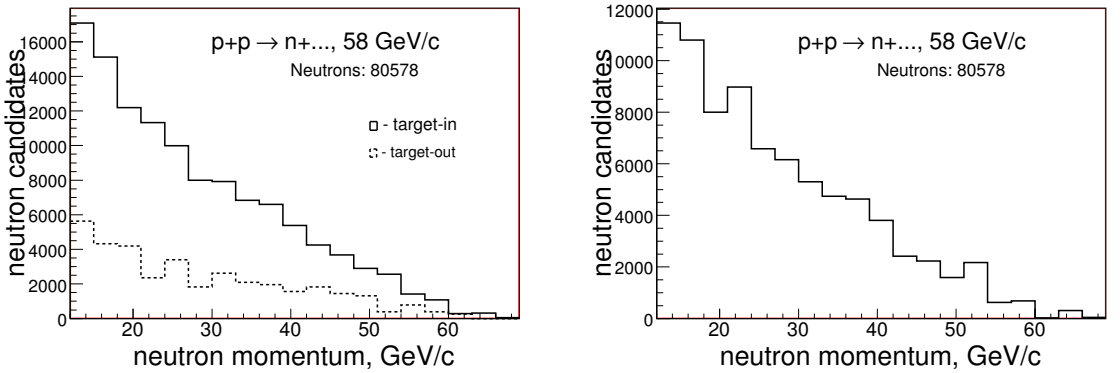

Figure 24: The neutron momentum distributions using p+p interactions at 58 GeV/c. Left plot represents both the target-in and target-out data. The right plot shows the neutron spectrum when the target-out subtraction was applied.

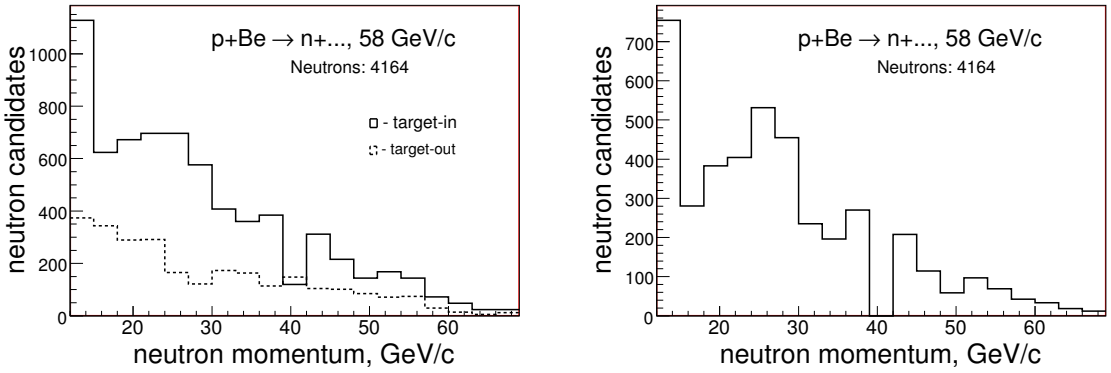

Figure 25: The neutron momentum distributions using p+Be interactions at 58 GeV/c. Left plot represents both the target-in and target-out data. The right plot shows the neutron spectrum when the target-out subtraction was applied.

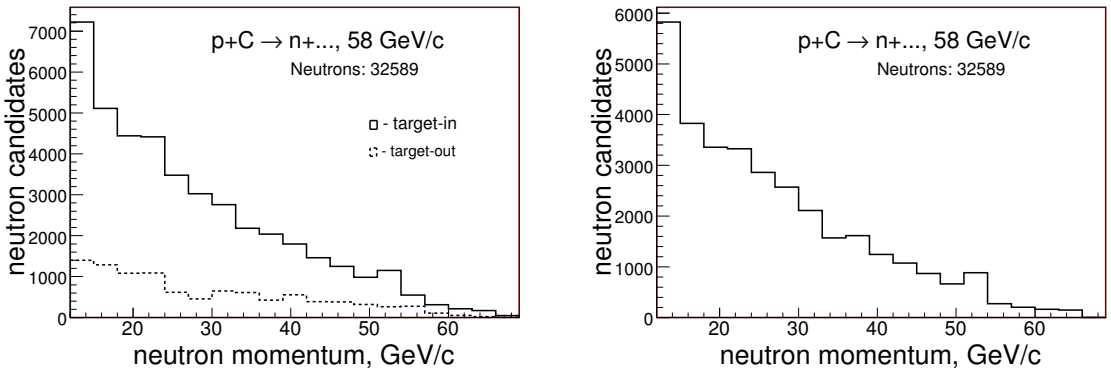

Figure 26: The neutron momentum distributions using p+C interactions at 58 GeV/c. Left plot represents both the target-in and target-out data. The right plot shows the neutron spectrum when the target-out subtraction was applied.

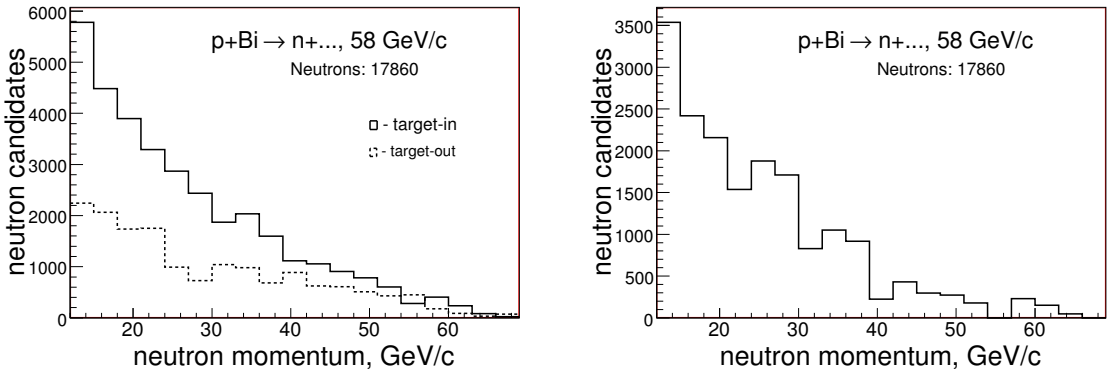

Figure 27: The neutron momentum distributions using the p+Bi interactions at 58 GeV/c. Left plot represents both the target-in and target-out data. The right plot shows the neutron spectrum when the target-out subtraction was applied.

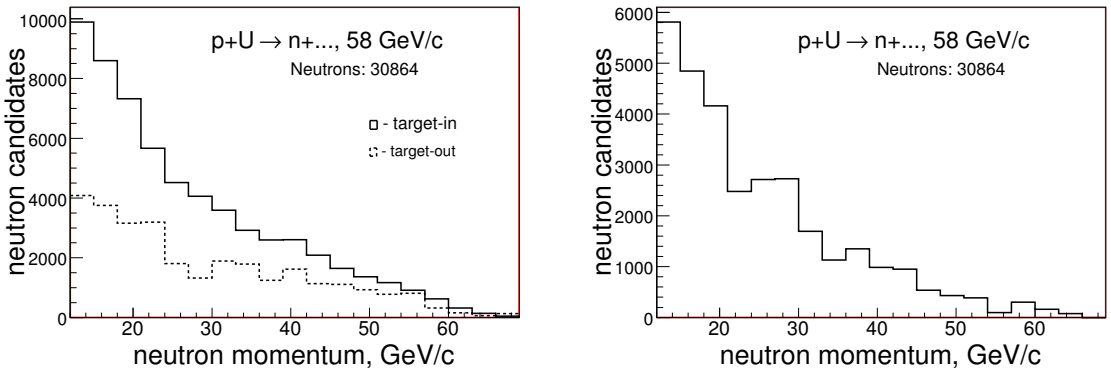

Figure 28: The neutron momentum distributions using the p+U interactions at 58 GeV/c. Left plot represents both the target-in and target-out data. The right plot shows the neutron spectrum when the target-out subtraction was applied.

10.3 Spectra at 84 GeV/c

Figure 29 shows the neutron spectrum with liquid hydrogen target at 84 GeV/c.

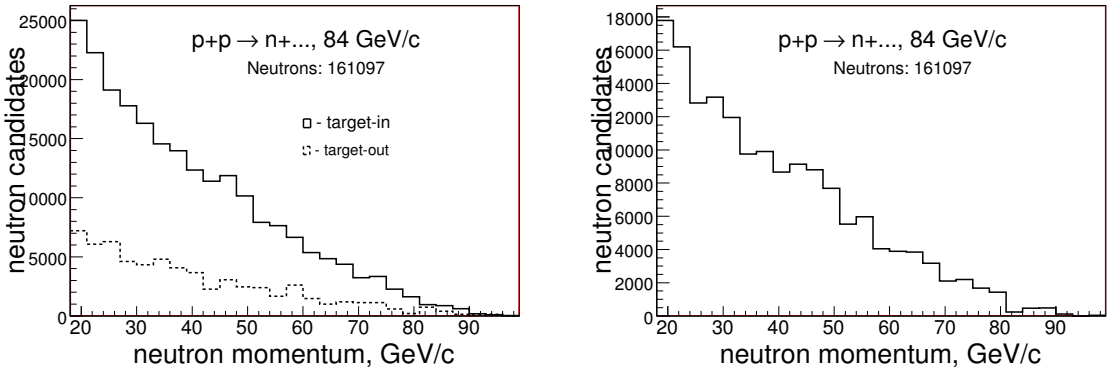

Figure 29: The neutron momentum distributions using p+p interactions at 84 GeV/c. Left plot represents both the target-in and target-out data. The right plot shows the neutron spectrum when the target-out subtraction was applied.

10.4 Spectra at 120 GeV/c

Using 120 GeV/c protons we measured the neutron production from interactions with beryllium, carbon and bismuth targets. Figure 30 shows the neutron spectrum with beryllium target. Figure 31 shows the neutron spectrum with carbon target. Figure 32 shows the neutron spectrum with bismuth target.

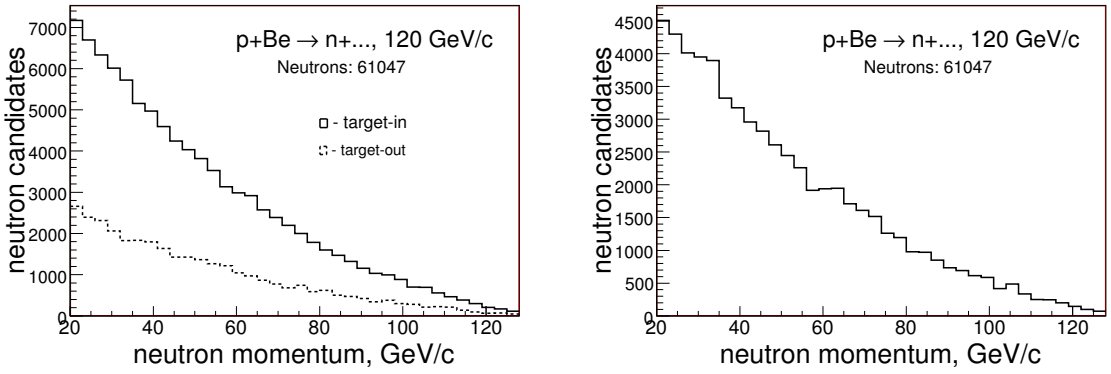

Figure 30: The neutron momentum distributions using the p+Be interactions at 120 GeV/c. Left plot represents both the target-in and target-out data. The right plot shows the neutron spectrum when the target-out subtraction was applied.

Table 8 represents the summary of the neutron sample size.

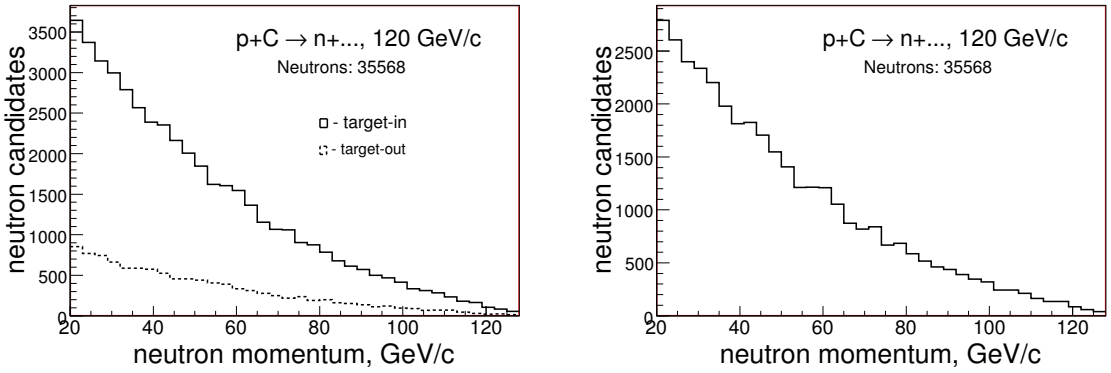

Figure 31: The neutron momentum distributions using the p+C interactions at 120 GeV/c. Left plot represents both the target-in and target-out data. The right plot shows the neutron spectrum when the target-out subtraction was applied.

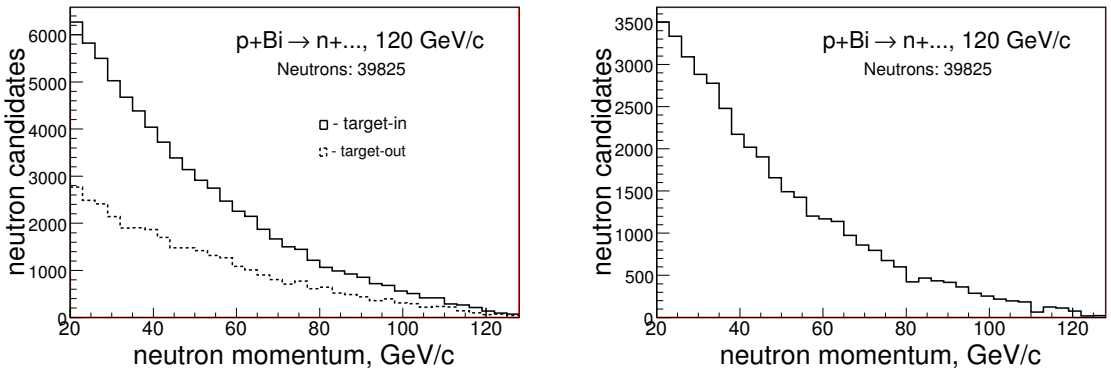

Figure 32: The neutron momentum distributions using the p+Bi interactions at 120 GeV/c. Left plot represents both the target-in and target-out data. The right plot shows the neutron spectrum when the target-out subtraction was applied.

	N_n	growth
H_2-20 GeV/c	886±48	
H_2-58 GeV/c	80578±1154	1.16
Be-58 GeV/c	4164±247	1.16
C-58 GeV/c	32589±773	1.19
Bi-58 GeV/c	17860±405	1.21
U-58 GeV/c	30864±421	1.20
H_2−84 GeV/c	161097±1517	-
Be-120 GeV/c	61047±199	1.15
C-120 GeV/c	35568±165	1.15
Bi-120 GeV/c	39825±146	1.17

Table 8: The summary of the neutron sample size. Growth column represents the increase factor relative to the previous neutron energy scale.

10.5 Vertex Z distributions for neutron samples

10.5.1 Z positions for data without scintillator

Before to look on the Z vertex distribution for the neutron samples we might want to see once how the Z positions looks like for data prior of the trigger scintillator was installed. Figure 33 shows Z position distributions for $\pi/K/p$ incident beams interacting with Be (on left), Bi (on middle) and target-out (on right) at 58 GeV/c.

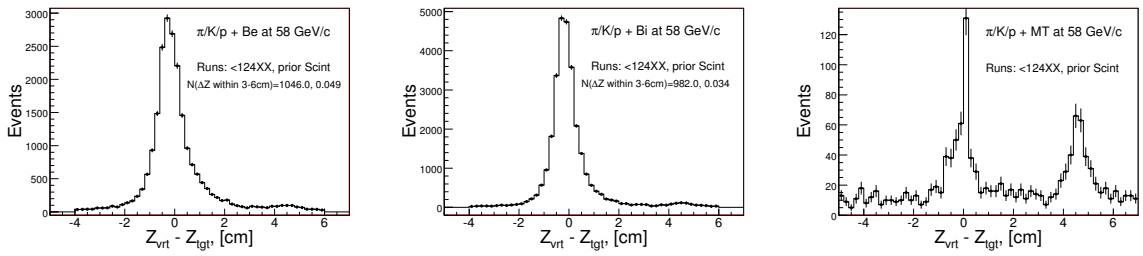

Figure 33: Z position distributions for $\pi/K/p$ incident beams interacting with Be (on left), Bi (on middle) and target-out (on right) at 58 GeV/c. The distributions with Be and Bi targets indicates the interactions around Z=4.5 cm. Target-out distribution shows same bump, but more pronounce. This peak represents interactions with TPC wall. For data with the scintillator installed the distance between the target center and TPC wall is about 7.5 cm

10.5.2 Z positions for data with the trigger scintillator

Below we will discuss the results of the target-out subtraction. Prior subtraction the target-out samples were normalized to same number of incident proton beam particles as in the target-in samples. Even so, the peak on the scintillator with target-out data appear to be slightly below than for the same peak on the target-in data.

Figure 34 shows the longitudinal vertex position distributions for the neutron candidates based on the interactions with the liquid hydrogen at 20 GeV/c beam momentum using the proton interaction triggers.

Figure 35 shows the longitudinal vertex position distributions for the neutron candidates based on the interactions with the liquid hydrogen at 58 GeV/c beam momentum using the proton interaction triggers.

Figure 36 shows the longitudinal vertex position distributions for the neutron candidates based on the interactions with the liquid hydrogen at 84 GeV/c beam momentum using the proton interaction triggers.

Figure 37 shows the longitudinal vertex position distributions for the neutron candidates based on the interactions with the Be target at 58 GeV/c beam momentum using the proton interaction triggers.

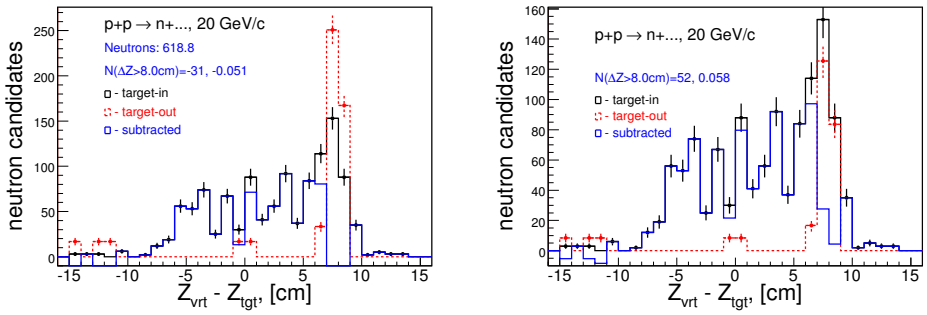

Figure 34: The longitudinal vertex position distributions for the neutron candidates based on the interactions with the liquid hydrogen at 20 GeV/c: without (on left) and with (on right) correction to the target-out size normalization. The correction factor is 1.7

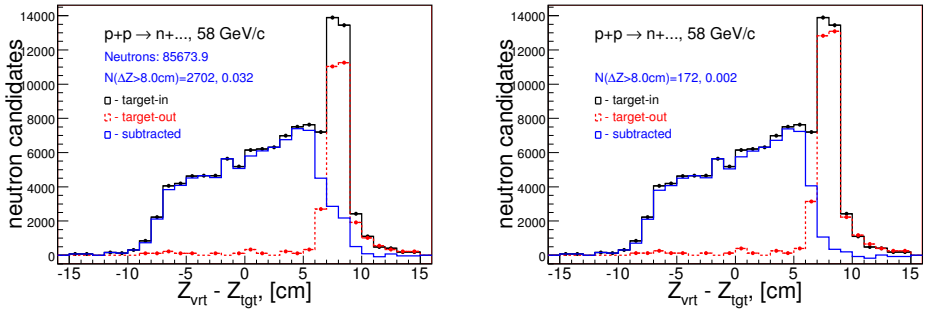

Figure 35: The longitudinal vertex position distributions for the neutron candidates based on the interactions with the liquid hydrogen at 58 GeV/c: without (on left) and with (on right) correction to the target-out size normalization. The correction factor is 1.11

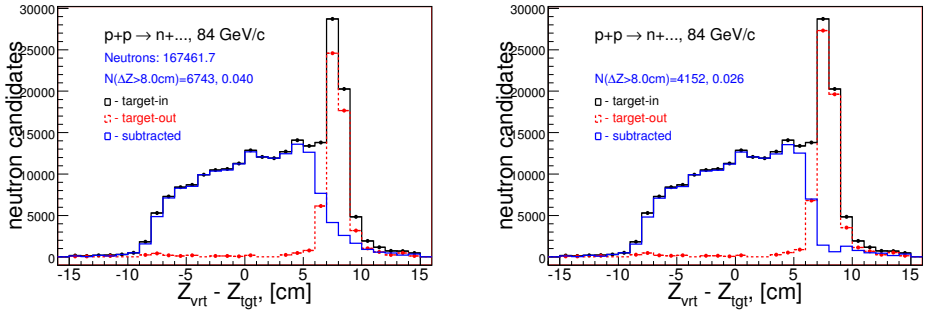

Figure 36: The longitudinal vertex position distributions for the neutron candidates based on the interactions with the liquid hydrogen at 84 GeV/c: without (on left) and with (on right) correction to the target-out size normalization. The correction factor is 1.18

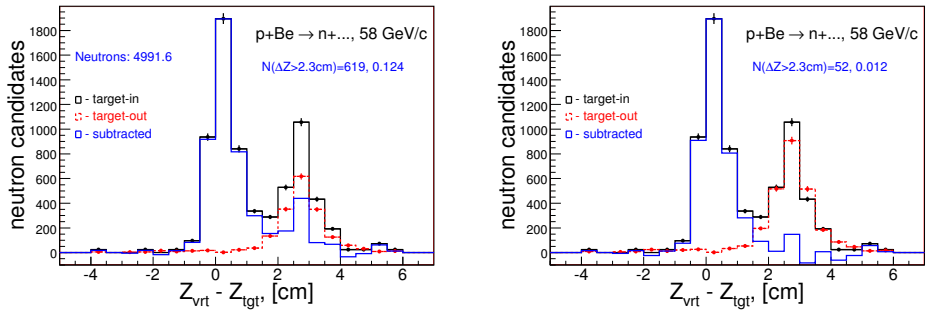

Figure 37: The longitudinal vertex position distributions for the neutron candidates based on the interactions with the Be target at 58 GeV/c: without (on left) and with (on right) correction to the target-out size normalization. The correction factor is 1.33

Figure 38 shows the longitudinal vertex position distributions for the neutron candidates based on the interactions with the C target at 58 GeV/c beam momentum using the proton interaction triggers.

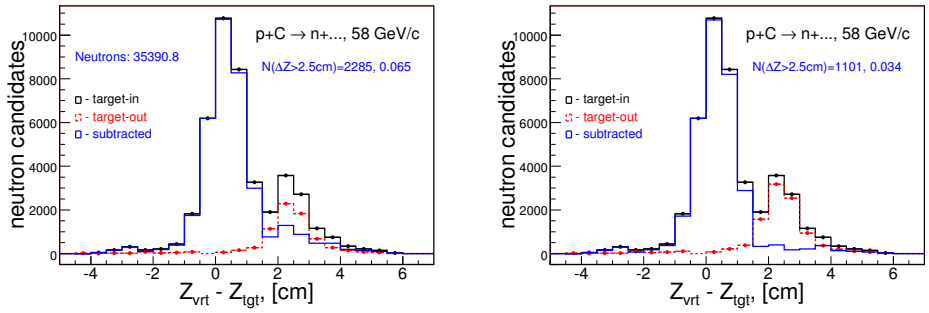

Figure 38: The longitudinal vertex position distributions for the neutron candidates based on the interactions with the C target at 58 GeV/c: without (on left) and with (on right) correction to the target-out size normalization. The correction factor is 1.33

Figure 39 shows the longitudinal vertex position distributions for the neutron candidates based on the interactions with the Bi target at 58 GeV/c beam momentum using the proton interaction triggers.

Figure 40 shows the longitudinal vertex position distributions for the neutron candidates based on the interactions with the U target at 58 GeV/c beam momentum using the proton interaction triggers.

Figure 41 shows the longitudinal vertex position distributions for the neutron candidates based on the interactions with the Be target at 120 GeV/c beam momentum using the proton interaction triggers.

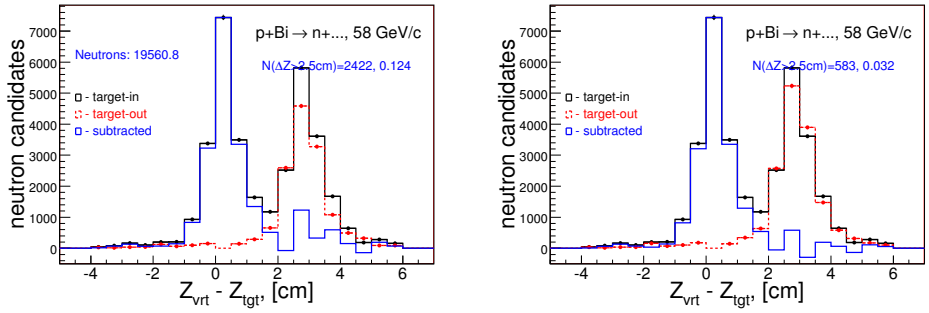

Figure 39: The longitudinal vertex position distributions for the neutron candidates based on the interactions with the Bi target at 58 GeV/c: without (on left) and with (on right) correction to the target-out size normalization. The correction factor is 1.14

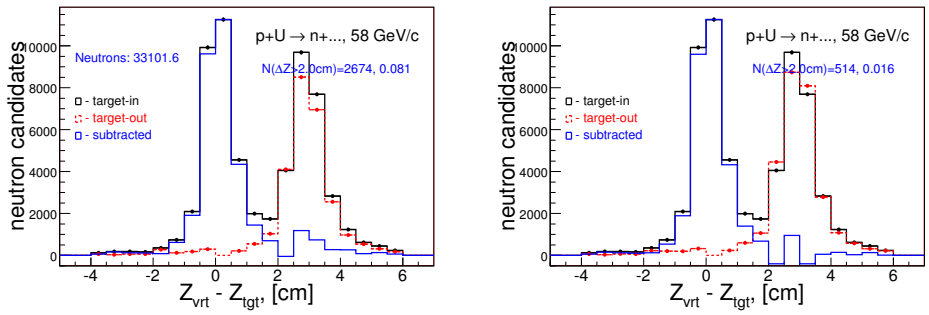

Figure 40: The longitudinal vertex position distributions for the neutron candidates based on the interactions with the U target at 58 GeV/c: without (on left) and with (on right) correction to the target-out size normalization. The correction factor is 1.09

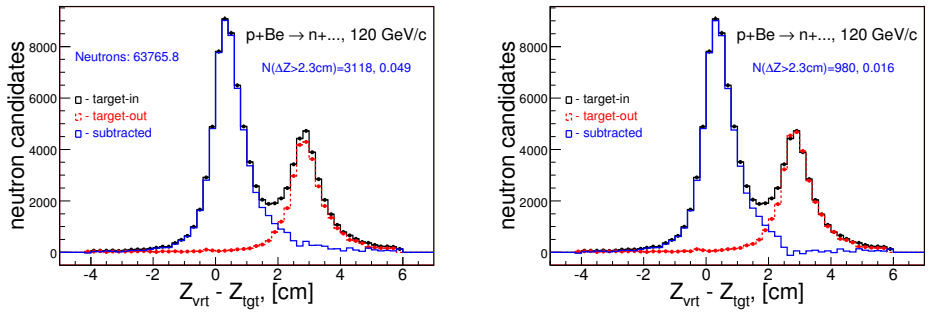

Figure 41: The longitudinal vertex position distributions for the neutron candidates based on the interactions with the Be target at 120 GeV/c: without (on left) and with (on right) correction to the target-out size normalization. The correction factor is 1.087

Figure 42 shows the longitudinal vertex position distributions for the neutron candidates based on the interactions with the C target at 120 GeV/c beam momentum using the proton interaction triggers.

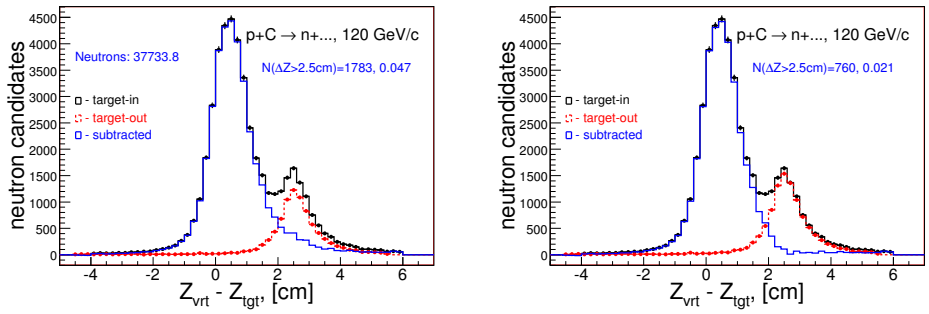

Figure 42: The longitudinal vertex position distributions for the neutron candidates based on the interactions with the C target at 120 GeV/c: without (on left) and with (on right) correction to the target-out size normalization. The correction factor is 1.25

Figure 43 shows the longitudinal vertex position distributions for the neutron candidates based on the interactions with the Bi target at 120 GeV/c beam momentum using the proton interaction triggers.

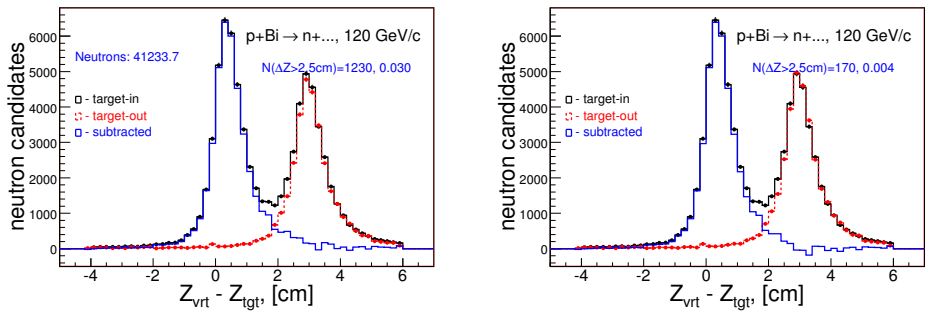

Figure 43: The longitudinal vertex position distributions for the neutron candidates based on the interactions with the Bi target at 120 GeV/c: without (on left) and with (on right) correction to the target-out size normalization. The correction factor is 1.042

Table 9 represents the number of neutrons calculated with and without corrections applied to the target-out size.

Figure 44 shows the neutron yields vs the run number.

The neutron yield calculated as:

$$\mathrm{Y}_n = \mathrm{nc}_{run} \times \frac{1}{N_{beam-run}} \times \frac{1}{A} \times \frac{1}{n_t} \times \mathrm{ipr} \times 10^4$$

p_{beam}	MT-CF	N_n(MT-uncorr)	N_n(MT-corr)	$\Delta N_n/N_n$
H_2-20 GeV/c	-	-	886	
H_2-58 GeV/c	1.16	85674	80578	0.06
Be-58 GeV/c	1.47	4992	4164	0.20
C-58 GeV/c	1.38	35391	32589	0.09
Bi-58 GeV/c	1.14	19561	17860	0.09
U-58 GeV/c	1.09	33102	30864	0.07
H_2−84 GeV/c	1.11	167462	161097	0.04
Be-120 GeV/c	1.09	63766	61047	0.04
C-120 GeV/c	1.25	37734	35568	0.06
Bi-120 GeV/c	1.04	41234	39825	0.04

Table 9: The number of neutrons with and without corrections applied to the target-out size.

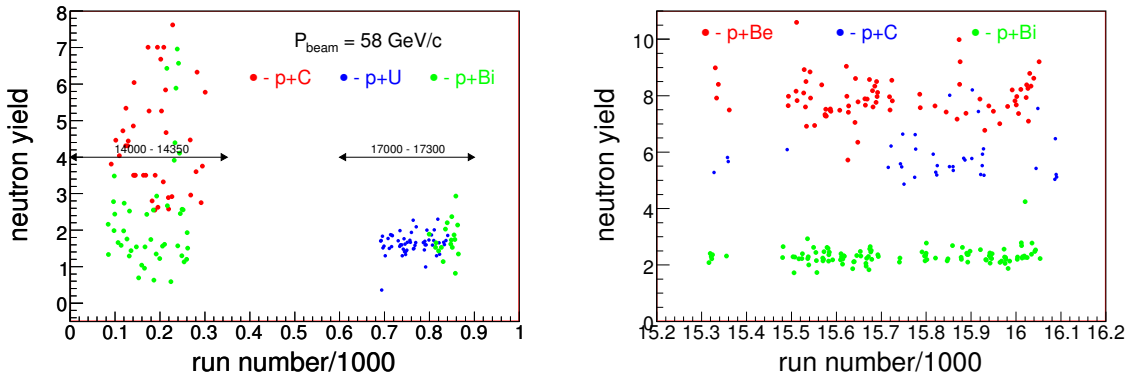

Figure 44: The neutron yield vs run number: 58 GeV/c data (on left) and 120 GeV/c data (on right). The target-out subtraction procedure is not applicable for this study.

where, nc_{run} and $N_{beam-run}$ are both represents what was accumulated for given run. The target-out subtraction procedure is not applicable for this study. 58 GeV/c data shows a great spread for the early runs. What is a reason for that? Possible an explanation is due to a big discrete beam and interaction prescalers for those runs. Figure 45 shows the beam and the interactions prescalers vs run number.

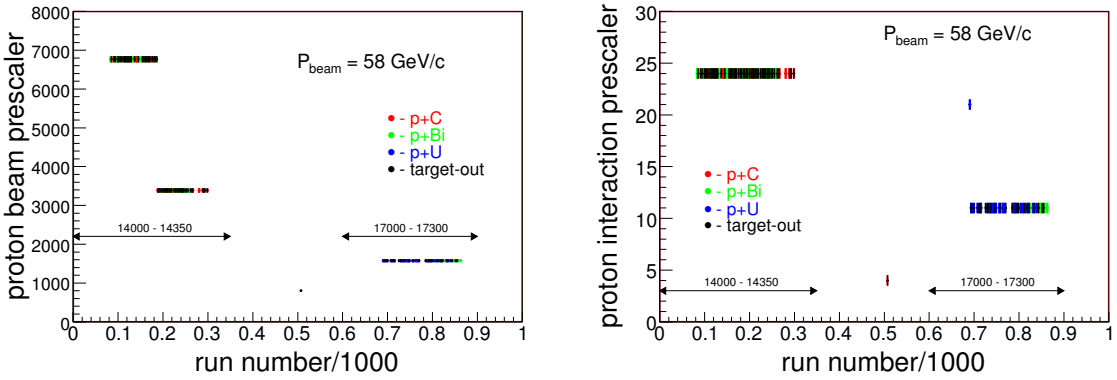

Figure 45: The proton beam and interaction prescalers values vs run number for the 58 GeV/c data

11 Trigger Efficiency

We study the trigger efficiency on both ways: using the unbias beam triggers in data and using Monte Carlo. We use the data sample consisting of the proton beam triggers and all requirements for the neutron selection applied, except "SciHi" (trigger) fires. As a supporting information, the track multiplicities for the proton interaction triggers are given in Appendix D.

11.1 Trigger efficiency for p+p at 20 GeV/c

Figure 46 shows the trigger scintillator pulse height distributions for the p+p interactions at 20 GeV/c using the liquid hydrogen target data for target-in (on left) and target-out subtraction applied (on right), respectively.

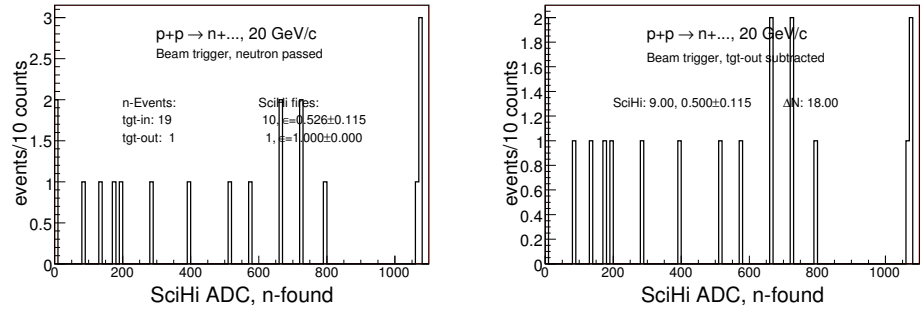

Figure 46: The "SciHi" pulse height distributions for the liquid hydrogen target data using 20 GeV/c proton beam triggers for target-in (on left) and target-out subtraction applied (on right), respectively.

Figure 47 shows the charged track multiplicities for the p+p interactions at 20 GeV/c.

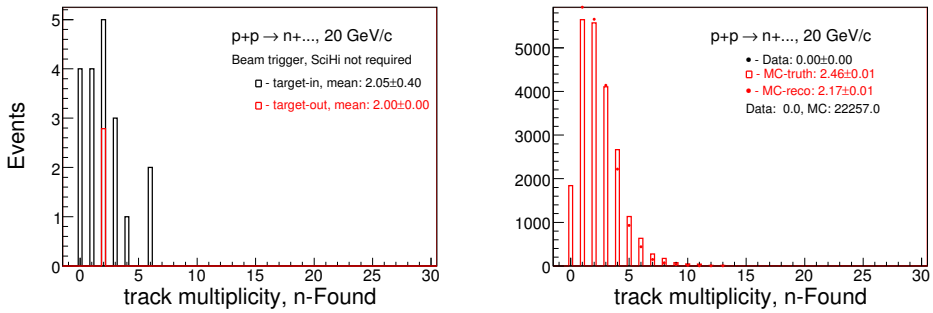

Figure 47: The charged track multiplicities for the liquid hydrogen target using 20 GeV/c proton beam triggers for data (left) and Monte Carlo (right), respectively.

Figure 48 shows the trigger efficiency as a function of the neutron momentum for p+p interactions at 20 GeV/c.

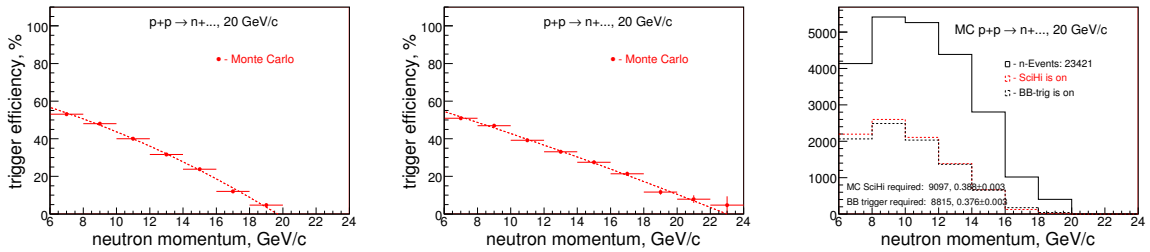

Figure 48: The trigger efficiency as a function of the neutron momentum for p+p interactions at 20 GeV/c: Monte Carlo efficiency dependence without (left) and with (middle) the neutron momentum smearing applied and MC average trigger efficiency (right).

The trigger efficiency study for p+p interactions at 20 GeV/c are summarized in Table 10.

N_{evt}	ϵ_{trig}(data)	ϵ_{trig}(MC-BB)	ϵ_{trig}(MC-SciHi)	ϵ_{trig}(final)	$\Delta\epsilon_{trig}$
19(1)	0.53(0.50)±0.12	0.38±0.003	0.39±0.003	0.46	±0.10

Table 10: Summary of the trigger efficiency studies for p+p interactions at 20 GeV/c. Last two columns represent assigned the final trigger efficiency and the systematic uncertainty.

11.2 Trigger efficiency for p+p at 58 GeV/c

Figure 49 shows the trigger scintillator pulse height distributions for the p+p interactions at 58 GeV/c using the liquid hydrogen target data for target-in (on left) and target-out subtraction applied (on right), respectively.

Figure 50 shows the charged track multiplicities for the p+p interactions at 58 GeV/c.

Figure 51 shows the trigger efficiency as a function of the neutron momentum for p+p interactions at 58 GeV/c.

The charged track multiplicities passing through the trigger scintillator for p+p interactions at 58 GeV/c are summarized in Table 11.

The trigger efficiency study for p+p interactions at 58 GeV/c are summarized in Table 12.

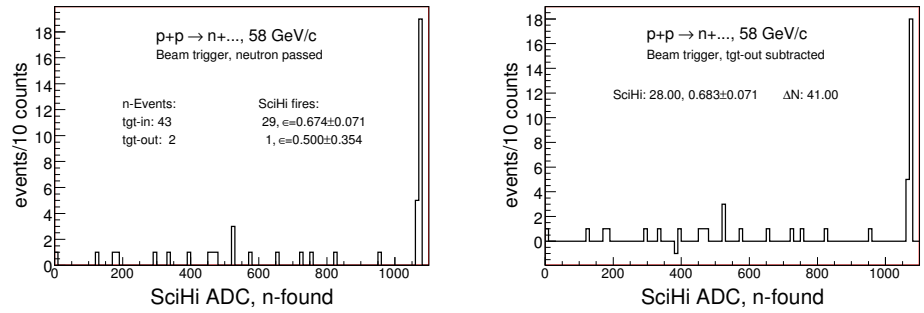

Figure 49: The "SciHi" pulse height distributions for the liquid hydrogen target data using 58 GeV/c proton beam triggers for target-in (on left) and target-out subtraction applied (on right), respectively.

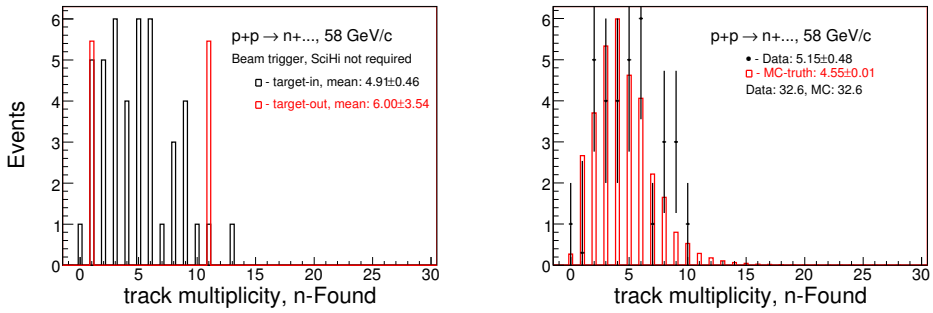

Figure 50: The charged track multiplicities for the liquid hydrogen target using 58 GeV/c proton beam triggers for data (left) and Monte Carlo superimposed (right), respectively.

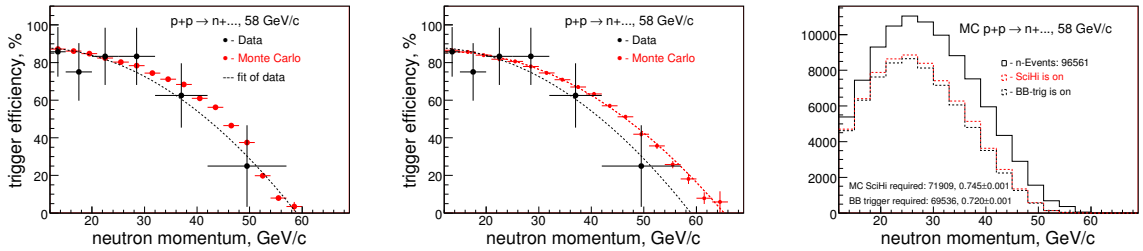

Figure 51: The trigger efficiency as a function of the neutron momentum for p+p interactions at 58 GeV/c: Monte Carlo efficiency dependence without (left) and with (middle) the neutron momentum smearing applied and MC average trigger efficiency (right).

N_{trk}(beam-tr)	N_{trk}(intr-tr)	N_{trk}(MC-true)	N_{trk}(MC-reco)
4.9(5.1)±0.47	4.81(4.62)±0.05	4.55±0.01	4.26±0.01

Table 11: Summary of the charged track multiplicities for p+p interactions at 58 GeV/c. The difference between N_{trk}(MC-true) and N_{trk}(MC-reco) are mainly due to of TPC acceptance.

N_{evt}	ϵ_{trig}(data)	ϵ_{trig}(MC-BB)	ϵ_{trig}(MC-SciHi)	ϵ_{trig}(final)	$\Delta\epsilon_{trig}$
43(2)	0.67(0.68)±0.07	0.72±0.001	0.74±0.001	0.71	±0.10

Table 12: Summary of the trigger efficiency studies for p+p interactions at 58 GeV/c. Last two columns represent assigned the final trigger efficiency and the systematic uncertainty.

11.3 Trigger efficiency for p+Be and p+C at 58 GeV/c

Figure 52 shows the trigger scintillator pulse height distributions for the p+Be and p+C interactions at 58 GeV/c.

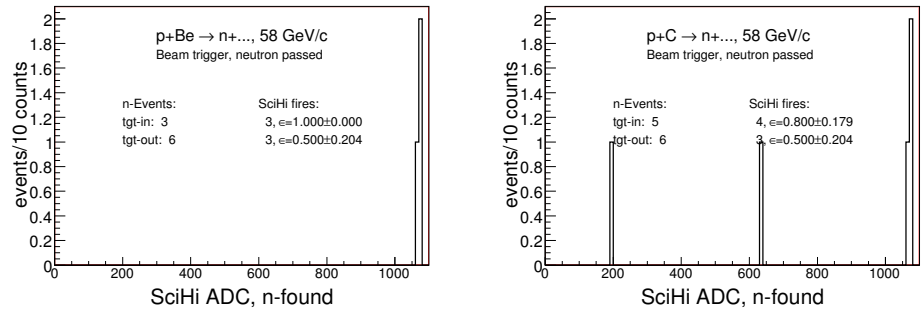

Figure 52: The "SciHi" pulse height distributions for p+Be (left) and p+C (right) interactions with 58 GeV/c proton beam triggers, respectively.

Figure 53 shows MC charged track multiplicities for the p+Be and p+C interactions at 58 GeV/c using interaction triggers.

Figure 54 shows Monte Carlo the average trigger efficiencies for p+Be and p+C interactions at 58 GeV/c.

Figure 55 shows Monte Carlo the trigger efficiency as a function of the neutron momentum for p+Be and p+C interactions at 58 GeV/c.

The charged track multiplicities passing through the trigger scintillator for p+Be and p+C interactions at 58 GeV/c are summarized in Table 13.

The trigger efficiency study for p+Be and p+C interactions at 58 GeV/c are summarized in Table 14.

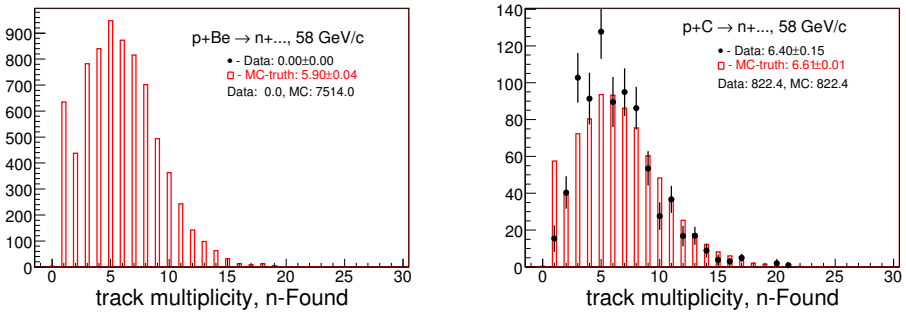

Figure 53: Monte Carlo charged track multiplicities for p+Be (left) and p+C interactions at 58 GeV/c. Since the multiplicities for the beam trigger requirements are not available, then compasion made for the interaction trigger cases.

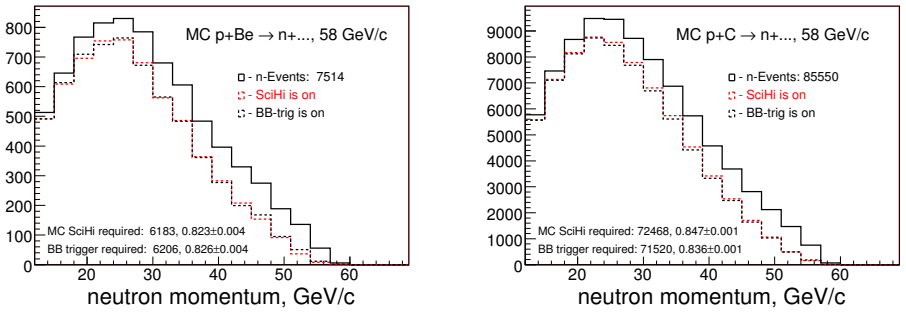

Figure 54: Monte Carlo the average trigger efficiencies for p+Be (left) and p+C (right) interactions at 58 GeV/c.

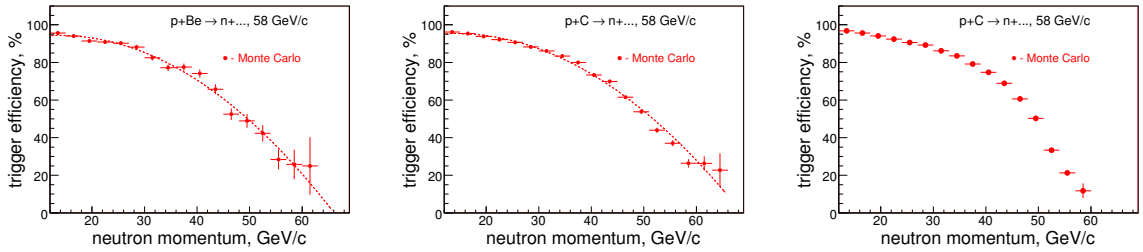

Figure 55: Monte Carlo the trigger efficiency as a function of the neutron momentum for p+Be (left) and p+C (middle and right) interactions at 58 GeV/c. Monte Carlo efficiency dependence with (middle) and without (right) the neutron momentum smearing applied.

	N_{trk}(beam-tr)	N_{trk}(intr-tr)	N_{trk}(MC-true)	N_{trk}(MC-reco)
Be, 58 GeV/c	n/a	6.03(6.23)±0.21	5.90±0.04	5.71±0.04
C, 58 GeV/c	n/a	6.10(6.40)±0.11	6.61±0.01	5.96±0.01

Table 13: Summary of the charged track multiplicities for p+Be and p+C interactions at 58 GeV/c

	N_{evt}	ϵ_{trig}(data)	ϵ_{trig}(MC-BB)	ϵ_{trig}(MC-SciHi)	ϵ_{trig}(final)	$\Delta\epsilon_{trig}$
Be, 58 GeV/c	3(6)	1.00(?)±?	0.83±0.004	0.82±0.004	0.82	±0.10
C, 58 GeV/c	5(6)	0.80(?)±0.18	0.85±0.001	0.84±0.001	0.84	±0.10

Table 14: Summary of the trigger efficiency studies for p+Be and p+C interactions at 58 GeV/c. Last two columns represent assigned the final trigger efficiency and the systematic uncertainty.

11.4 Trigger efficiency for p+Bi and p+U at 58 GeV/c

Figure 56 shows the trigger scintillator pulse height distributions for the p+Bi and p+U interactions at 58 GeV/c.

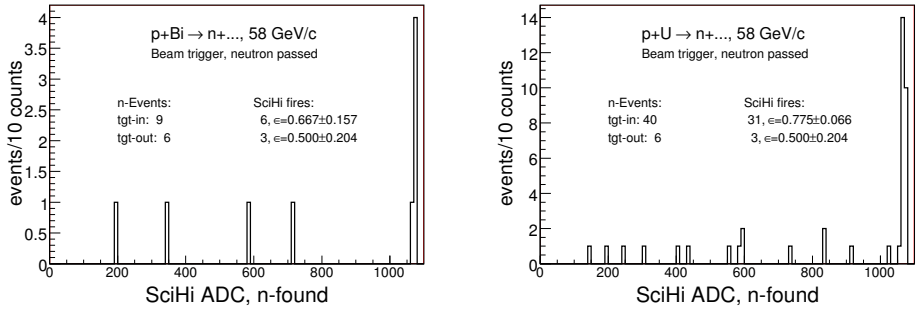

Figure 56: The "SciHi" pulse height distributions for p+Bi (left) and p+U (right) interactions with 58 GeV/c proton beam triggers, respectively.

Figure 57 shows the charged track multiplicities for the p+U interactions at 58 GeV/c.

Figure 58 shows the trigger efficiency as a function of the neutron momentum for p+Bi interactions at 58 GeV/c.

Figure 59 shows the trigger efficiency as a function of the neutron momentum for p+U interactions at 58 GeV/c.

The charged track multiplicities passing through the trigger scintillator for p+Bi and p+U interactions at 58 GeV/c are summarized in Table 15.

The trigger efficiency study for p+Bi and p+U interactions at 58 GeV/c are summarized in Table 16.

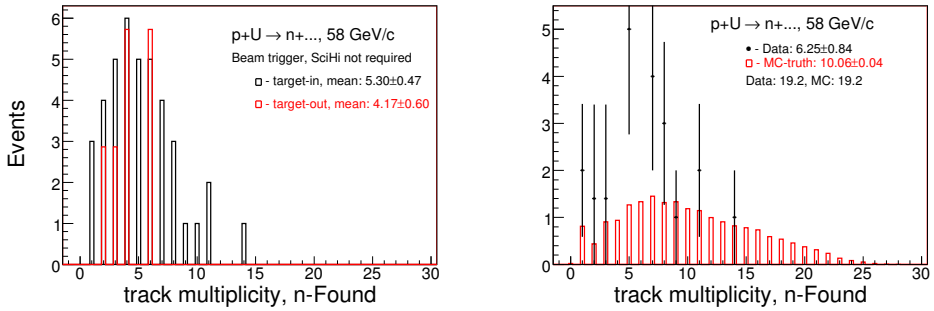

Figure 57: The charged track multiplicities for p+U interactions using 58 GeV/c proton beam triggers for data (left) and Monte Carlo superimposed (right), respectively.

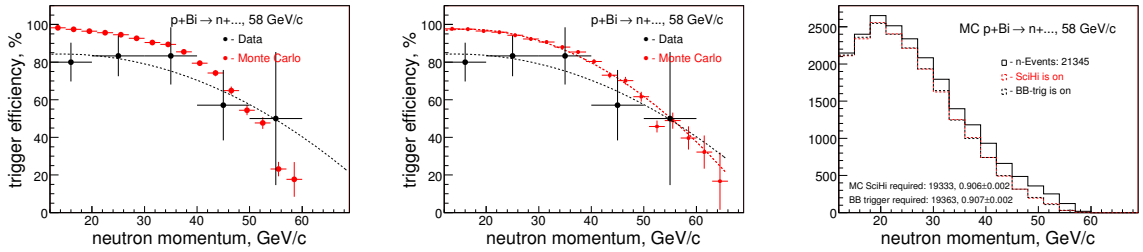

Figure 58: The trigger efficiency as a function of the neutron momentum for p+Bi interactions at 58 GeV/c: Monte Carlo efficiency dependence without (left) and with (right) the neutron momentum smearing applied and MC average trigger efficiency (right).

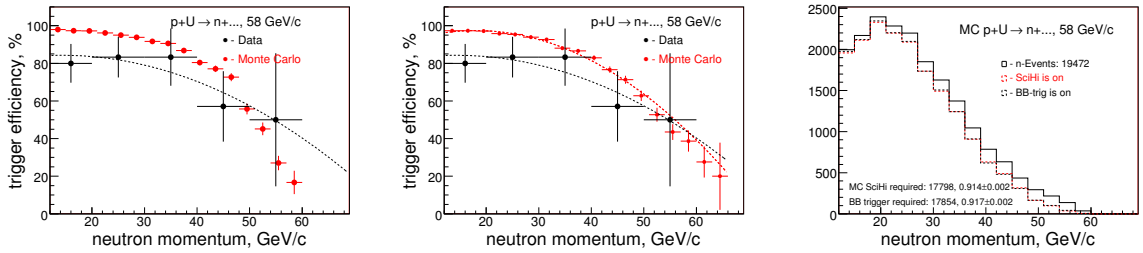

Figure 59: The trigger efficiency as a function of the neutron momentum for p+U interactions at 58 GeV/c: Monte Carlo efficiency dependence without (left) and with (right) the neutron momentum smearing applied and MC average trigger efficiency (right).

	N_{trk}(beam-tr)	N_{trk}(intr-tr)	N_{trk}(MC-true)	N_{trk}(MC-reco)
Bi, 58 GeV/c	n/a	6.96(8.87)±0.19	9.76±0.04	8.31±0.03
U, 58 GeV/c	5.30(6.25)±0.50	6.65(7.29)±0.07	10.06±0.04	8.52±0.03

Table 15: Summary of the charged track multiplicities for p+Be and p+C interactions at 58 GeV/c. For U target MC multiplicity is 8.52/6.25=1.36 times higher than in data. Due to of that the MC trigger efficiency could be overestimated.

	N_{evt}	ϵ_{trig}(data)	ϵ_{trig}(MC-BB)	ϵ_{trig}(MC-SciHi)	ϵ_{trig}(final)	$\Delta\epsilon_{trig}$
Bi, 58 GeV/c	9(6)	0.67(?)±0.16	0.91±0.002	0.91±0.002	0.845	±0.10
U, 58 GeV/c	40(6)	0.78(?)±0.07	0.92±0.002	0.91±0.002	0.845	±0.10

Table 16: Summary of the trigger efficiency studies for p+Bi and p+U interactions at 58 GeV/c. Note: the efficiencies based on data have high level of statistical uncertainties. Last two columns represent the final trigger efficiency and the systematic uncertainty.

11.5 Trigger efficiency for p+p at 84 GeV/c

Figure 60 shows the trigger scintillator pulse height distributions for the p+p interactions at 84 GeV/c using the liquid hydrogen target data for target-in (on left) and target-out subtraction applied (on right), respectively.

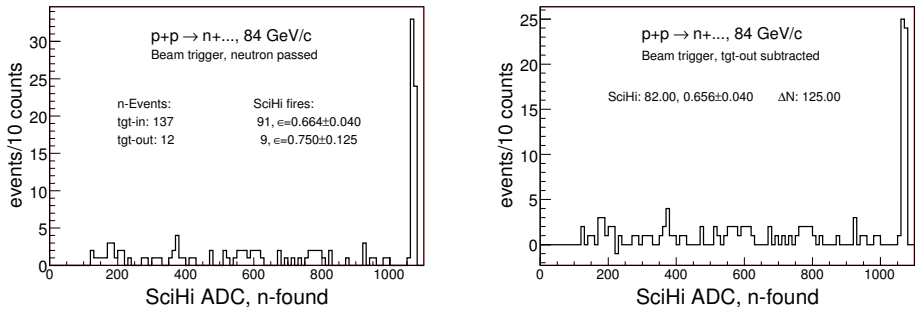

Figure 60: The "SciHi" pulse height distributions for the liquid hydrogen target data using 20 GeV/c proton beam triggers for target-in (on left) and target-out subtraction applied (on right), respectively.

Figure 61 shows the charged track multiplicities for the p+p interactions at 84 GeV/c.

Figure 62 shows the trigger efficiency as a function of the neutron momentum for p+p interactions at 84 GeV/c.

The trigger efficiency study for p+p interactions at 84 GeV/c are summarized in Table 17.

Why the trigger efficiency at 84 GeV/c is lower than at 58 GeV/c? Let's compare

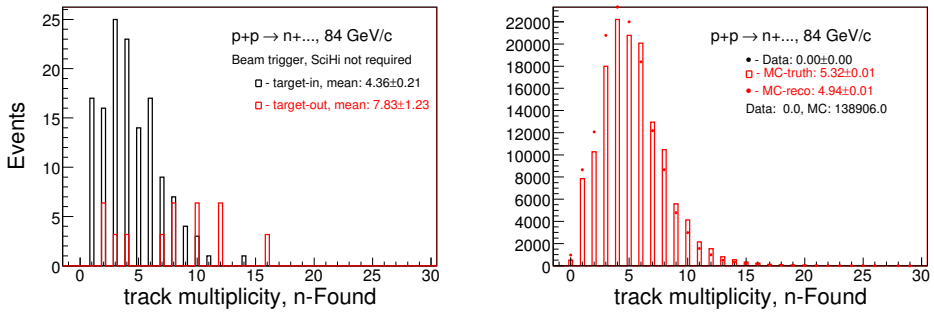

Figure 61: The charged track multiplicities for the liquid hydrogen target using 84 GeV/c proton beam triggers for data (left) and Monte Carlo (right), respectively.

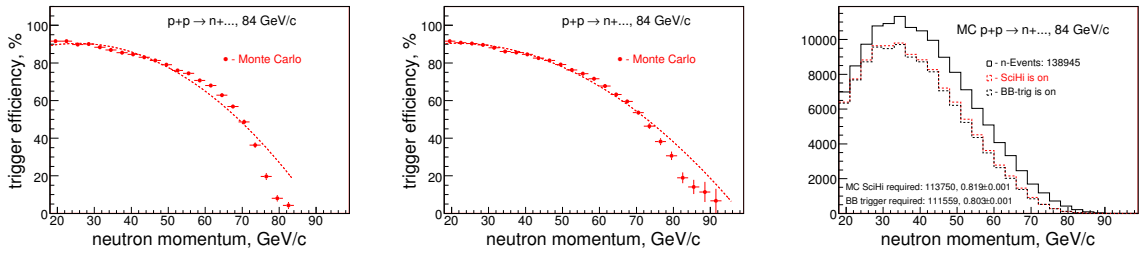

Figure 62: The trigger efficiency as a function of the neutron momentum for p+p interactions at 84 GeV/c: Monte Carlo efficiency dependence without (left) and with (middle) the neutron momentum smearing applied and MC average trigger efficiency (right).

N_{evt}	ϵ_{trig}(data)	ϵ_{trig}(MC-BB)	ϵ_{trig}(MC-SciHi)	ϵ_{trig}(final)	$\Delta\epsilon_{trig}$
137(12)	0.66(0.66)±0.04	0.82±0.001	0.80±0.001	0.73	±0.10

Table 17: Summary of the trigger efficiency studies for p+p interactions at 84 GeV/c. Last two columns represent assigned final trigger efficiency and systematic uncertainty.

SciHi rates for these two datasets. Figure 63 shows the SciHi fires rate as a function of the dataset number for both 58 and 84 GeV/c datasets using the beam triggers.

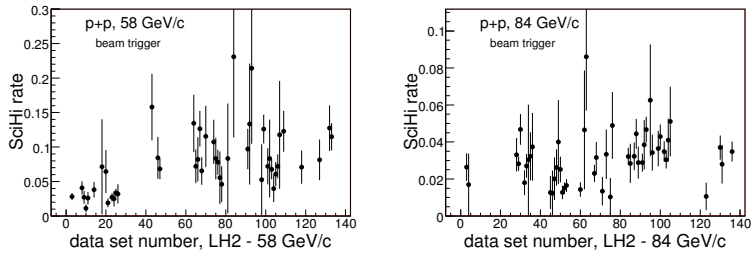

Figure 63: The SciHi fires rate as a function of the dataset number for both 58 GeV/c (left) and 84 GeV/c (right) using the beam triggers. Each data point on figures represents a single run number. Plots indicates that the SciHi fires at 84 GeV/c occurs at least twice lower than at 58 GeV/c.

Figure 64 shows the SciHi fires rate as a function of the dataset number for both 58 and 84 GeV/c datasets using the proton interaction triggers.

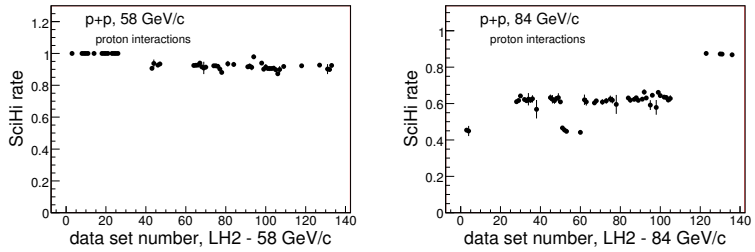

Figure 64: The SciHi fires rate as a function of the dataset number for both 58 GeV/c (left) and 84 GeV/c (right) using the proton interaction triggers. Each data point on figures represents a single run number. Plots indicates that the SciHi fires at 84 GeV/c occurs about 30% lower than at 58 GeV/c.

Figure 65 shows the SciHi ADC distributions for 58 and 84 GeV/c data using the beam triggers.

Figure 66 shows the SciHi ADC distributions for 58 and 84 GeV/c data using the beam triggers.

11.6 Trigger efficiency for p+Be at 120 GeV/c

Figure 67 shows the trigger scintillator pulse height distributions for the p+Be interactions at 120 GeV/c.

Figure 68 shows the trigger efficiency as a function of the neutron momentum for p+Be interactions at 120 GeV/c.

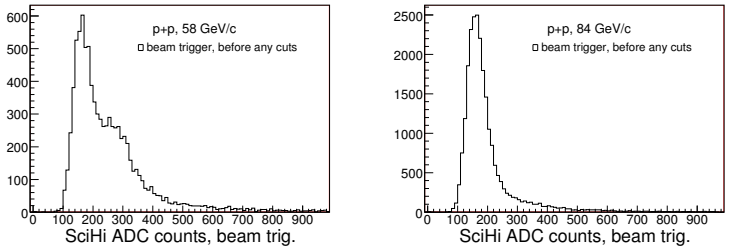

Figure 65: The SciHi ADC distributions for 58 (left) and 84 GeV/c (right) data using the beam triggers.

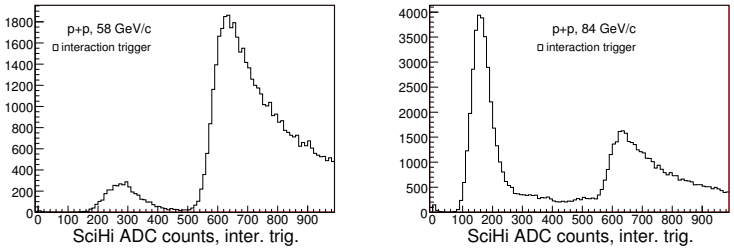

Figure 66: The SciHi ADC distributions for 58 (left) and 84 GeV/c (right) data using the proton interaction triggers. Left plot indicates that the trigger at 58 GeV mainly caused by SciHi with small straight through contamination. While 84 GeV data (right) mainly was triggered by iDC and it highly populated with the straight through. That can lead to the lower efficiency at 84 GeV in compare with 58 GeV data. Unfortunately, Monte Carlo could not able to reproduce these effects. Due to of that as the central value of trigger efficiency we used what was derived from data, while the momentum dependence follows according to Monte Carlo curve. So, Monte Carlo trigger efficiency function values were scaled down by coefficient of 0.82

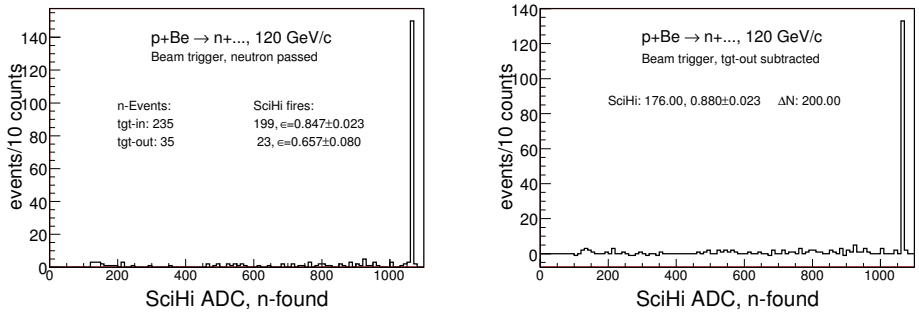

Figure 67: The "SciHi" pulse height distributions for p+Be interactions at 120 GeV/c: for target-in (left) and target-out subtraction applied (right), respectively.

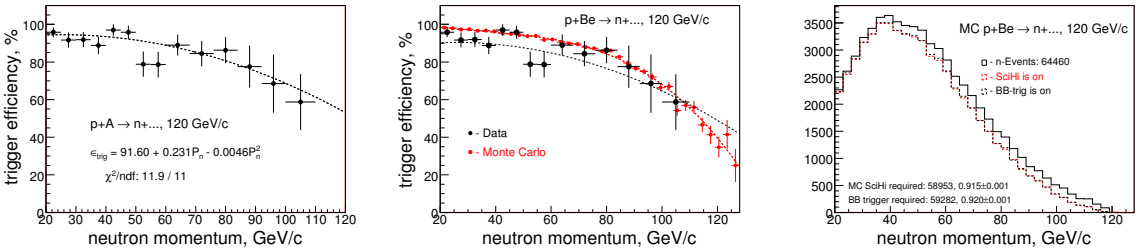

Figure 68: The trigger efficiency as a function of the neutron momentum for p+Be interactions at 120 GeV/c. Combined fit, Be and Bi data values are scaled to the C (left), predicted MC behavior (middle) and the average MC predictions (right). Monte Carlo efficiency dependence was made with the neutron momentum smearing applied.

Figure 69 shows the charged track multiplicities for the p+Be interactions at 120 GeV/c.

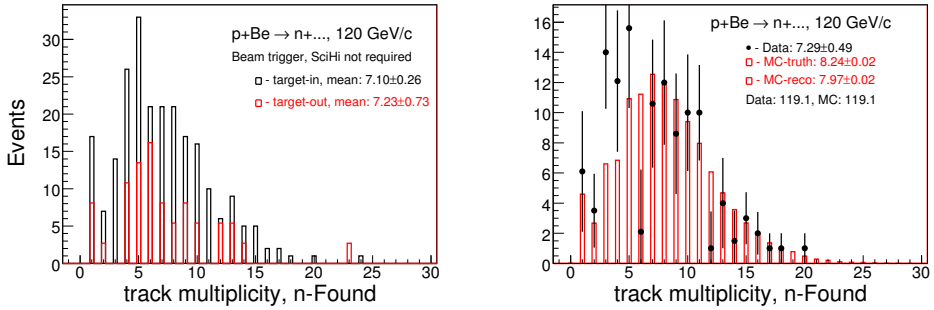

Figure 69: The charged track multiplicities for p+Be interactions at 120 GeV/c for data (left) and Monte Carlo superimposed (right), respectively.

The charged track multiplicities passing through the trigger scintillator for p+Be interactions at 120 GeV/c are summarized in Table 18.

The trigger efficiency study for p+Be interactions at 120 GeV/c are summarized in Table 19.

11.7 Trigger efficiency for p+C at 120 GeV/c

Figure 70 shows the trigger scintillator pulse height distributions for the p+C interactions at 120 GeV/c.

Figure 71 shows the trigger efficiency as a function of the neutron momentum for p+C interactions at 120 GeV/c.

Figure 72 shows the charged track multiplicities for the p+C interactions at 120 GeV/c.

N_{trk}(beam-tr)	N_{trk}(intr-tr)	N_{trk}(MC-true)	N_{trk}(MC-reco)
7.10(7.3)±0.49	7.9(7.8)±0.02	8.2±0.02	8.0±0.02

Table 18: Summary of the charged track multiplicities for p+Be interactions at 120 GeV/c. MC multiplicity is 8.0/7.3=1.1 times higher than in data. Both multiplicities and MC average efficiency suggests that ϵ_{trig}=0.99 looks unreasonable.

N_{evt}	ϵ_{trig}(data)	ϵ_{trig}(MC-BB)	ϵ_{trig}(MC-SciHi)	ϵ_{trig}(final)	$\Delta\epsilon_{trig}$
235(35)	0.85(0.88)±0.03	0.92±0.001	0.92±0.001	0.885	±0.07

Table 19: Summary of the trigger efficiency studies for p+Be interactions at 120 GeV/c. What to use as the average trigger efficiency: 0.84(data) or 0.92(MC)? The value 0.84 is way off, however MC average is slightly overestimated. We might use MC value and assign 0.08 as systematic uncertainty.

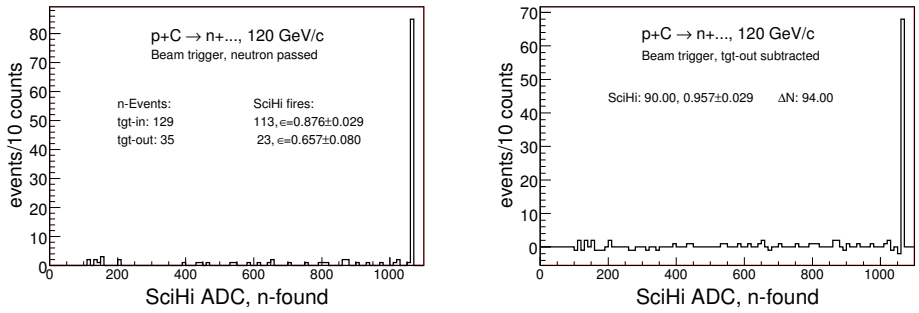

Figure 70: The "SciHi" pulse height distributions for p+C interactions at 120 GeV/c: for target-in (left) and target-out subtraction applied (right), respectively.

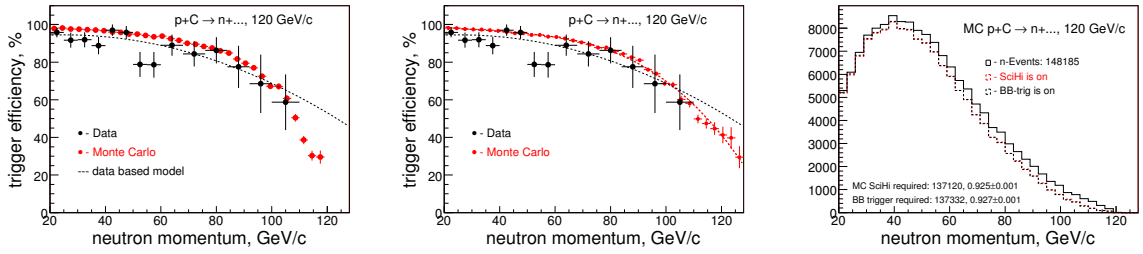

Figure 71: The trigger efficiency as a function of the neutron momentum for p+C interactions at 120 GeV/c: Monte Carlo efficiency dependence without (left) and with (right) the neutron momentum smearing applied and MC average trigger efficiency (right).

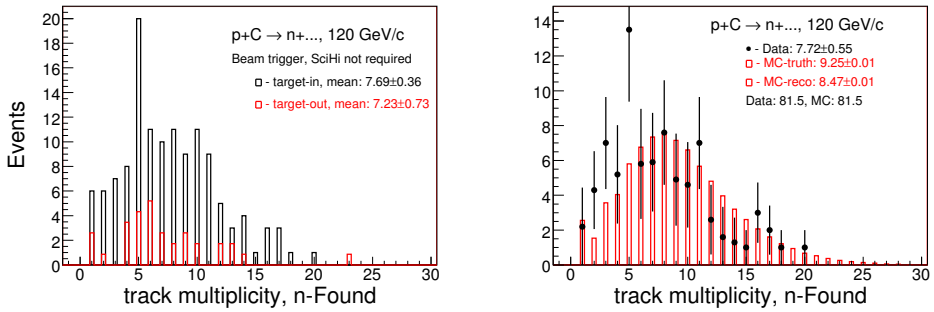

Figure 72: The charged track multiplicities for p+C interactions at 120 GeV/c for data (left) and Monte Carlo superimposed (right), respectively.

The charged track multiplicities passing through the trigger scintillator for p+C interactions at 120 GeV/c are summarized in Table 20.

N_{trk}(beam-tr)	N_{trk}(intr-tr)	N_{trk}(MC-true)	N_{trk}(MC-reco)
7.7(7.7)±0.55	8.3(8.4)±0.02	9.3±0.01	8.5±0.01

Table 20: Summary of the charged track multiplicities for p+C interactions at 120 GeV/c. MC multiplicity is 8.5/7.7=1.1 times higher than in data. Both multiplicities and MC average efficiency suggests that ϵ_{trig}=0.96 looks unreasonable.

The trigger efficiency study for p+C interactions at 120 GeV/c are summarized in Table 21.

N_{evt}	ϵ_{trig}(data)	ϵ_{trig}(MC-BB)	ϵ_{trig}(MC-SciHi)	ϵ_{trig}(final)	$\Delta\epsilon_{trig}$
129(35)	0.88(0.96?)±0.03	0.93±0.001	0.93±0.001	0.905	±0.05

Table 21: Summary of the trigger efficiency studies for p+C interactions at 120 GeV/c. Last two columns represent assigned the final trigger efficiency and the systematic uncertainty.

11.8 Trigger efficiency for p+Bi at 120 GeV/c

Figure 73 shows the trigger scintillator pulse height distributions for the p+Be interactions at 120 GeV/c.

Figure 74 shows the trigger efficiency as a function of the neutron momentum for p+Bi interactions at 120 GeV/c.

Figure 75 shows the charged track multiplicities for the p+Bi interactions at 120 GeV/c.

The charged track multiplicities passing through the trigger scintillator for p+Bi interactions at 120 GeV/c are summarized in Table 22.

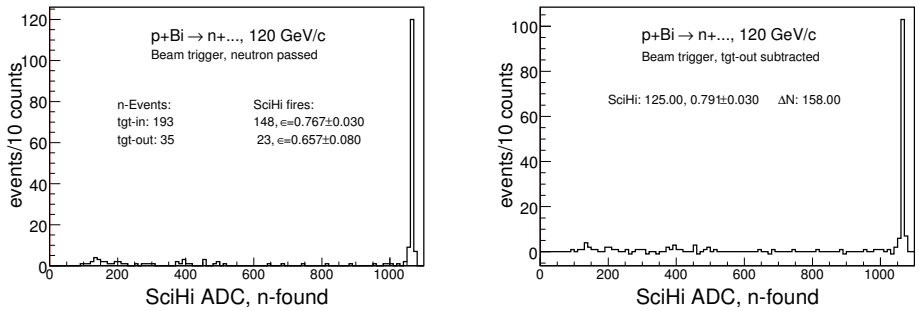

Figure 73: The "SciHi" pulse height distributions for p+Be interactions at 120 GeV/c: for target-in (left) and target-out subtraction applied (right), respectively.

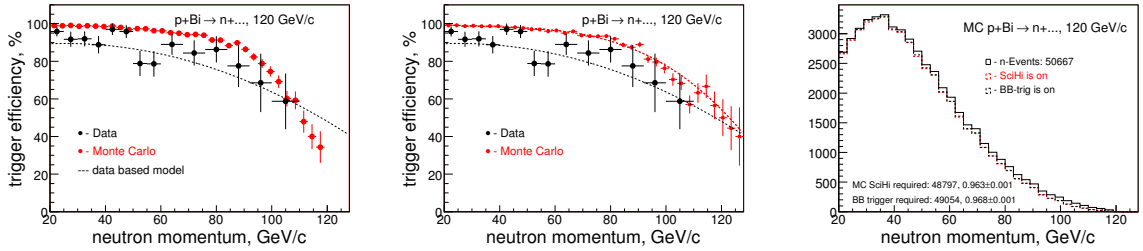

Figure 74: The trigger efficiency as a function of the neutron momentum for p+Bi interactions at 120 GeV/c: Monte Carlo efficiency dependence without (left) and with (right) the neutron momentum smearing applied and MC average trigger efficiency (right).

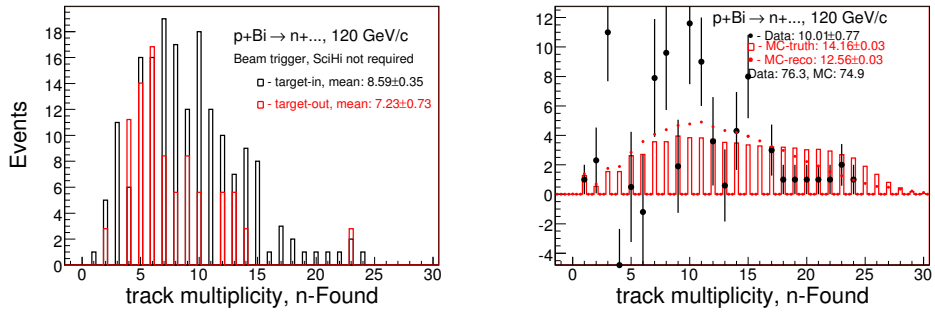

Figure 75: The charged track multiplicities for p+Bi interactions at 120 GeV/c for data (left) and Monte Carlo superimposed (right), respectively.

N_{trk}(beam-tr)	N_{trk}(intr-tr)	N_{trk}(MC-true)	N_{trk}(MC-reco)
8.6(10.0)±0.77	9.6(11.0)±0.05	14.23±0.03	12.62±0.03

Table 22: Summary of the charged track multiplicities for p+Bi interactions at 120 GeV/c. MC multiplicity is 12.62/10.0=1.26 times higher than in data. Due to of that the MC trigger efficiency could be overestimated.

The trigger efficiency study for p+Bi interactions at 120 GeV/c are summarized in Table 23.

N_{evt}	ϵ_{trig}(data)	ϵ_{trig}(MC-BB)	ϵ_{trig}(MC-SciHi)	ϵ_{trig}(final)	$\Delta\epsilon_{trig}$
193(35)	0.77(0.79)±0.03	0.96±0.001	0.97±0.001	0.87	±0.10

Table 23: Summary of the trigger efficiency studies for p+Bi interactions at 120 GeV/c. Last two columns represent assigned the final trigger efficiency and the systematic uncertainty.

The charged particles multiplicities for the Monte Carlo non-neutron samples are given in Appendix E.

12 Neutron Production Properties Depending on Generator

We considered the particles production multiplicities, the true neutron spectra and the neutron an angular distribution. Comparison made for FLUKA/DPMJET and LAQGSM generators. DPMJET used for p+p interactions at 58 GeV/c only.

12.1 General particle multiplicities

Below we compare the particle production multiplicities of FLUKA and LAQGSM [5, 6, 7] generators calculated per single p+A interaction.

The particles multiplicity production from p+p, p+C and p+Bi interactions at 58 GeV/c using Fluka and LAQGSM models are shown in Table 24.

58 GeV/c	p+p		p+C		p+Bi	
	DPMJET	LAQGSM	FLUKA	LAQGSM	FLUKA	LAQGSM
π^+	2.71	1.81	2.05	2.84	1.97	5.35
π^-	2.00	1.28	1.82	2.50	1.89	5.81
K^+	0.21	0.15	0.16	0.25	0.16	0.48
K^-	0.11	0.10	0.09	0.15	0.09	0.20
p	1.59	1.41	1.65	2.86	3.10	11.01
n	0.68	0.52(0.51)	1.49	2.61(1.20)	3.20	32.27(4.49)
Total (charged)	6.62	4.75	5.77	8.60	7.21	22.85

Table 24: The particles multiplicity production from p+p, p+C and p+Bi interactions at 58 GeV/c using Fluka and LAQGSM generators. The multiplicities are calculated per single interaction. The number of neutrons in parenthesis represents yield with p_n >100 MeV/c threshold.

The particles multiplicity production from p+p, p+C and p+Bi interactions at 120 GeV/c using Fluka and LAQGSM models are shown in Table 25.

12.2 MC neutron production per single p+A interaction

Figure 76 shows the neutron production spectra and rates normalized per single p+p interactions at 20, 58 and 84 GeV/c.

Figure 77 shows the neutron production spectra and rates normalized per single p+Be or p+C interactions at 58 GeV/c.

Figure 78 shows the neutron production spectra and rates normalized per single p+Bi or p+U interactions at 58 GeV/c.

Figure 79 shows the neutron production spectra and rates normalized per single p+Be, p+C or p+Bi interactions at 120 GeV/c.

120 GeV/c	p+p		p+C		p+Bi	
	DPMJET	LAQGSM	FLUKA	LAQGSM	FLUKA	LAQGSM
π^+	-	2.36	2.56	3.87	2.53	7.72
π^-	-	1.82	2.33	3.53	2.46	8.24
K^+	-	0.25	0.21	0.41	0.22	0.79
K^-	-	0.18	0.13	0.28	0.14	0.39
p	-	1.39	1.67	2.97	2.92	11.88
n	-	0.54(0.52)	1.53	2.74(1.26)	3.16	33.69(4.99)
Total (charged)	-	6.00	6.90	11.06	8.27	29.02

Table 25: The particles multiplicity production from p+p, p+C and p+Bi interactions at 120 GeV/c using Fluka and LAQGSM generators. The multiplicities are calculated per single interaction. The number of neutrons in parenthesis represents yield with p_n >100 MeV/c threshold.

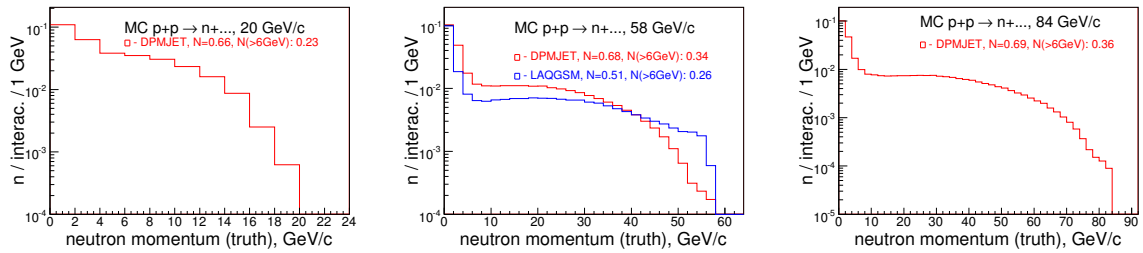

Figure 76: The neutron production spectra and rates normalized per single p+p interactions at 20 GeV/c (left), 58 GeV/c (middle) and 84 GeV/c (right) using FLUKA and LAQGSM (if possible).

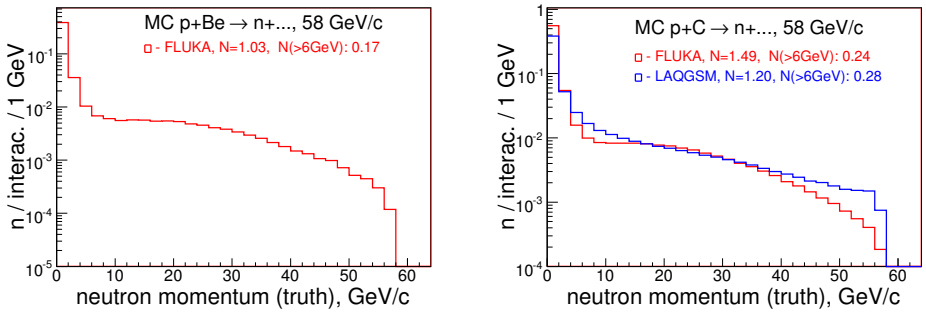

Figure 77: The neutron production spectra and rates normalized per single p+Be (left) or p+C (right) interactions at 58 GeV/c using FLUKA and LAQGSM (if possible).

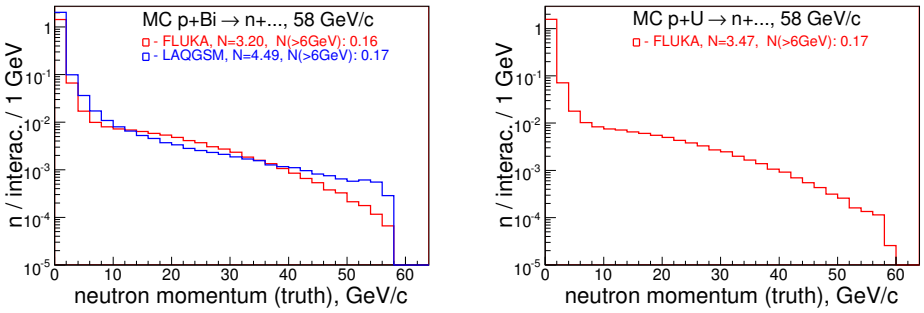

Figure 78: The neutron production spectra and rates normalized per single p+Bi (left) and p+U (right) interactions at 58 GeV/c using FLUKA and LAQGSM (if possible).

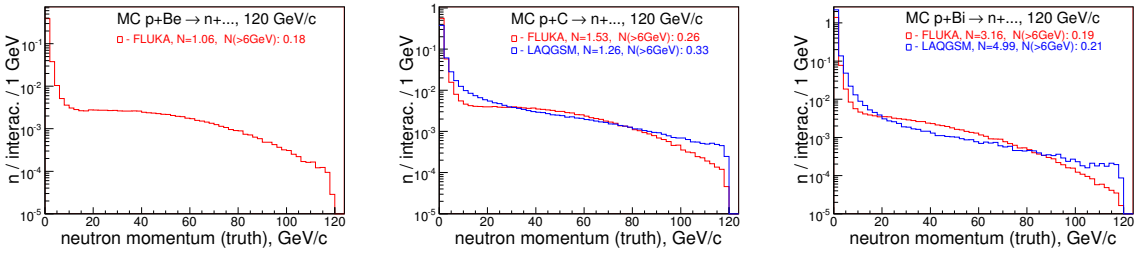

Figure 79: The neutron production spectra and rates normalized per single p+Be (left), p+C (middle) and p+Bi (right) interactions at 120 GeV/c using FLUKA and LAQGSM (if possible).

Table 26 illustrates Monte Carlo neutron production rates per single p+A interaction with p_n >100 MeV/c threshold.

	FLUKA	LAQGSM
H_2-20	0.66	
H_2-58	0.68	0.51
Be-58	1.03	
C-58	1.49	1.20
Bi-58	3.20	4.49
U-58	3.47	
H_2-84	0.69	
Be-120	1.06	
C-120	1.53	1.26
Bi-120	3.16	4.99

Table 26: Summary of Monte Carlo neutron production rates per single p+A interaction with p_n >100 MeV/c threshold. FLUKA column for H_2 target actually done with DPMJET generator.

Figure 80 shows the neutron p_T spectra normalized per single p+A interactions at 58 and 120 GeV/c.

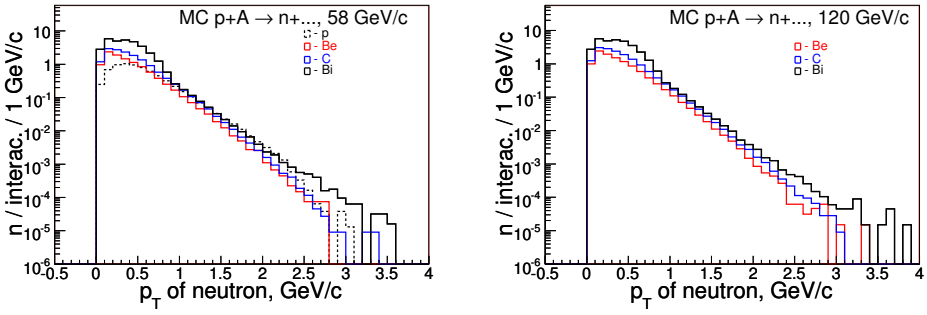

Figure 80: The neutron p_T spectra normalized per single p+A interactions at 58 (left) and 120 GeV/c (right) using FLUKA generator. Prediction for p target at 58 GeV/c was done by DPMJET.

12.3 Neutron spectra with $p_n > p_{min}$

Figure 81 shows the true neutron production spectra from p+p interactions at 20, 58 and 84 GeV/c using FLUKA and LAQGSM models.

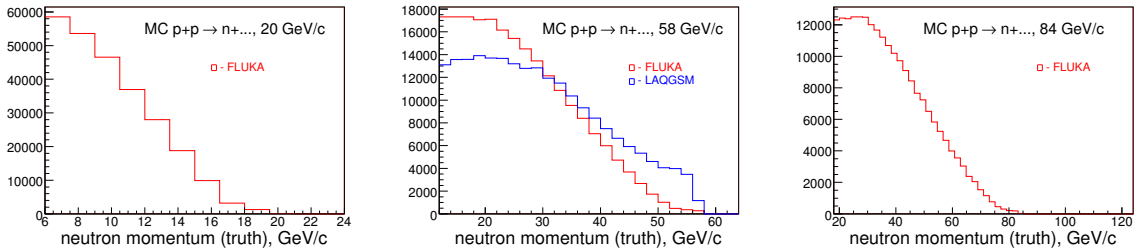

Figure 81: The true neutron production spectra from the p+p interactions at 20 GeV/c (left), 58 GeV/c (middle) and 84 GeV/c using FLUKA and LAQGSM (where it was possible) models.

Figure 82 shows the true neutron production spectra from p+Be and p+C interactions at 58 GeV/c using FLUKA and LAQGSM models.

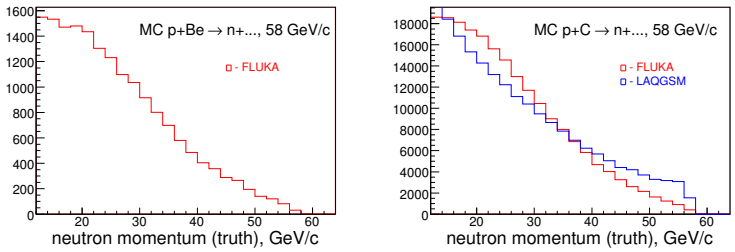

Figure 82: The true neutron production spectra from the p+Be (left) and p+C (right) interactions at 58 GeV/c using FLUKA and LAQGSM models.

Figure 83 shows the true neutron production spectra for the p+Bi and p+U interactions at 58 GeV/c using FLUKA and LAQGSM models.

Figure 84 shows the true neutron production spectra from p+Be, p+C and p+Bi interactions at 120 GeV/c using FLUKA and LAQGSM models.

12.4 Neutron an angular distribution

The neutron angular distribution effecting the calorimeter acceptance. Below we compare the neutron exit angle, a p_T/p_{tot} variable, from Fluka and LAQGSM [5, 6, 7] generators.

Figure 85 shows the p_T/p_{tot} quantity distributions for p+p at 20, 58 and 84 GeV/c using Fluka and LAQGSM models (where it was available).

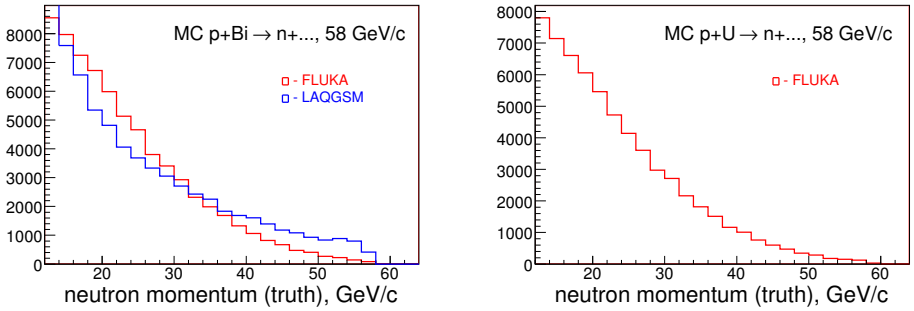

Figure 83: The true neutron production spectra from p+Bi (left) and p+U (right) interactions at 58 GeV/c using FLUKA and LAQGSM models.

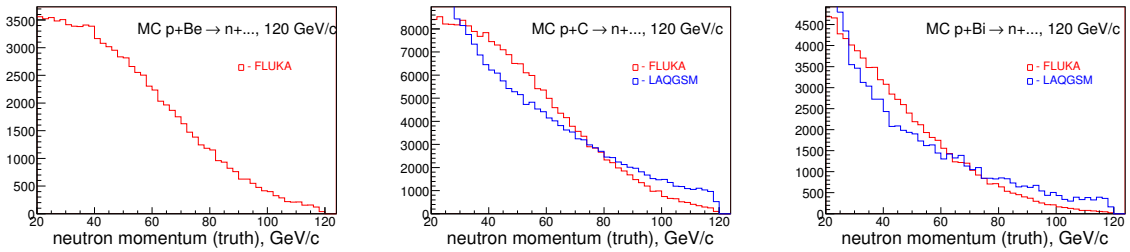

Figure 84: The true neutron production spectra from p+Be (left), p+C (middle) and p+Bi (right) interactions at 120 GeV/c using FLUKA and LAQGSM models.

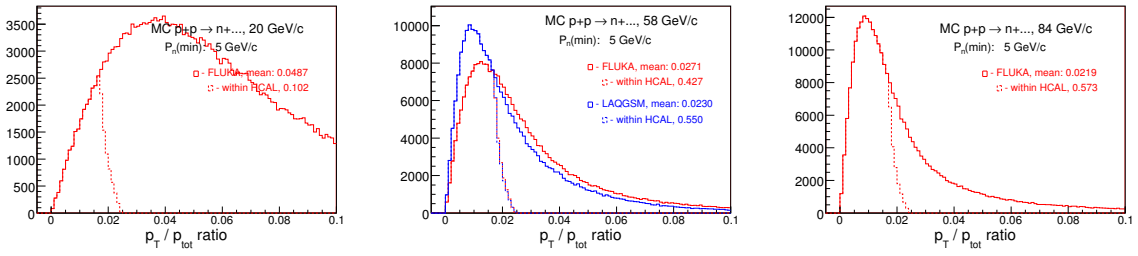

Figure 85: The p_T/p_{tot} distributions for neutrons from p+p at 20 GeV/c (left), 58 GeV/c (middle) and 84 GeV/c (right) using Fluka and LAQGSM models.

Figure 86 shows the p_T/p_{tot} quantity distributions for p+Be and p+C interactions at 58 GeV/c using Fluka and LAQGSM models.

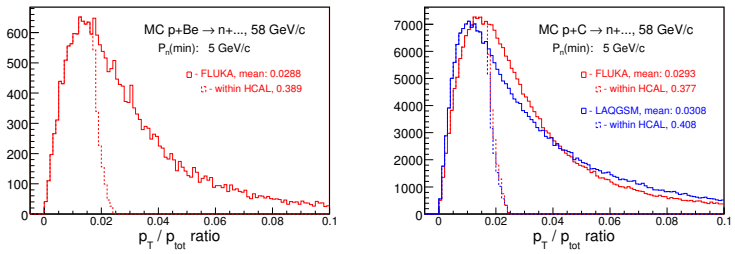

Figure 86: The p_T/p_{tot} distributions for neutrons from p+Be (left) and p+C (right) interactions at 58 GeV/c using Fluka and LAQGSM models.

Figure 87 shows the p_T/p_{tot} quantity distributions for p+Bi and p+U interactions at 58 GeV/c using Fluka and LAQGSM models.

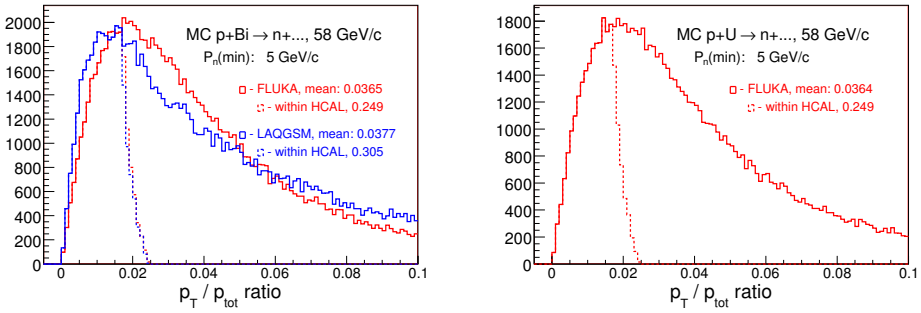

Figure 87: The p_T/p_{tot} distributions for neutrons from p+Bi (left) and p+U (right) interactions at 58 GeV/c using Fluka and LAQGSM models.

Figure 88 shows the p_T/p_{tot} quantity distributions for p+Be. p+C and p+U interactions at 120 GeV/c using Fluka and LAQGSM models..

13 Summary of the Neutron Production: data vs Monte Carlo

Table 27 illustrates the summary of data and Monte Carlo neutron production properties. Neutron fractions were calculated per single p+A interactions with $p_n > p_{min}$ requirements.

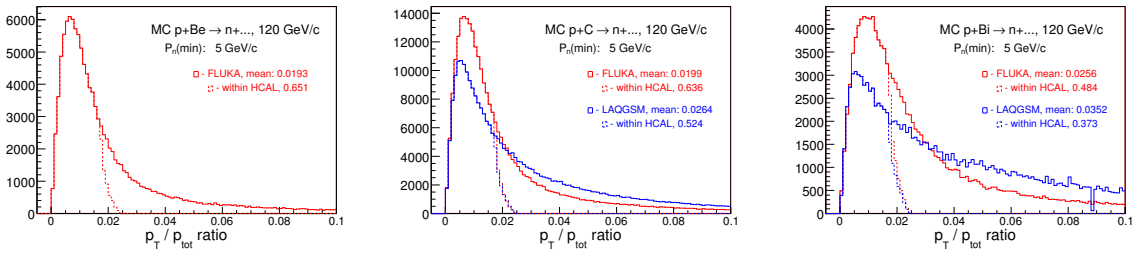

Figure 88: The p_T/p_{tot} distributions for neutrons from p+Be (left), p+C (middle) and p+Bi (right) interactions at 120 GeV/c using Fluka and LAQGSM models.

	N_{intr}(d)	F_n(data)	F_n(FL)	F_n(LA)	F_{non}(FL)
H_2-20	208786	0.0042±0.0002	0.014	-	0.502
H_2-58	2001048	0.0346±0.0005	0.111	0.109	0.450
Be-58	575635	0.0063±0.0004	0.104	-	0.154
C-58	1258291	0.0217±0.0005	0.102	0.099	0.156
Bi-58	1383354	0.0107±0.0003	0.066	0.047	0.091
U-58	1426534	0.0180±0.0003	0.067	-	0.094
H_2-84	2710439	0.0594±0.0003	0.162	-	0.438
Be-120	607457	0.0874±0.0003	0.201	-	0.151
C-120	319103	0.0966±0.0005	0.201	0.095	0.153
Bi-120	587048	0.0582±0.0002	0.156	0.042	0.105

Table 27: Summary of data and Monte Carlo neutron production properties. Neutron fractions were calculated per single p+A interactions with $p_n > p_{min}$ requirements.

14 Hadron calorimeter's solid angle

The solid angle, Ω, subtended at the center of a sphere of radius r by a portion of the surface S of the sphere is defined as: $\Omega = \frac{S}{r^2}$, where S is area of calorimeter in m^2, r = Z is a distance from the reconstructed interaction vertex up to HCAL front surface in m.

Calorimeter's designed surface area size is equal to $S = 0.989 \times 0.979 = 0.968$ m^2. An active surface area size can be estimated by Monte Carlo.

At this moment the Monte Carlo information about the neutron passage simulation and it's position at HCAL front surface is not available. But we have the projected positions. We applied following cuts to the neutron sample in Monte Carlo:

- select events when there only single high momentum neutron being generated, $p_n > p_{min}$
- require that the high momentum neutron directed toward downstream of the beam line, within ±80 cm from beam line in both views at Z equal to the the Z of HCAL front face. This sample represents the denominator
- calculate p_n(true) / p_n(HCAL) variable, where p_n(HCAL) is reconstructed neutron momentum according to the procedure same as in data
- select events when ratio value would be within 0.8-1.2 range. This sample represents the numerator
- make 2D Y-projection vs X-projection plot
- the edges of the 2D plot will tell what is the active calorimeter area size

Figure 89 shows the distributions of p_n(true)/p_n(HCAL) variable and the 2D X-Y-projection plot made using the p+C interactions at 58 GeV/c

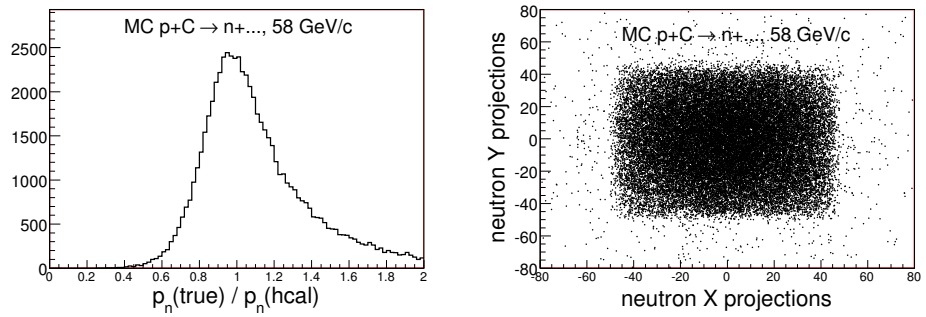

Figure 89: The distributions of p_n(true)/p_n(HCAL) variable (left) and the 2D X-Y-projection plot (right) made using the p+C interactions at 58 GeV/c

Figure 90 shows X and Y projections for subsample shown on Fig. 89 (right plot).

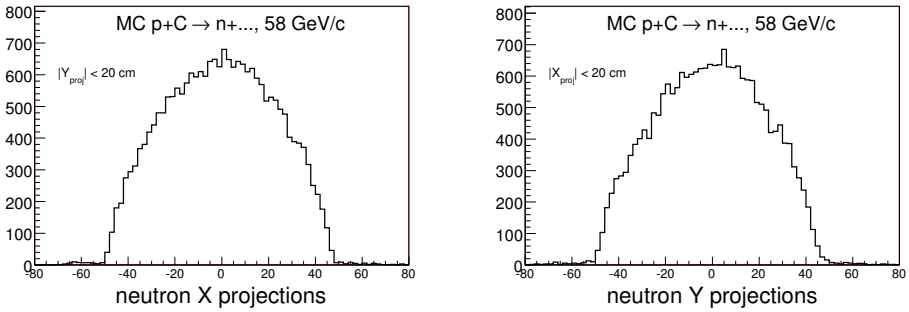

Figure 90: The X and Y projections for subsample shown on Fig. 89 (right plot).

Figure 91 shows the neutron reconstruction rates depending on X and Y projections.

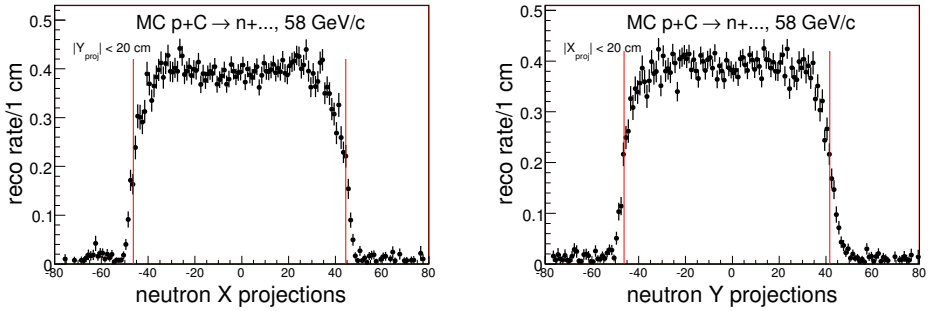

Figure 91: The neutron reconstruction rates depending on X and Y projections. The rate is a ratio of what shown on Fig. 90 over the generated sample.

The vertical red lines in Fig. 91 illustrates defined by the fit the X (or Y) position where the neutron rate reached 1/2 of it's maximum value. The active edges of the hadron calorimeter were found as: -46.39 cm and 44.47 cm in X view and -46.27 cm and 41.62 cm in Y view, respectively. Thus, the active surface area is equal to $0.9086 \times 0.8789 = 0.79857$ m^2. The uncertainty in the surface area value is ± 0.001 m^2 (or 0.0005 m in single estimate). Then, the expected solid angle value for the thin target would be: $\Omega = 0.7986 \,/\, 24.76^2 = 0.001302 \pm 0.000002$ (syst) steradians.

What is an angular coverage of the calorimeter? Our calorimeter front surface is a rectangular. An equivalent radius value can be found through the formula: $S = \pi r^2$, then $r = \sqrt{\frac{S}{\pi}}$. The equivalent radius would be $r = \sqrt{\frac{0.7986}{3.141593}} = 0.5047$ m. Thus, the angular coverage: $\sin\theta = \theta = \frac{0.5047}{24.76} = 0.0204$ radians, or 20.4 mrad.

Figure 92 shows the solid angle value distributions for p+p, p+C and p+Bi interactions at 58 GeV/c

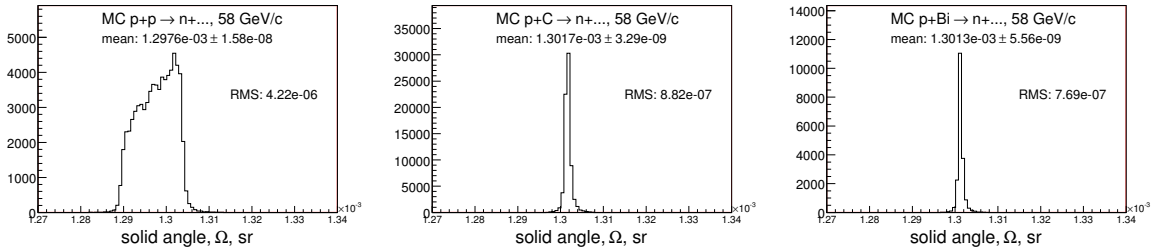

Figure 92: The solid angle value distributions for p+p, p+C and p+Bi interactions at 58 GeV/c.

Figure 93 shows the solid angle value distributions for p+p at 84 GeV/c and for p+C and p+Bi interactions at 120 GeV/c

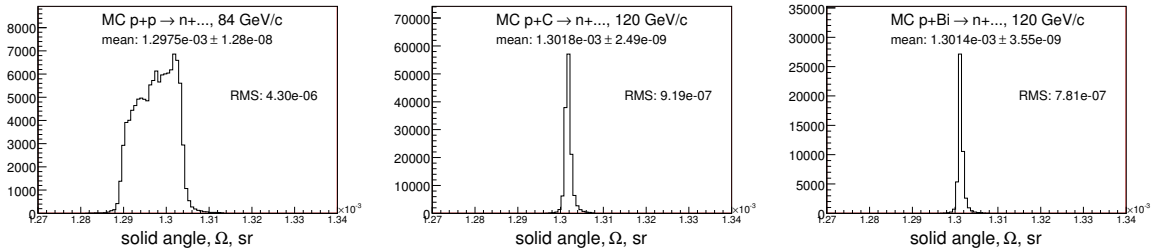

Figure 93: The solid angle value distributions for p+p at 84 GeV/c and p+C and p+Bi interactions at 120 GeV/c.

Table 28 illustrates the summary of the solid angle values calculated for the active and designed front surface area of the hadron calorimeter.

	$\Omega_{active}\times10^3$,sr	$\mathrm{RMS}_\Omega\times10^6$	$\Omega_{design}\times10^3$,sr	$\Delta\Omega$(assign)
H_2-20	1.2986	3.89	1.5742	0.003
H_2-58	1.2976	4.22	1.5729	0.003
Be-58	1.3014	0.82	1.5775	0.002
C-58	1.3017	0.88	1.5779	0.002
Bi-58	1.3013	0.77	1.5774	0.002
U-58	1.3014	0.75	1.5775	0.002
H_2-84	1.2975	4.30	1.5728	0.003
Be-120	1.3015	0.92	1.5777	0.002
C-120	1.3018	0.92	1.5781	0.002
Bi-120	1.3014	0.78	1.5775	0.002

Table 28: Summary of Ω values.

15 Calorimeter Acceptance

The geometrical acceptance of the calorimeter is certain. However, as was shown on previous section that the neutron angular distribution is model dependent. Due to of this fact the calorimeter acceptance would depend on what model in use. So, we used two Monte Carlo generators: FLUKA and LAQGSM [5, 6, 7] generators to see for the possible variations in acceptance.

Figure 94 shows the neutron spectra and calorimeter acceptance as the function of the neutron momentum from p+p interactions at 20 GeV/c.

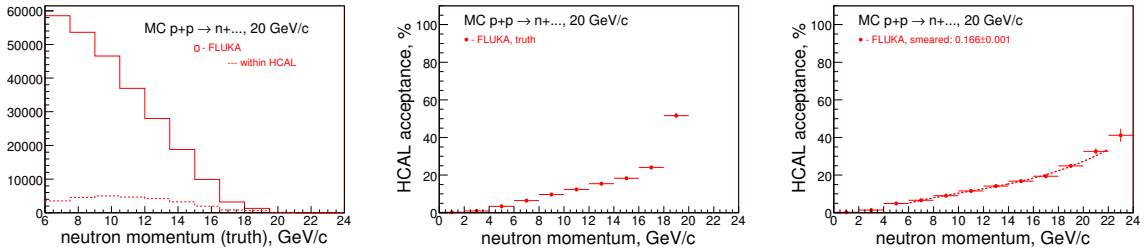

Figure 94: Neutron spectra and calorimeter acceptance as the function of the neutron momentum from p+p interactions at 20 GeV/c. Left: neutron spectra with and without HCAL fiducial requirements. Calorimeter acceptance without (left) and with (right) Fluka neutron smearing applied.

Figure 95 shows the neutron spectra and calorimeter acceptance as the function of the neutron momentum from p+p interactions at 58 GeV/c.

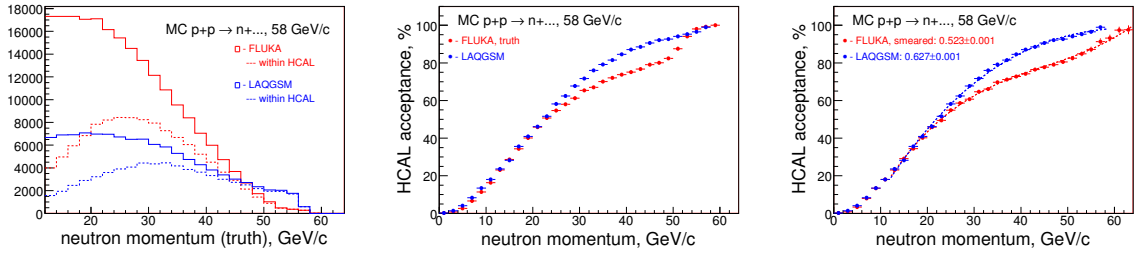

Figure 95: Neutron spectra and calorimeter acceptance as the function of the neutron momentum from p+p interactions at 58 GeV/c. Left: neutron spectra with and without HCAL fiducial requirements. Calorimeter acceptance without (left) and with (right) Fluka neutron smearing applied.

Figure 96 shows the neutron spectra and calorimeter acceptance as the function of the neutron momentum from p+Be interactions at 58 GeV/c and HCAL acceptance.

Figure 97 shows the neutron spectra and calorimeter acceptance as the function of the neutron momentum from p+C interactions at 58 GeV/c and HCAL acceptance.

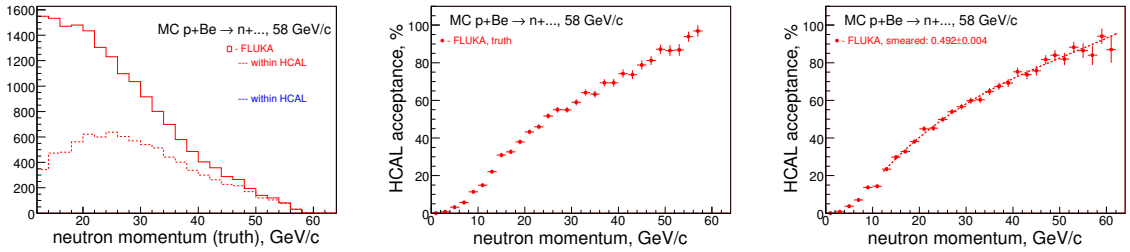

Figure 96: Neutron spectra and calorimeter acceptance as the function of the neutron momentum from p+Be interactions at 58 GeV/c. Left: neutron spectra with and without HCAL fiducial requirements. HCAL acceptance without (left) and with (right) Fluka neutron smearing applied.

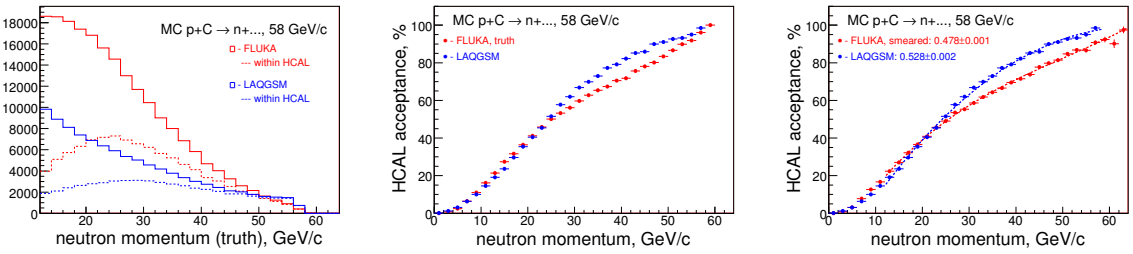

Figure 97: Neutron spectra and calorimeter acceptance as the function of the neutron momentum from p+C interactions at 58 GeV/c. Left: neutron spectra with and without HCAL fiducial requirements. HCAL acceptance without (left) and with (right) Fluka neutron smearing applied.

Figure 98 shows the neutron spectra and calorimeter acceptance as the function of the neutron momentum from p+Bi interactions at 58 GeV/c and HCAL acceptance.

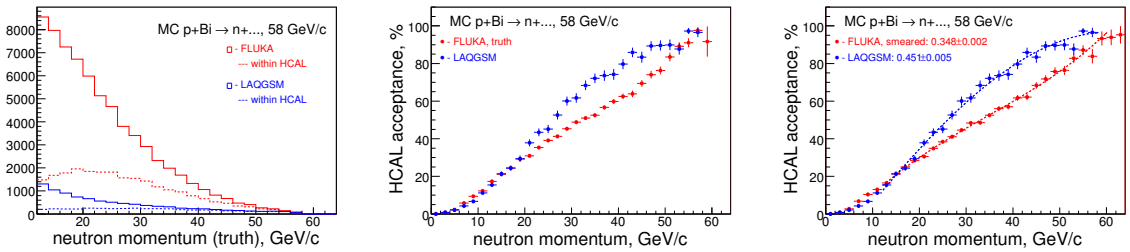

Figure 98: Neutron spectra and calorimeter acceptance as the function of the neutron momentum from p+Bi interactions at 58 GeV/c. Left: Neutron spectra with and without HCAL fiducial requirements. HCAL acceptance without (left) and with (right) Fluka neutron smearing applied.

Figure 99 shows the neutron spectra and calorimeter acceptance as the function of the neutron momentum from p+U interactions at 58 GeV/c and HCAL acceptance.

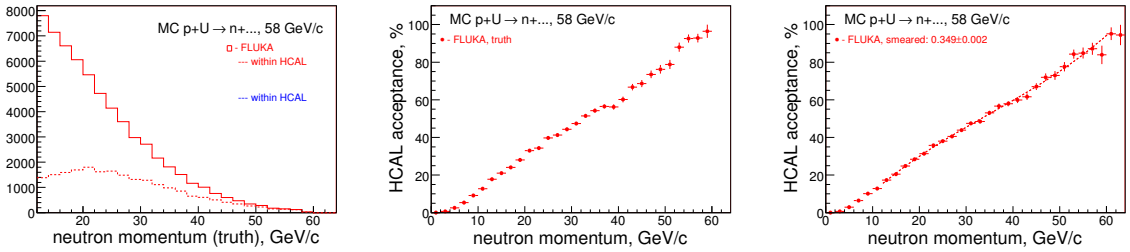

Figure 99: Neutron spectra and calorimeter acceptance as the function of the neutron momentum from p+U interactions at 58 GeV/c. Left: Neutron spectra with and without HCAL fiducial requirements. HCAL acceptance without (left) and with (right) Fluka neutron smearing applied.

Figure 100 shows the neutron spectra and calorimeter acceptance as the function of the neutron momentum from p+p interactions at 84 GeV/c.

Figure 101 shows the neutron spectra and calorimeter acceptance as the function of the neutron momentum from p+Be interactions at 120 GeV/c and HCAL acceptance.

Figure 102 shows the neutron spectra and calorimeter acceptance as the function of the neutron momentum from p+C interactions at 120 GeV/c and HCAL acceptance.

Figure 103 shows the neutron spectra and calorimeter acceptance as the function of the neutron momentum from p+Bi interactions at 120 GeV/c and HCAL acceptance.

Average HCAL acceptances for the various targets and beam momenta are summarized in Table 29.

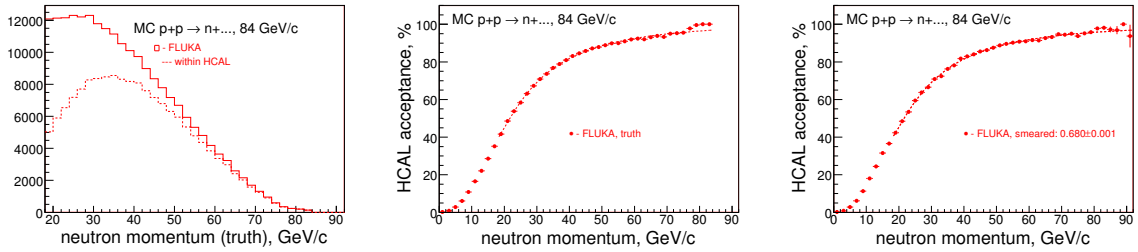

Figure 100: Neutron spectra and calorimeter acceptance as the function of the neutron momentum from p+p interactions at 84 GeV/c. Left: neutron spectra with and without HCAL fiducial requirements. Calorimeter acceptance without (left) and with (right) Fluka neutron smearing applied.

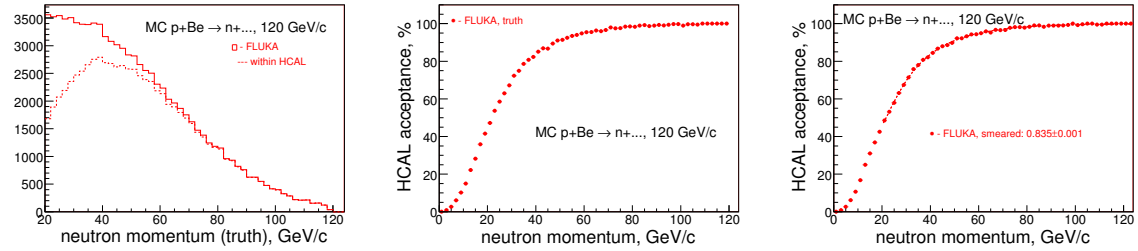

Figure 101: Neutron spectra and calorimeter acceptance as the function of the neutron momentum from p+Be interactions at 120 GeV/c. Left: Neutron spectra with and without HCAL fiducial requirements. HCAL acceptance without (left) and with (right) Fluka neutron smearing applied.

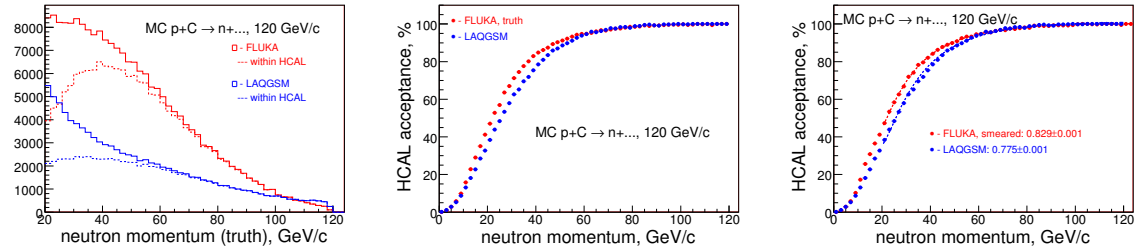

Figure 102: Neutron spectra and calorimeter acceptance as the function of the neutron momentum from p+C interactions at 120 GeV/c. Left: Neutron spectra with and without HCAL fiducial requirements. HCAL acceptance without (left) and with (right) Fluka neutron smearing applied.

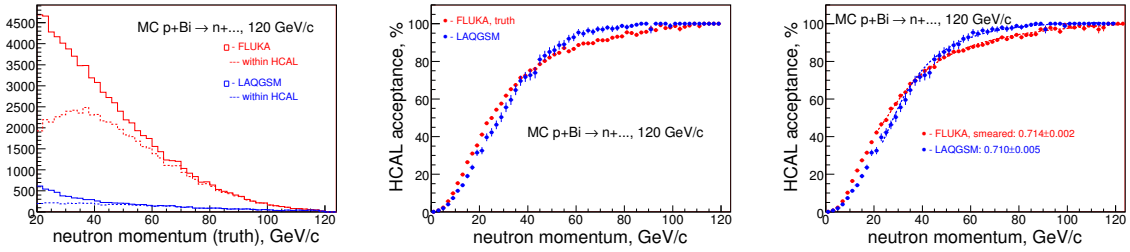

Figure 103: Neutron spectra and calorimeter acceptance as the function of the neutron momentum from p+Bi interactions at 120 GeV/c. Left: Neutron spectra with and without HCAL fiducial requirements. HCAL acceptance without (left) and with (right) Fluka neutron smearing applied.

p_{beam}	ϵ_{hcal}(FLUKA)	ϵ_{hcal}(LAQGSM)
H_2-20 GeV/c	0.166±0.001	-
H_2-58 GeV/c	0.523±0.001	0.627±0.001
Be-58 GeV/c	0.492±0.004	-
C-58 GeV/c	0.478±0.001	0.528±0.002
Bi-58 GeV/c	0.348±0.002	0.451±0.005
U-58 GeV/c	0.349±0.002	-
H_2-84 GeV/c	0.680±0.001	-
Be-120 GeV/c	0.835±0.001	-
C-120 GeV/c	0.829±0.001	0.775±0.001
Bi-120 GeV/c	0.714±0.001	0.710±0.001

Table 29: Average HCAL acceptances based on FLUKA and LAQGSM generators.

16 Effect of Calorimeter Resolution to Neutron Spectrum

The calorimeter resolution, σ, as a function of the incident proton beam momenta was found to be [1]:

$$\sigma = \sqrt{0.554^2 E + 0.026^2 E^2}$$

where E is proton beam energy in GeV. One can assume that the calorimeter performance for neutrons would be pretty match similar to protons. We see also a small nonlinearity there, which can be taken in account by using a second order polynomial function:

$$\sigma = \sqrt{1.98^2 + 0.2948^2 E_{ts} + 0.0558^2 E_{ts}^2}$$

In this formula E_{ts} represents the true summed neutron momentum pointing to HCAL fiducial. An actual smearing value for given event has been derived as a random number from Gaussian distribution, where σ used as an input parameter to Gauss. Thus, for each MC event we have two neutron energies: E_{ts} and $E_{ts} \pm \Delta_E$. Figure 104 illustrates the calorimeter resolution vs the proton beam energy and what used to smear neutron energy in MC.

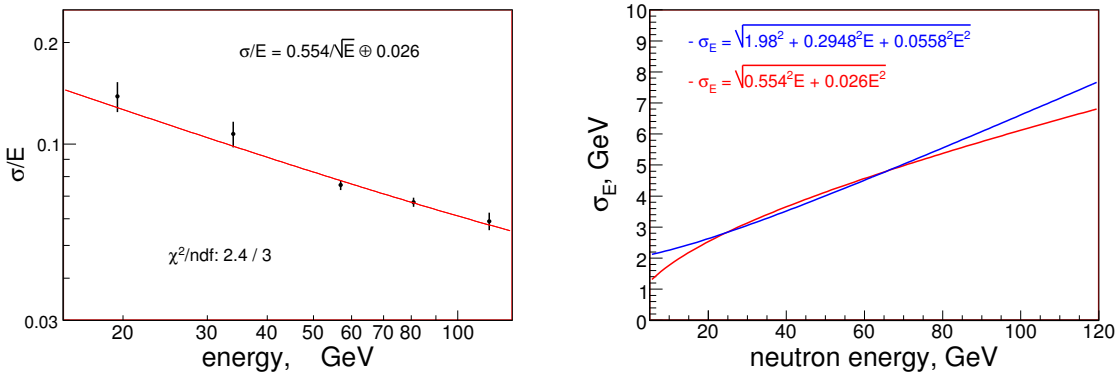

Figure 104: The hadron calorimeter energy resolution, σ/E, vs the incident proton energy (left) and how neutron energy resolution was simulated in MC (right - blue curve).

Figure 105 illustrates the effect of calorimeter resolution to the neutron spectrum using p+p interactions at 20 GeV/c.

Figure 106 illustrates the effect of calorimeter resolution to the neutron spectrum using p+p interactions at 58 GeV/c.

Figure 107 illustrates the effect of calorimeter resolution to the neutron spectrum using p+Be interactions at 58 GeV/c.

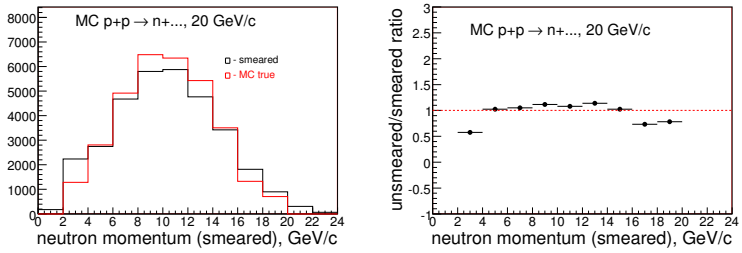

Figure 105: The effect of calorimeter resolution to the neutron spectrum using p+p interactions at 20 GeV/c: smeared and unsmeared summed neutron spectra (left) and the unsmeared over smeared ratio (right).

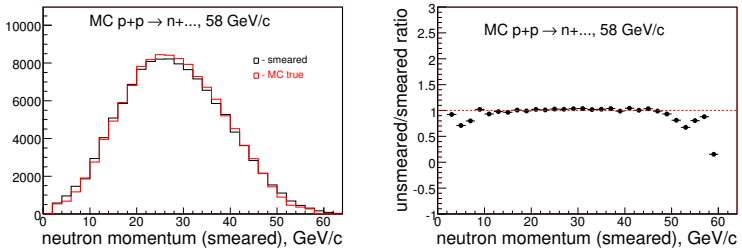

Figure 106: The effect of calorimeter resolution to the neutron spectrum using p+p interactions at 58 GeV/c: smeared and unsmeared summed neutron spectra (left) and the unsmeared over smeared ratio (right).

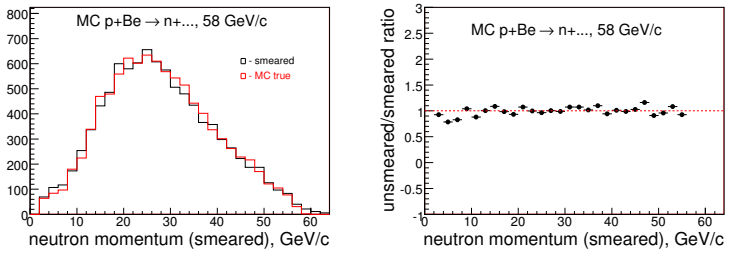

Figure 107: The effect of calorimeter resolution to the neutron spectrum using p+Be interactions at 58 GeV/c: smeared and unsmeared summed neutron spectra (left) and the unsmeared over smeared ratio (right).

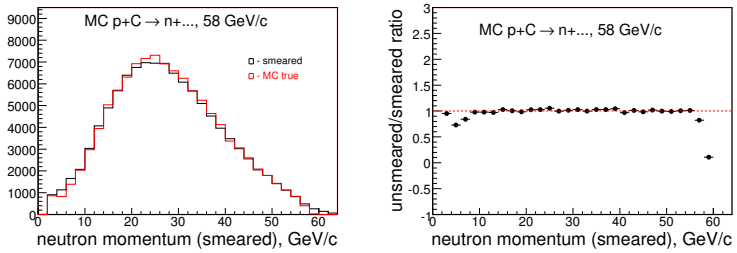

Figure 108: The effect of calorimeter resolution to the neutron spectrum using p+C interactions at 58 GeV/c: smeared and unsmeared summed neutron spectra (left) and the unsmeared over smeared ratio (right).

Figure 108 illustrates the effect of calorimeter resolution to the neutron spectrum using p+C interactions at 58 GeV/c.

Figure 109 illustrates the effect of calorimeter resolution to the neutron spectrum using p+Bi interactions at 58 GeV/c.

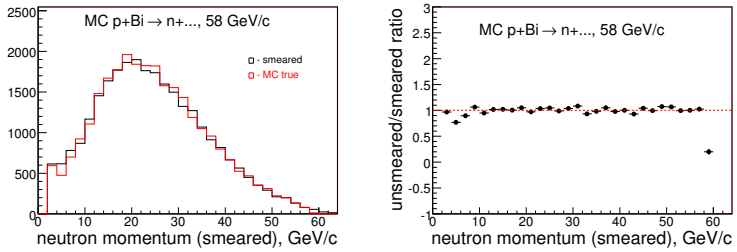

Figure 109: The effect of calorimeter resolution to the neutron spectrum using p+Bi interactions at 58 GeV/c: smeared and unsmeared summed neutron spectra (left) and the unsmeared over smeared ratio (right).

Figure 110 illustrates the effect of calorimeter resolution to the neutron spectrum using p+U interactions at 58 GeV/c.

Figure 111 illustrates the effect of calorimeter resolution to the neutron spectrum using p+p interactions at 84 GeV/c.

Figure 112 illustrates the effect of calorimeter resolution to the neutron spectrum using p+Be interactions at 120 GeV/c.

Figure 113 illustrates the effect of calorimeter resolution to the neutron spectrum using p+C interactions at 120 GeV/c.

Figure 114 illustrates the effect of calorimeter resolution to the neutron spectrum using p+Bi interactions at 120 GeV/c.

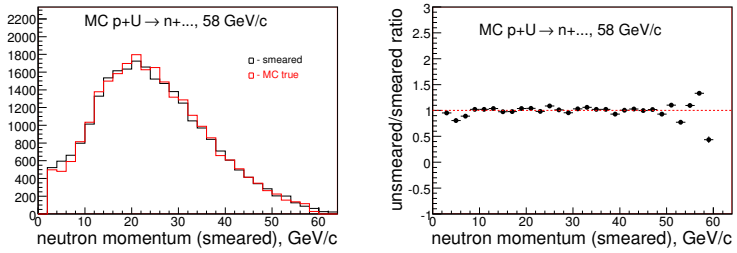

Figure 110: The effect of calorimeter resolution to the neutron spectrum using p+U interactions at 58 GeV/c: smeared and unsmeared summed neutron spectra (left) and the unsmeared over smeared ratio (right).

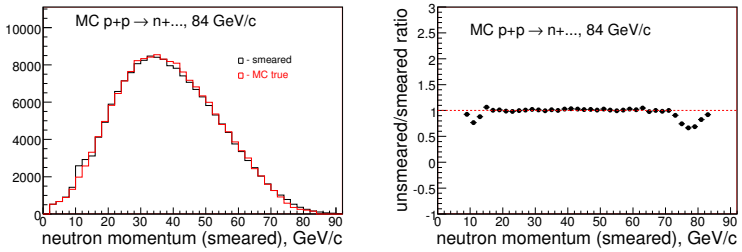

Figure 111: The effect of calorimeter resolution to the neutron spectrum using p+p interactions at 84 GeV/c: smeared and unsmeared summed neutron spectra (left) and the unsmeared over smeared ratio (right).

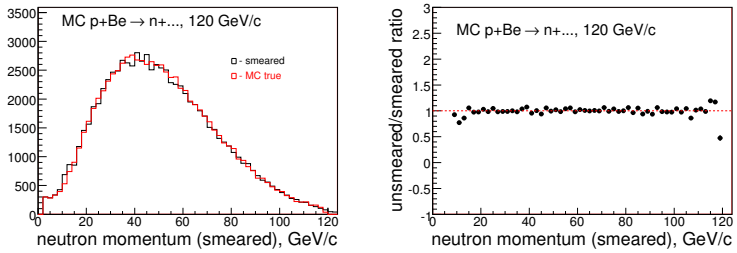

Figure 112: The effect of calorimeter resolution to the neutron spectrum using p+Be interactions at 120 GeV/c: smeared and unsmeared summed neutron spectra (left) and the unsmeared over smeared ratio (right).

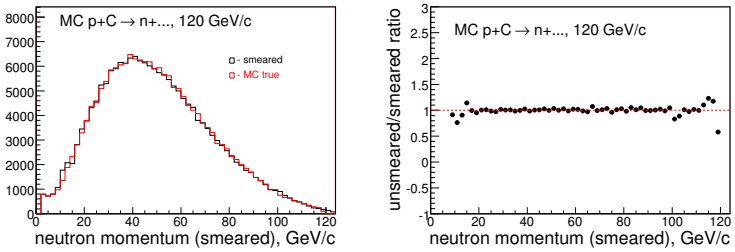

Figure 113: The effect of calorimeter resolution to the neutron spectrum using p+C interactions at 120 GeV/c: smeared and unsmeared summed neutron spectra (left) and the unsmeared over smeared ratio (right).

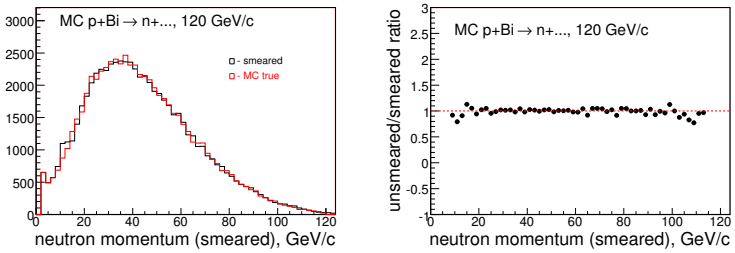

Figure 114: The effect of calorimeter resolution to the neutron spectrum using p+Bi interactions at 120 GeV/c: smeared and unsmeared summed neutron spectra (left) and the unsmeared over smeared ratio (right).

17 Neutron Selection Efficiency

On previous subsection we discussed the HCAL acceptance using Fluka and LAQGSM neutron generators. However, in analysis of the real data we applied the Z_{vtx} and Δp_T and other cuts to select neutrons. Below we will present the neutron reconstruction efficiency.

Figure 115 shows the neutron reconstruction efficiency as the function of the neutron momentum for p+p interactions at 20, 58 and 84 GeV/c.

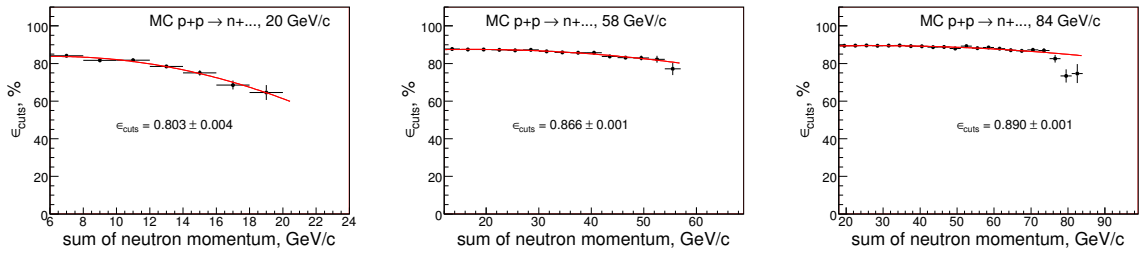

Figure 115: The neutron reconstruction efficiency as the function of the summed neutron momentum for p+p interactions at 20 GeV/c (left), 58 GeV/c (middle) and 84 GeV/c (right), respectively.

Figure 116 shows the neutron reconstruction efficiency as the function of the neutron momentum for p+Be and p+C interactions at 58 GeV/c

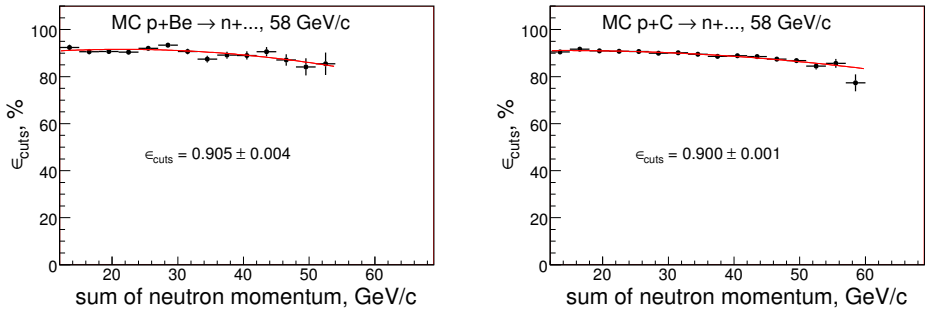

Figure 116: The neutron reconstruction efficiency as the function of the summed neutron momentum for p+Be (left) and p+C (right) interactions at 58 GeV/c.

Figure 117 shows the neutron reconstruction efficiency as the function of the neutron momentum for p+Bi and p+U interactions at 58 GeV/c

Figure 118 shows the neutron reconstruction efficiency as the function of the neutron momentum for p+Be, p+C and p+Bi interactions at 120 GeV/c

Monte Carlo the neutron reconstruction efficiency for the various targets and beam momenta are summarized in Table 30.

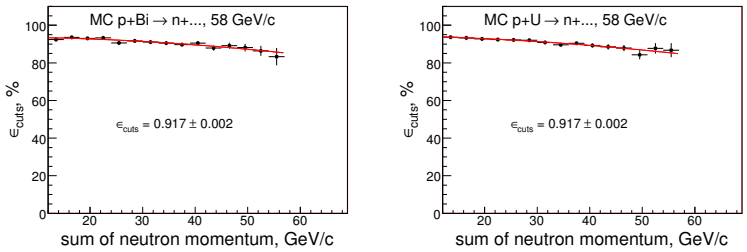

Figure 117: The neutron reconstruction efficiency as the function of the summed neutron momentum for p+Bi (left) and p+U (right) interactions at 58 GeV/c.

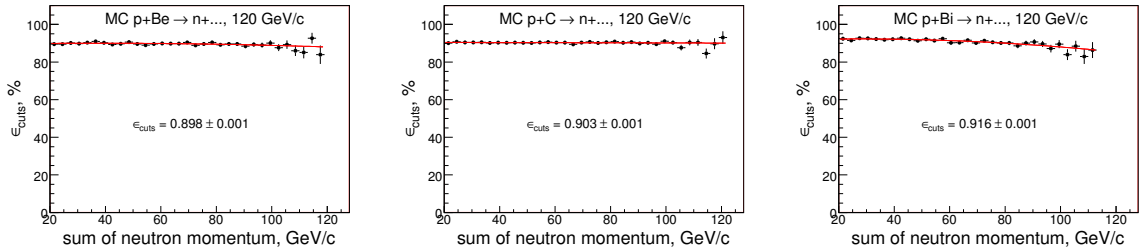

Figure 118: The neutron reconstruction efficiency as the function of the summed neutron momentum for p+Be (left), p+C (middle) and p+Bi (right) interactions at 120 GeV/c

p_{beam}	ϵ_{cuts}
H_2-20 GeV/c	0.801±0.004
H_2-58 GeV/c	0.866±0.001
Be-58 GeV/c	0.905±0.004
C-58 GeV/c	0.900±0.001
Bi-58 GeV/c	0.917±0.002
U-58 GeV/c	0.917±0.002
H_2-84 GeV/c	0.890±0.001
Be-120 GeV/c	0.898±0.001
C-120 GeV/c	0.903±0.001
Bi-120 GeV/c	0.916±0.001

Table 30: Monte Carlo the neutron selection efficiency for the various targets and beam momenta. The efficiencies were calculated with FLUKA.

18 Neutron Backgrounds

The studies of the events when the total momentum of all tracks significantly exceed p_{beam} indicates the presence of a failure in the track reconstruction. We found that this effect take place in data as well in Monte Carlo within compatible rate. Some K_L^o from the primary target, the neutrons produced by the charged tracks downstream of target and photons might also contribute to the neutron spectrum. The neutron backgrounds are listed below:

- fakes due to unreconstructed tracks
- fakes due to misreconstructed tracks
- combinatoric backgrounds
- contributions from K_L^o
- neutrons from downstream of target
- photons (left over after passing EMCal)

18.1 Tracking source of backgrounds

Monte Carlo track momentum true-reco difference vs the reconstructed momentum distribution illustrated in Figure 119 using p+C interactions at 120 GeV/c.

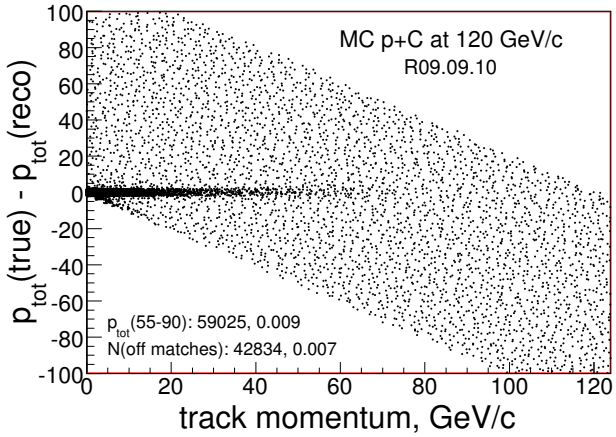

Figure 119: The true - reco vs the reco momentum distribution from p+C interactions at 120 GeV/c. Tracks are from the primary vertex. Match inefficiency (when $|\Delta p|$ >5 GeV/c) is about 0.7% (was 5%). Upper edge line of the distribution illustrates $p_{tot}(reco)$=0 case. Bottom edge - $p_{tot}(true)$=0

All data points away from $\Delta p = 0$ line in Fig. 119 illustrates the presence of the failure in track reconstruction. They all might contribute to the fake neutrons.

18.2 Total backgrounds

Below we describe the total background calculation procedure.

- apply the selection cuts as in data where it possible
- calculate neutron momentum in MC same way as in data: $E_n = E_{hcal}$-E_{trk}(hcal)(if)
- use MC sample where neutron was NOT generated
- what will be selected are fake neutrons
- calculate fake rate per single MC event
  - denominator: events passed Z_{vtx}, Δp_T and trigger requirements
  - numerator: same as above and is sufficient energy in HCAL?

Usage of HCAL responses for the sample without neutrons will allow to estimate an integral of all backgrounds: contribution from track failure as well as K^o_L, neutrons from downstream of target and photons.

Assumptions:

- tracking detectors' simulation, track and vertex reconstruction software in MC are compatible with data
- contributions from n_s, K_L, γ are about the same as in data
- HCAL simulation is more less reasonable (at least central value)

18.3 Fake neutron rates

Figure 120 illustrates the neutron fake rates and predicted contribution to the neutron sample in data for p+p interactions at 20 GeV/c.

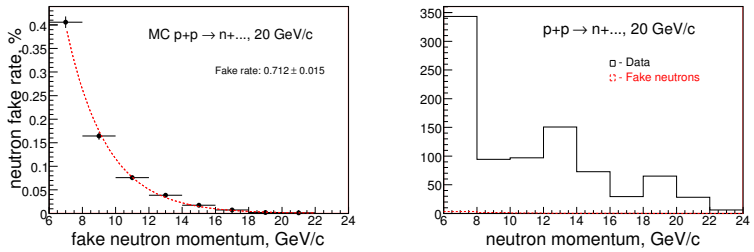

Figure 120: The neutron fake rates (left) and predicted contribution to the neutron sample in data for p+p interactions at 20 GeV/c..

Figure 121 illustrates the neutron fake rates and predicted contribution to the neutron sample in data for p+p interactions at 58 GeV/c.

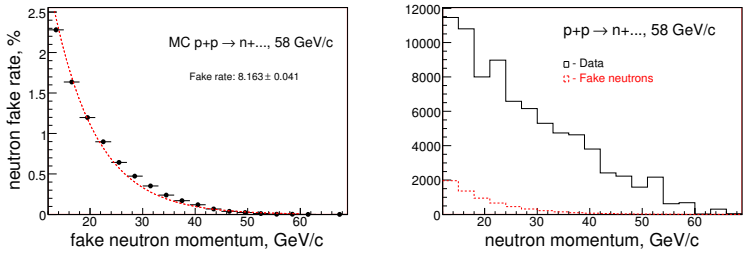

Figure 121: The neutron fake rates (left) and predicted contribution to the neutron sample in data (right) for p+p interactions at 58 GeV/c.

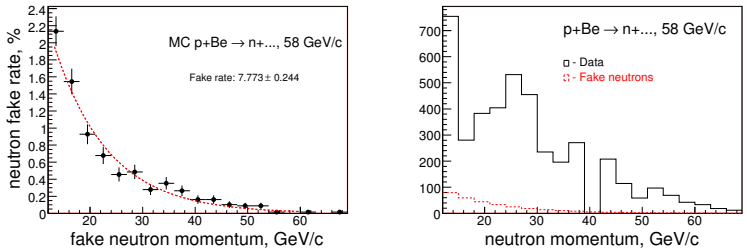

Figure 122: The neutron fake rates (left) and predicted contribution to the neutron sample in data (right) for p+Be interactions at 58 GeV/c.

Figure 122 illustrates the neutron fake rates and predicted contribution to the neutron sample in data for p+Be interactions at 58 GeV/c.

Figure 123 illustrates the neutron fake rates and predicted contribution to the neutron sample in data for p+C interactions at 58 GeV/c.

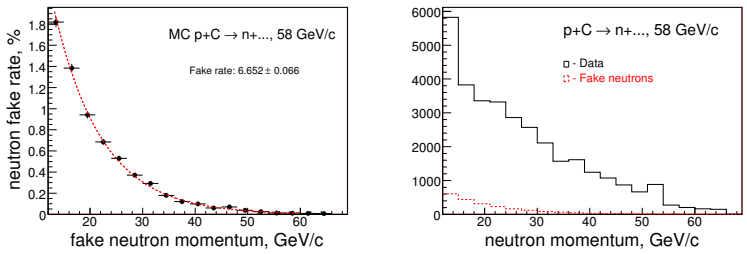

Figure 123: The neutron fake rates (left) and predicted contribution to the neutron sample in data (right) for p+C interactions at 58 GeV/c.

Figure 124 illustrates the neutron fake rates and predicted contribution to the neutron sample in data for p+Bi interactions at 58 GeV/c.

Figure 125 illustrates the neutron fake rates and predicted contribution to the neutron sample in data for p+U interactions at 58 GeV/c.

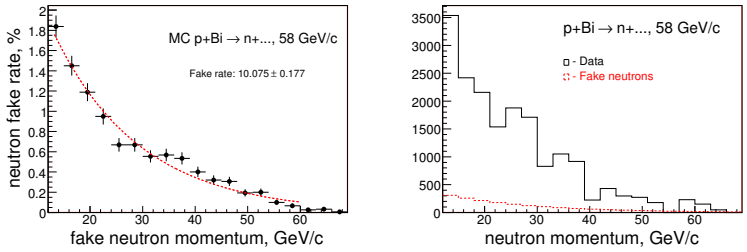

Figure 124: The neutron fake rates (left) and predicted contribution to the neutron sample in data (right) for p+Bi interactions at 58 GeV/c.

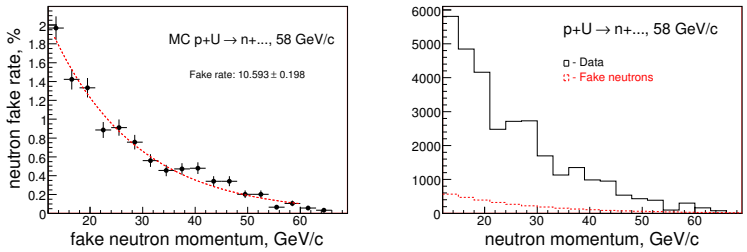

Figure 125: The neutron fake rates (left) and predicted contribution to the neutron sample in data (right) for p+U interactions at 58 GeV/c.

Figure 126 illustrates the neutron fake rates and predicted contribution to the neutron sample in data for p+p interactions at 84 GeV/c.

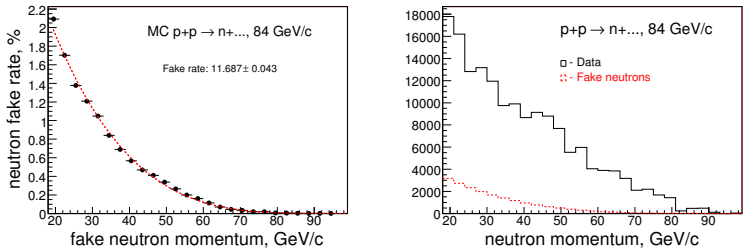

Figure 126: The neutron fake rates (left) and predicted contribution to the neutron sample in data (right) for p+p interactions at 84 GeV/c.

Figure 127 illustrates the neutron fake rates and predicted contribution to the neutron sample in data for p+Be interactions at 120 GeV/c.

Figure 128 illustrates the neutron fake rates and predicted contribution to the neutron sample in data for p+C interactions at 120 GeV/c.

Figure 129 illustrates the neutron fake rates and predicted contribution to the neutron sample in data for p+Bi interactions at 120 GeV/c.

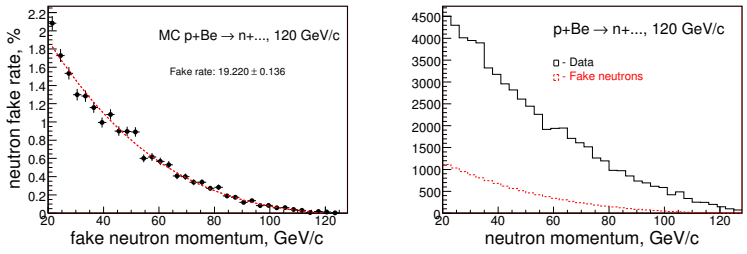

Figure 127: The neutron fake rates (left) and predicted contribution to the neutron sample in data (right) for p+Be interactions at 120 GeV/c.

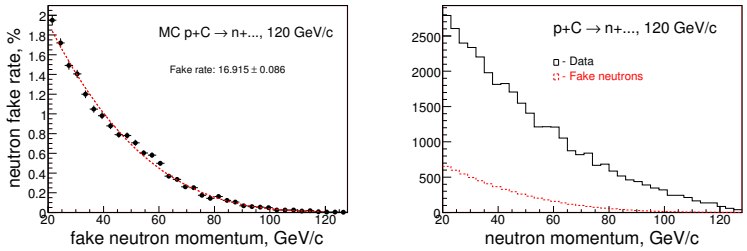

Figure 128: The neutron fake rates (left) and predicted contribution to the neutron sample in data (right) for p+C interactions at 120 GeV/c.

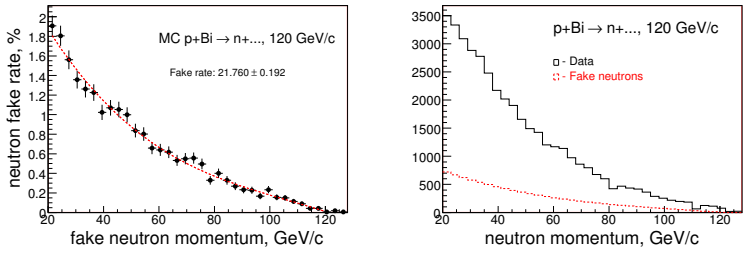

Figure 129: The neutron fake rates (left) and predicted contribution to the neutron sample in data (right) for p+Bi interactions at 120 GeV/c.

Monte Carlo neutron fake rate studies for the various targets and beam momenta are summarized in Table 31.

p_{beam}	Fake rate,%	non-matches,%	$< N_{trk} >$	$< P_{trk} >$	$< F_{(n_s+K_L+\gamma)} >$
H_2-20	0.71±0.02	0.48	0.30±0.03	7.2±0.4	0.25
H_2-58	8.16±0.04	1.41	0.73±0.01	11.8±0.1	0.33
Be-58	7.77±0.24	1.66	0.63±0.03	12.4±0.4	0.38
C-58	6.65±0.07	1.76	0.68±0.02	12.0±0.2	0.31
Bi-58	10.08±0.18	1.21	0.65±0.02	11.7±0.2	0.45
U-58	10.59±0.20	1.37	0.66±0.01	11.8±0.1	0.53
H_2-84	11.69±0.04	1.79	1.15±0.01	12.4±0.1	0.33
Be-120	19.22±0.14	2.50	1.51±0.01	16.36±0.04	0.39
C-120	16.92±0.09	2.68	1.50±0.01	16.36±0.05	0.34
Bi-120	21.76±0.19	2.21	1.53±0.01	15.85±0.04	0.46

Table 31: Summary of Monte Carlo neutron fake rate studies. "Non matches" represents the fraction of tracks when reconstructed one is off (at least 5 GeV/c for 20 GeV/c beam momentum) from a true value. $< N_{trk} >$ and $< P_{trk} >$ are data based the mean value of charged track multiplicities and the mean value of track momentum pointing to front wall of RICH within ±40 cm rectangular with center at the beam line. $< F_{(n_s+K_L+\gamma)} >$ is MC predicted fraction of the neutrals in the neutron fake rate.

18.4 Backgrounds due to of the neutrals

Figure 130 illustrates the fractions of the neutrals to respect of the total background based on the GEANT simulated depositions into HCAL. Calculations made for p+p interactions at 20, 58 and 84 GeV/c.

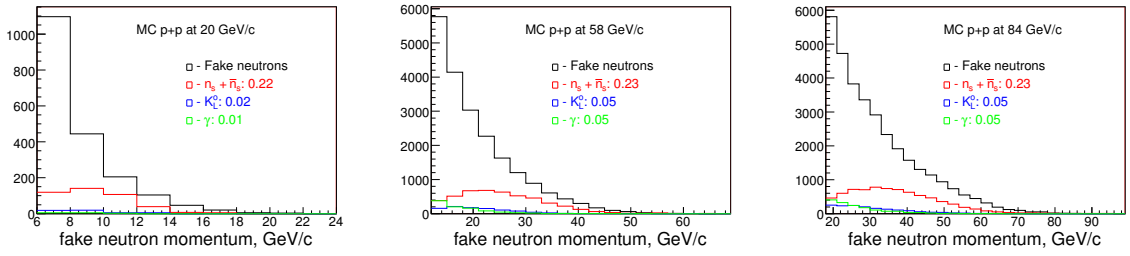

Figure 130: The fractions of the neutrals to respect of the total background based on the GEANT simulated depositions into HCAL. Calculations made for p+p interactions at 20 (left), 58 (middle) and at 84 GeV/c.

Figure 131 illustrates the fractions of the neutrals to respect of the total background based on the GEANT simulated depositions into HCAL. Calculations made

for p+Be and p+C interactions at 58 GeV/c.

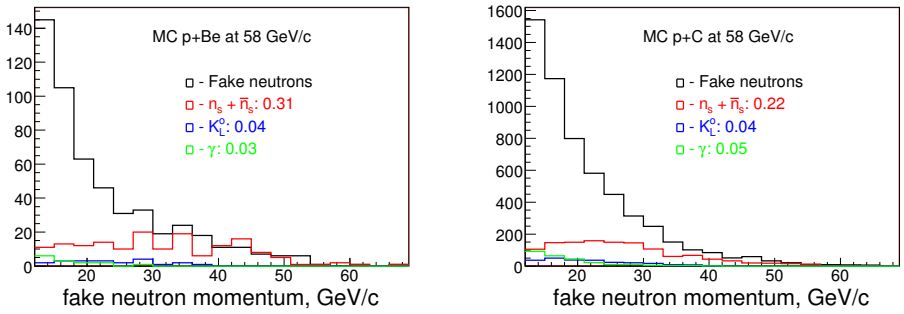

Figure 131: The fractions of the neutrals to respect of the total background based on the GEANT simulated depositions into HCAL. Calculations made for p+Be (left) and p+C (right) interactions at 58 GeV/c.

Figure 132 illustrates the fractions of the neutrals to respect of the total background based on the GEANT simulated depositions into HCAL. Calculations made for p+Bi and p+U interactions at 58 GeV/c.

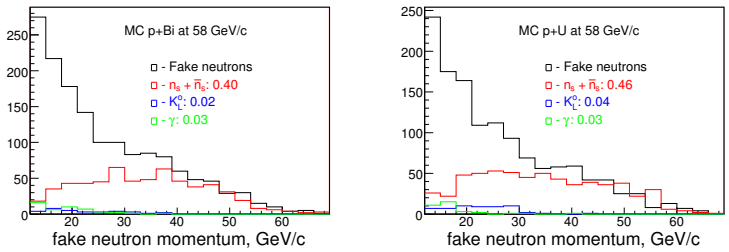

Figure 132: The fractions of the neutrals to respect of the total background based on the GEANT simulated depositions into HCAL. Calculations made for p+Bi (left) and p+U (right) interactions at 58 GeV/c.

Figure 133 illustrates the fractions of the neutrals to respect of the total background which calculated through the GEANT simulated depositions into HCAL. Calculations made for proton interactions with thin target at 120 GeV/c beam momentum.

The predicted fractions of the neutrals at the total background calculated using the GEANT simulated depositions into HCAL in Monte Carlo events where the neutrons were NOT generated are summarized in Table 32.

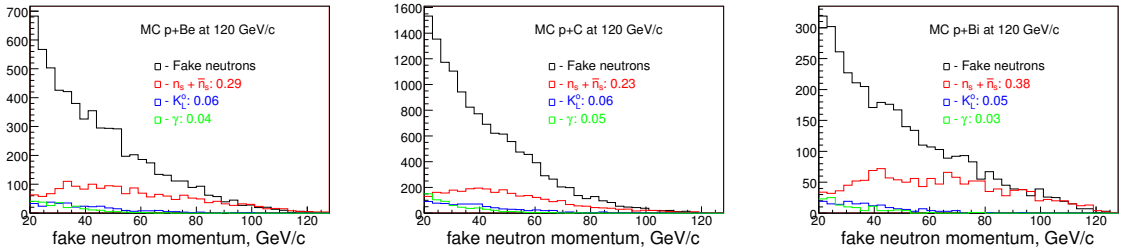

Figure 133: The fractions of the neutrals to respect of the total background which calculated through the GEANT simulated depositions into HCAL. Calculations made for the MC samples at 120 GeV/c beam momentum for targets: Be (on left), C (on middle) and Bi (on right).

p_{beam}	F(n_s)	F(K^o_L)	F(γ)	F(neutrals-total)
H_2-20 GeV/c	0.22	0.02	0.01	0.25
H_2-58 GeV/c	0.23	0.05	0.05	0.33
Be-58 GeV/c	0.31	0.04	0.03	0.38
C-58 GeV/c	0.22	0.04	0.05	0.31
Bi-58 GeV/c	0.40	0.02	0.03	0.45
U-58 GeV/c	0.46	0.04	0.03	0.53
H_2-84 GeV/c	0.23	0.05	0.05	0.33
Be-120 GeV/c	0.29	0.06	0.04	0.39
C-120 GeV/c	0.23	0.06	0.05	0.34
Bi-120 GeV/c	0.38	0.05	0.03	0.46

Table 32: The predicted fractions of the neutrals at the total background which is the GEANT simulated depositions into HCAL. The fractions estimated using Monte Carlo events where the neutrons were NOT generated. F(n_s) - secondary neutrons, F(K^o_L) - contribution from K^o_L and F(γ) - remained gamma's energy after passing EMCAL.

19 Final Neutron Sample Sizes and Spectra

Corrections applied to the neutron sample sizes are summarized in Table 33.

	N_n(data)	-Backgr	$\times\frac{1}{\epsilon(trig)}$	$\times\frac{1}{\epsilon(hcal)}$	$\times\frac{1}{\epsilon(n-sel)}$	Final
H_2-20	886±48	$_{-0.007}$880	$\frac{1}{0.46}$2160	$\frac{1}{0.17}$18607	$\frac{1}{0.80}$23649	23649±1292
H_2-58	80578±1154	$_{-0.08}$74121	$\frac{1}{0.71}$109633	$\frac{1}{0.52}$219883	$\frac{1}{0.87}$254575	254575±3646
Be-58	4164±247	$_{-0.08}$3856	$\frac{1}{0.82}$5025	$\frac{1}{0.49}$10344	$\frac{1}{0.91}$11475	11475±681
C-58	32589±773	$_{-0.07}$30427	$\frac{1}{0.84}$37418	$\frac{1}{0.48}$83785	$\frac{1}{0.90}$92874	92874±2204
Bi-58	17861±405	$_{-0.10}$16099	$\frac{1}{0.845}$19542	$\frac{1}{0.35}$61120	$\frac{1}{0.92}$66279	66279±1503
U-58	30864±421	$_{-0.11}$27640	$\frac{1}{0.845}$33114	$\frac{1}{0.35}$104385	$\frac{1}{0.92}$113005	113005±1541
H_2-84	161097±1517	$_{-0.12}$143496	$\frac{1}{0.73}$201994	$\frac{1}{0.68}$278596	$\frac{1}{0.89}$314452	314452±2962
Be-120	61047±199	$_{-0.19}$49436	$\frac{1}{0.885}$57567	$\frac{1}{0.84}$71233	$\frac{1}{0.90}$79377	79377±258
C-120	35568±165	$_{-0.17}$29575	$\frac{1}{0.905}$33621	$\frac{1}{0.83}$41991	$\frac{1}{0.90}$46493	46493±216
Bi-120	39825±146	$_{-0.22}$31254	$\frac{1}{0.87}$36463	$\frac{1}{0.71}$53492	$\frac{1}{0.92}$58341	58341±214

Table 33: Summary of corrections to the neutron sample size. Uncertainties are statistical

Figure 134 shows the detected and finalized neutron spectra for p+p interactions at 20, 58 and 84 GeV/c.

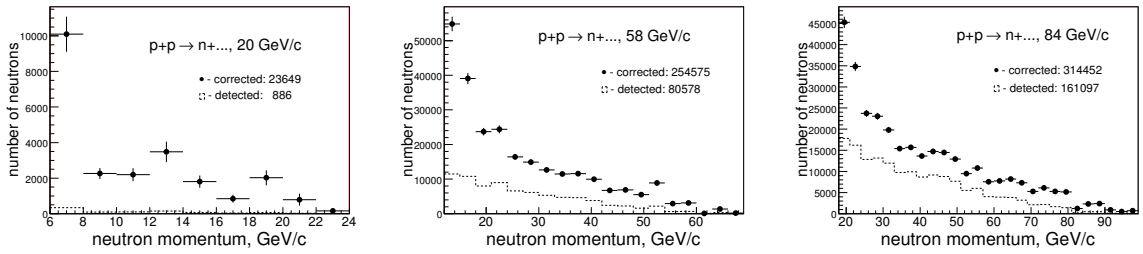

Figure 134: The detected and finalized neutron spectra for p+p interactions at 20 GeV/c (left), 58 GeV/c (middle) 84 GeV/c (right), respectively. The final spectrum include the background subtraction and corrections for trigger efficiency, HCAL acceptance and neutron selection efficiency.

Figure 135 shows the detected and finalized neutron spectra for p+Be and p+C interactions at 58 GeV/c.

Figure 136 shows the detected and finalized neutron spectra for p+Bi and p+U interactions at 58 GeV/c.

Figure 137 shows the detected and finalized neutron spectra for p+Be, p+C and p+Bi interactions at 120 GeV/c.

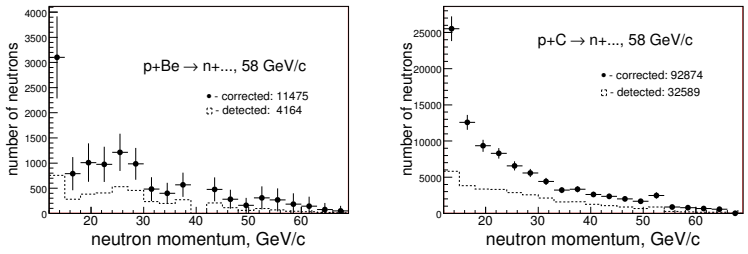

Figure 135: The detected and finalized neutron spectra for p+Be (left) and p+C (right) interactions at 58 GeV/c. The final spectrum include the background subtraction and corrections for trigger efficiency, HCAL acceptance and neutron selection efficiency.

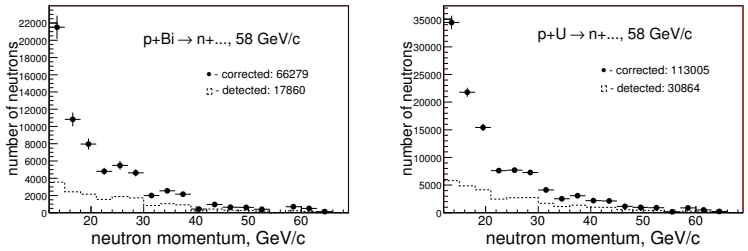

Figure 136: The detected and finalized neutron spectra for p+Bi (left) and p+U (right) interactions at 58 GeV/c. The final spectrum includes the background subtraction and corrections for trigger efficiency, HCAL acceptance and neutron selection efficiency.

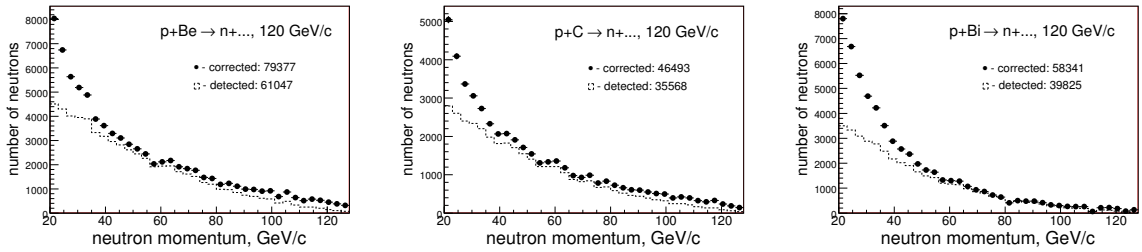

Figure 137: The detected and finalized neutron spectra for p+Be (left), p+C (middle) and p+Bi (right) interactions at 120 GeV/c. The final spectrum include the background subtraction and corrections for trigger efficiency, HCAL acceptance and neutron selection efficiency.

20 Systematic Uncertainty

The statistical, estimated and assigned systematic uncertainties for the incident protons are summarized in Table 34.

target	p_{beam}	stat.	estim.sys.	assigned syst.
H_2	20	0.054	±0.07	±0.10
H_2	58	0.026	±0.03	±0.10
Beryllium	58	0.052	±0.01	±0.10
Carbon	58	0.028	±0.02	±0.10
Bismuth	58	0.018	±0.05	±0.10
Uranium	58	0.015	±0.06	±0.10
H_2	84	0.009	±0.09	±0.10
Beryllium	120	0.009	±0.08	±0.10
Carbon	120	0.012	±0.07	±0.10
Bismuth	120	0.009	±0.08	±0.10

Table 34: The statistical, estimated and assigned systematic uncertainties for the incident protons. The systematic uncertainties for the target-out sample size considered separately.

The systematic uncertainty studies of the target-out subtraction procedure are summarized in Table 35.

The systematic uncertainty studies of the trigger efficiency are calculated according to formula:

$$N_n(p_n > p_{min}) = \frac{n_n(t-in)-n_n(t-out)-n_n(backgr)}{\epsilon_{trig}\times\epsilon_{hcal}\times\epsilon_{cuts}} \pm[0.10 \times \Delta N_{trig}]$$

and summarized in Table 36.

The HCAL acceptance uncertainty was estimated by two approaches: a)using a difference between FLUKA and LAQGSM predictions and b)by assigning the some uncertainty.

The systematic uncertainty studies of the HCAL acceptance using the differences between FLUKA and LAQGSM predictions are summarized in Table 37.

The systematic uncertainty studies of the HCAL acceptance uncertainty using the second approach are summarized in Table 38.

Figure 138 shows the corrected neutron spectra from p+p interactions at 20, 58 and 84 GeV/c with HCAL systematic uncertainties superimposed.

Figure 139 shows the corrected neutron spectra from p+Be and p+C interactions at 58 GeV/c with HCAL systematic uncertainties superimposed.

Figure 140 shows the corrected neutron spectra from p+Bi and p+U interactions at 58 GeV/c with HCAL systematic uncertainties superimposed.

Figure 141 shows the corrected neutron spectra from p+Be, p+C and p+Bi interactions at 120 GeV/c with HCAL systematic uncertainties superimposed.

	N_n(nominal)	F_{t-out}	ΔF_{t-out}	N_n variations	$\Delta\epsilon_{t-out}$
H_2-20	23649	0.50	±0.17	$^{+24843}_{-22455}$	±0.050
H_2-58	254575	1.16	±0.10	$^{+267455}_{-241723}$	±0.051
Be-58	11475	1.47	±0.16	$^{+12755}_{-10235}$	±0.112
C-58	92874	1.39	±0.13	$^{+96823}_{-88943}$	±0.043
Bi-58	66279	1.14	±0.10	$^{+72338}_{-60280}$	±0.091
U-58	113005	1.09	±0.10	$^{+124045}_{-102043}$	±0.098
H_2-84	314452	1.11	±0.10	$^{+328634}_{-300271}$	±0.045
Be-120	79377	1.09	±0.10	$^{+84762}_{-73992}$	±0.068
C-120	46493	1.25	±0.10	$^{+48182}_{-44804}$	±0.036
Bi-120	58341	1.04	±0.10	$^{+64653}_{-52029}$	±0.108

Table 35: The systematic uncertainty studies of the target-out subtraction procedure. Second column represents the correction to the target-out sample size applied. Third column represents an assigned uncertainty in correction factor. Forth column represents corresponding variations on the number of neutrons. Last column - the systematic uncertainty.

	N_n(nominal)	$\Delta\epsilon_{trig}$(ass)	N_n(var)	$\Delta\epsilon_{trig}$
H_2-20	23649	±0.10	$^{+24900}_{-22399}$	±0.053
H_2-58	254575	±0.10	$^{+261620}_{-247531}$	±0.028
Be-58	11475	±0.10	$^{+11672}_{-11278}$	±0.017
C-58	92874	±0.10	$^{+94097}_{-91651}$	±0.013
Bi-58	66279	±0.10	$^{+67176}_{-65382}$	±0.014
U-58	113005	±0.10	$^{+114483}_{-111526}$	±0.013
H_2-84	314452	±0.10	$^{+322871}_{-306034}$	±0.027
Be-120	79377	±0.07	$^{+80086}_{-78668}$	±0.009
C-120	46493	±0.05	$^{+46742}_{-46244}$	±0.005
Bi-120	58341	±0.10	$^{+59129}_{-57553}$	±0.014

Table 36: The systematic uncertainty studies of the trigger efficiency. The $\Delta\epsilon_{trig}$(ass) is an assigned uncertainty applied to the correction value. N_n represents the neutron sample size variations. Last column - the final uncertainty.

	N_n(FLUKA)	N_n(LAQGSM)	$\Delta\epsilon_{hcal}$	cf_1
H_2-20	23649	n/a	n/a	10
H_2-58	254575	241506	$\pm$0.051	4.14
Be-58	11475	12096	$\pm$0.054	3.95
C-58	92874	95362	$\pm$0.027	4.25
Bi-58	66279	61602	$\pm$0.076	5.61
U-58	113005	105435	$\pm$0.072	5.52
H_2-84	314452	n/a	n/a	2.5
Be-120	79377	86496	$\pm$0.090	2.02
C-120	46493	50599	$\pm$0.088	2.04
Bi-120	58341	62501	$\pm$0.071	2.30

Table 37: The systematic uncertainty studies of the HCAL acceptance using the differences between FLUKA and LAQGSM predictions. Middle column - the systematic uncertainty. Last column - the correction factor for the lowest momentum bin (FLUKA).

	N_n(nominal)	N_n variations	$\Delta\epsilon_{hcal}$
H_2-20	23649	$^{+29875}_{-17424}$	$\pm$0.263
H_2-58	254575	$^{+292606}_{-216545}$	$\pm$0.149
Be-58	11475	$^{+13229}_{-9721}$	$\pm$0.153
C-58	92874	$^{+108201}_{-77547}$	$\pm$0.165
Bi-58	66279	$^{+79746}_{-52812}$	$\pm$0.203
U-58	113005	$^{+136044}_{-89965}$	$\pm$0.204
H_2-84	314452	$^{+340231}_{-288674}$	$\pm$0.082
Be-120	79377	$^{+83936}_{-74818}$	$\pm$0.057
C-120	46493	$^{+49271}_{-43714}$	$\pm$0.060
Bi-120	58341	$^{+63885}_{-52797}$	$\pm$0.095

Table 38: The systematic uncertainty studies of the HCAL acceptance using the second approach. Middle column represents the neutron samples due to $\pm$0.30*(corr-uncorr) variations in the HCAL acceptance correction. Last column - the systematic uncertainty.

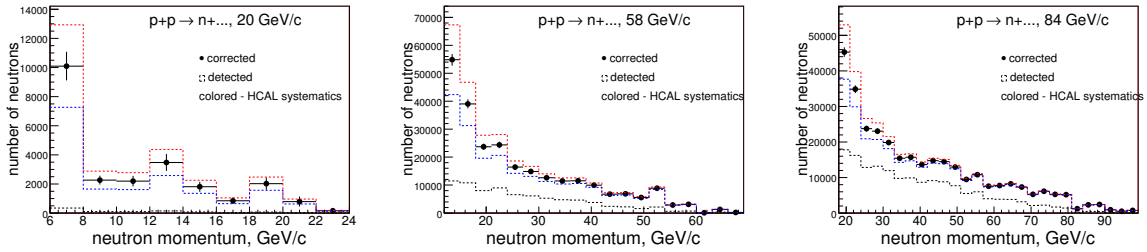

Figure 138: The corrected neutron spectra from p+p interactions at 20, 58 and 84 GeV/c with HCAL systematic uncertainties superimposed.

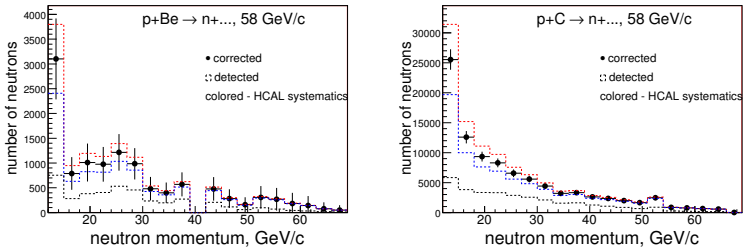

Figure 139: The corrected neutron spectra from p+Be (left) and p+C (right) interactions at 58 GeV/c with HCAL systematic uncertainties superimposed.

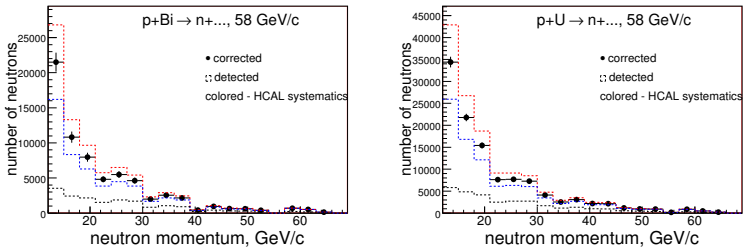

Figure 140: The corrected neutron spectra from p+Bi (left) and p+U (right) interactions at 58 GeV/c with HCAL systematic uncertainties superimposed.

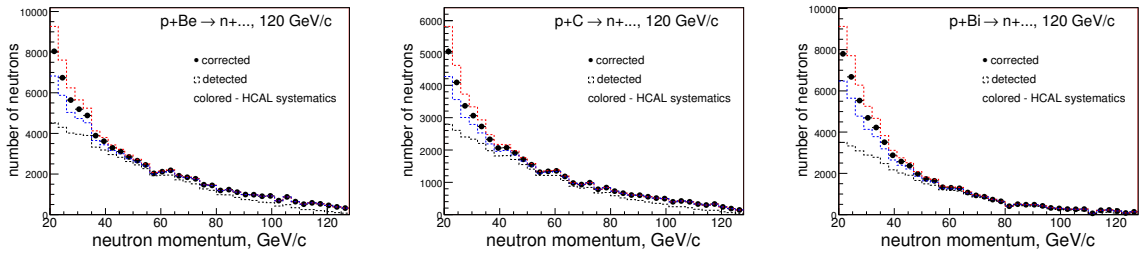

Figure 141: The corrected neutron spectra from p+Be (left), p+C (middle) and p+Bi (right) interactions at 120 GeV/c with HCAL systematic uncertainties superimposed.

The systematic uncertainty studies of the neutron selection efficiency are summarized in Table 39.

	N_n(nominal)	ϵ_{sel}	N_n variations	$\Delta\epsilon_{nsel}$
H_2-58	23649	0.801	$^{+25162}_{-22137}$	$\pm$0.064
H_2-58	254575	0.866	$^{+264983}_{-244168}$	$\pm$0.041
Be-58	11475	0.905	$^{+11814}_{-11135}$	$\pm$0.030
C-58	92874	0.900	$^{+95600}_{-90147}$	$\pm$0.029
Bi-58	66279	0.917	$^{+67827}_{-64731}$	$\pm$0.023
U-58	113005	0.917	$^{+115590}_{-110419}$	$\pm$0.023
H_2-58	314452	0.890	$^{+325209}_{-303696}$	$\pm$0.034
Be-120	79377	0.898	$^{+81820}_{-76933}$	$\pm$0.031
C-120	46493	0.903	$^{+47844}_{-45142}$	$\pm$0.029
Bi-120	58341	0.916	$^{+59796}_{-56886}$	$\pm$0.025

Table 39: The systematic uncertainty studies of the neutron selection efficiency. Second column represents the neutron selection efficiency. Third column represents the N_n numbers for $\pm 0.30 * (corr - uncorr)$ variations in the correction value. Last column - the systematic uncertainty.

The systematic uncertainty studies of the neutron backgrounds are summarized in Table 40.

	N_n(nominal)	$Fake_n$	N_n variations	$\Delta\epsilon_{backgr}$
H_2-20	23649	0.007	$^{+23701}_{-23598}$	$\pm$0.002
H_2-58	254575	0.082	$^{+262434}_{-246716}$	$\pm$0.031
Be-58	11475	0.078	$^{+11780}_{-11170}$	$\pm$0.027
C-58	92874	0.066	$^{+95126}_{-90621}$	$\pm$0.024
Bi-58	66279	0.101	$^{+68419}_{-64139}$	$\pm$0.032
U-58	113005	0.106	$^{+116885}_{-109124}$	$\pm$0.034
H_2-84	314452	0.117	$^{+325923}_{-302982}$	$\pm$0.036
Be-120	79377	0.192	$^{+85024}_{-73730}$	$\pm$0.071
C-120	46493	0.169	$^{+49413}_{-43573}$	$\pm$0.063
Bi-120	58341	0.218	$^{+63045}_{-53637}$	$\pm$0.081

Table 40: The systematic uncertainty studies of the neutron backgrounds. Middle column represents the N_n numbers for ± 0.30 variations in the neutron fake rate. Last column - the systematic uncertainty.

The total systematic uncertainty shown in Table 41.

Figure 142 shows the neutron spectra from p+p interactions at 20, 58 and 84 GeV/c with the total systematic uncertainties superimposed.

Figure 143 shows the neutron spectra for p+Be and p+C interactions at 58 GeV/c with the total systematic uncertainties superimposed.

	Inc	T-out.	Trig.	Accept	Cuts	Backgr	Total
H_2-20	±0.10	±0.050	±0.053	±0.263	±0.064	±0.002	±0.298
H_2-58	±0.10	±0.051	±0.028	±0.149	±0.041	±0.031	±0.196
Be-58	±0.10	±0.112	±0.017	±0.153	±0.030	±0.027	±0.219
C-58	±0.10	±0.043	±0.013	±0.165	±0.029	±0.024	±0.202
Bi-58	±0.10	±0.091	±0.014	±0.203	±0.023	±0.032	±0.247
U-58	±0.10	±0.098	±0.013	±0.204	±0.023	±0.034	±0.251
H_2-84	±0.10	±0.045	±0.027	±0.082	±0.034	±0.037	±0.148
Be-120	±0.10	±0.068	±0.009	±0.057	±0.031	±0.071	±0.155
C-120	±0.10	±0.036	±0.005	±0.060	±0.029	±0.063	±0.140
Bi-120	±0.10	±0.108	±0.014	±0.095	±0.025	±0.081	±0.195

Table 41: The total and partial systematic uncertainties.

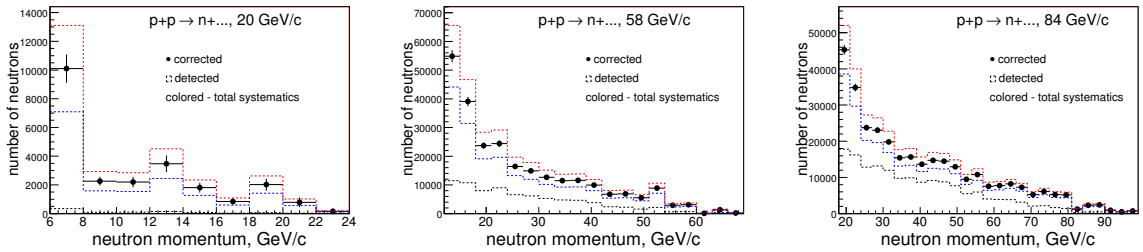

Figure 142: The neutron spectra from p+p interactions at 20 (left), 58 (middle) and 84 GeV/c (right) with the total systematic uncertainties superimposed.

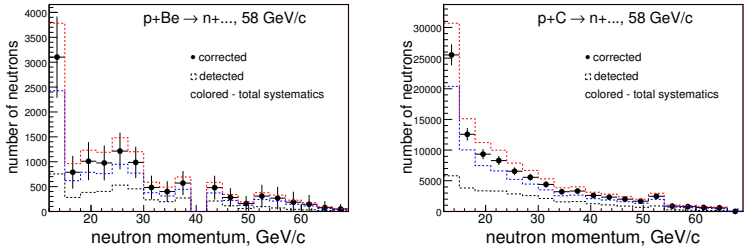

Figure 143: The final neutron spectra for p+Be (left) and p+C (right) interactions at 58 GeV/c with the total systematic uncertainties superimposed.

Figure 144 shows the final neutron spectra for p+Bi and p+U interactions at 58 GeV/c with the total systematic uncertainties superimposed.

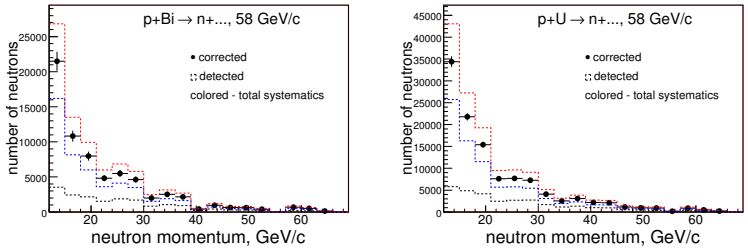

Figure 144: The neutron spectra for p+Bi (left) and p+U (right) interactions at 58 GeV/c with the total systematic uncertainties superimposed.

Figure 145 shows the neutron spectra for p+Be, p+C and p+Bi interactions at 120 GeV/c with the total systematic uncertainties superimposed.

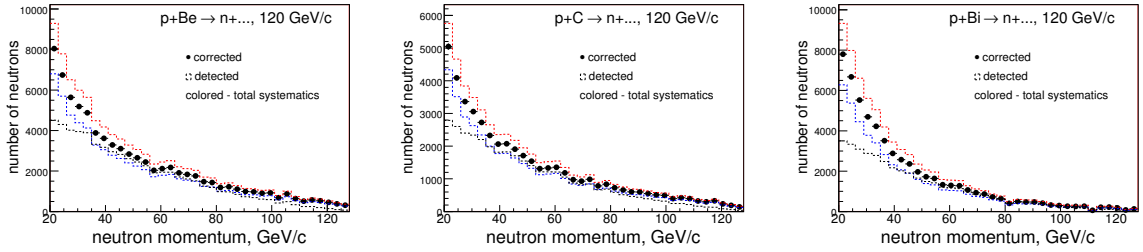

Figure 145: The final neutron spectra for p+Be (left), p+C (middle) and p+Bi (right) interactions at 120 GeV/c with the total systematic uncertainties superimposed.

21 Cross Section Results

We calculate the inclusive neutron production cross sections for following cases:

- spectra were corrected for the neutrons missed due to calorimeter's geometrical acceptance
- spectra NOT corrected for the geometrical acceptance
- invariant cross section with the calorimeter's solid angle included

Before to discuss the neutron cross section we like to do some cross check. For example, estimate the inelastic cross section using our neutron sample and compare it with PDG.

21.1 Inelastic cross section estimate (cross check)

Our neutron sample represents a subsample of the inelastic processes, or σ_{inel}. If we count events prior the neutron selection, then it would be the inelastic sample. We calculate σ_{inel} as:

$$\sigma_{inel} = \frac{N_{inel}(t-in) - N_{inel}(t-out) - N_{backgr}}{N_{beam} \times \epsilon_{trig}} \times \frac{10^4}{n_t}, \text{ mb/(GeV/c)}$$

where N_{inel} are events passed Z_{vtx}, Δp_T and SciHi reqirements for both: target-in and target-out. N_{backgr} is remained elastic and straight through backgrounds, which survived Δp_T cut. N_{beam} is number of incident protons, ϵ_{trig} is the trigger efficiency, . Quantity n_t is number of target particles per cm^2, details are on Table 1. The factor 10^4 is to bring the cross section in mbarns units.

We present results for both a)default events selection requirements and b)with an additional cut to reduce the straight throughs

21.1.1 Default event selection

Default event selection requirements:

- the interaction position should be around of the target
- the straight throughs are rejected by Δp_T >0.15 GeV/c cut
- SciHi trigger is on

Resulting input numbers and the σ_{inel} for p+p interactions at 58 GeV/c are shown in Table 42.

Figure 146 shows the Z_{vtx} and charged track multiplicities for p+p interactions at 58 GeV/c.

Comparison of our N_{ch} result with PDG using p+p interactions at 58 GeV/c are shown in Table 43

	Δp_T >0.15 GeV/c	Δp_T >0.25 GeV/c
N_{beam}	2.6206e+07	2.6206e+07
$N_{inel}(t-in)$	562704	507120
$N_{inel}(t-out)$	37920*5.196	34584*5.196
ϵ_{trig}	0.60±0.03	0.65±0.03
σ_{inel}, our	39.4 mb	32.6 mb
σ_{inel}, PDG	31.0 mb	31.0 mb
σ_{inel}, DPMJET	30.6 mb	30.6 mb

Table 42: The input numbers and the σ_{inel} for p+p interactions at 58 GeV/c. Factor 5.196 in $N_{inel}(t-out)$ line is to bring target-out sample size to same value as target-in. Δp_T >0.15 GeV/c cut is default value for the neutron analysis. n_t=5.922 for the liquid hydrogen.

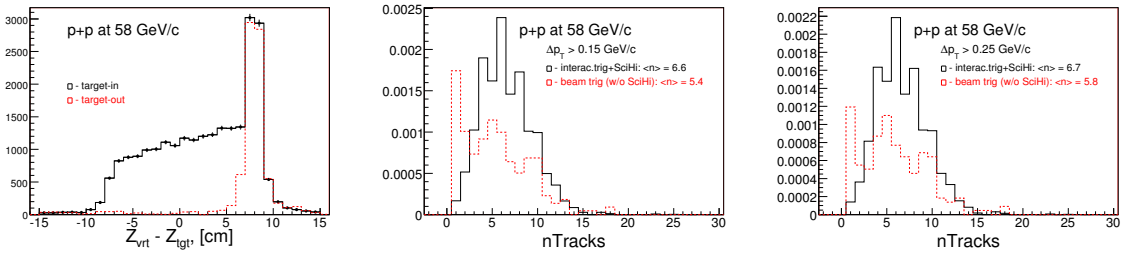

Figure 146: The Z_{vtx} (left) and charge track multiplicities (middle and right) for p+p interactions at 58 GeV/c. Multiplicities were normalized per single incident proton for events passed Z_{vtx}, Δp_T and SciHi requirements (in black) and beam trigger events passed Z_{vtx} and Δp_T cuts only (in red, not in scale). Target-out subtraction were applied. nTrks=1 in red plots illustrate the presence of the straight throughs. In black nTrks=1,2 are reduced by SciHi.

	Our	PDG
N_{ch}, Δp_T >0.15 GeV/c	5.4	6.0
N_{ch}, Δp_T >0.25 GeV/c	5.8	6.0

Table 43: Comparison of our N_{ch} with PDG. Our results are based on the unbias trigger data (without SciHi requirements).

	Δp_T >0.15 GeV/c	Δp_T >0.25 GeV/c
N_{beam}	3.1373e+07	3.1373e+07
$N_{inel}(t-in)$	771367	703865
$N_{inel}(t-out)$	79653*3.278	73626*3.278
ϵ_{trig}	0.66±0.02	0.71±0.03
σ_{inel}, our	41.7 mb	35.0 mb
σ_{inel}, PDG	31.0 mb	31.0 mb
σ_{inel}, DPMJET	30.9 mb	30.9 mb

Table 44: The input numbers and the σ_{inel} for p+p interactions at 84 GeV/c. Δp_T >0.15 GeV/c is default value for the neutron analysis.

The input numbers and the σ_{inel} for p+p interactions at 84 GeV/c are shown in Table 44.

Figure 147 shows the Z_{vtx} and charged track multiplicities for p+p interactions at 84 GeV/c

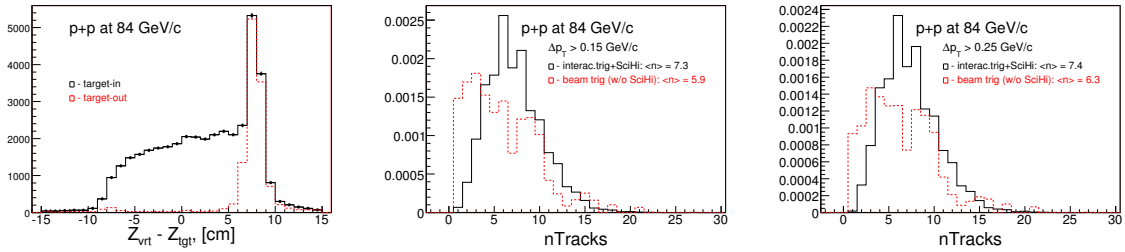

Figure 147: The Z_{vtx} (left) and charge track multiplicities (middle and right) for p+p interactions at 84 GeV/c. Multiplicities were normalized per single incident proton for events passed Z_{vtx}, Δp_T and SciHi requirements (in black) and beam trigger events passed Z_{vtx} and Δp_T cuts only (in red, not in scale). Target-out subtraction were applied. nTrks=1 in red plots illustrate the presence of the straight throughs. In black nTrks=1,2 are reduced by SciHi. N_{ch} PDG is 7.0

By viewing above results someone might come-up with an idea why we not using more tight Δp_T cut? Another possible question: If an input sample size for the neutron analysis is about 30% higher than what supposed to be, then what is possible impact to the neutron cross section? Short answer would be: In neutron selection we have an additional cut to reduce the straight throughs: Event rejected if there charged track with p_{trk} >0.7*P_{beam}. Figure 148 shed some lights on this.

Results for the neutron cross section with more tight Δp_T cut shown on Table 45

From σ_{inel} studies we might conclude:

- σ_{inel} with the default cuts appear to be about 30% higher than PDG value

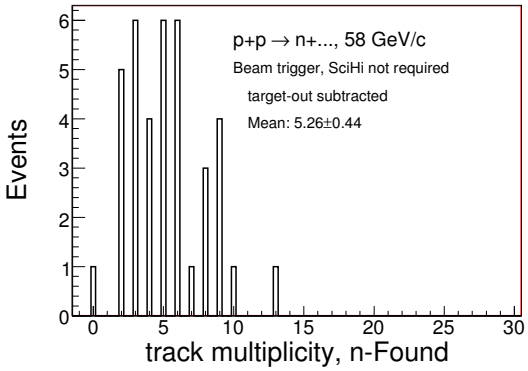

Figure 148: Charged track multiplicities for neutron candidates from p+p interactions at 58 GeV/c. Requirements: beam trigger, SciHi not required, target-out subtracted.

	Δp_T >0.15 GeV/c	Δp_T >0.25 GeV/c	variation
20 GeV/c	2.2±0.3 mb	1.9±0.3 mb	0.14±0.14
58 GeV/c	8.2±1.0 mb	7.2±0.9 mb	0.12±0.12
84 GeV/c	12.3±1.5 mb	11.0±1.4 mb	0.11±0.12

Table 45: Neutron cross section, $\int \frac{d\sigma}{dp}$ (discussed on following pages), calculated for different Δp_T cuts from p+p→n+X. NOTE: for Δp_T >0.25 GeV/c results were used the same the trigger efficiency, neutron selection efficiency and background level as for Δp_T >0.15 GeV/c case. But it might be not correct.

- tightening of Δp_T cut, which helps to reduce the background, lead to better agreement with PDG (30% →10%).

- tightening of Δp_T cut for the neutron analysis reduces the neutron cross section value in level of one uncertainty. This variation can be overestimated.

21.1.2 An additional cut to reject the straight throughs

For this study we implemented the additional cut to reject remained straight throughs: reject event if charged track has p_{trk} >0.7*P_{beam}. This cut is in use to select neutrons.

Results with the additional cut for p+p interactions are presented in Table 46

beam momentum	20 GeV/c	58 GeV/c	84 GeV/c
N_{beam}	2.2155e+06	2.6206e+07	3.1373e+07
$N_{inel}(t-in)$	24492	496464	697154
$N_{inel}(t-out)$	1929*3.98	32856*4.364	70581*3.347
ϵ_{trig}	0.65±0.03	0.78±0.03	0.73±0.02
σ_{inel}, our	19.6 mb	29.2 mb	33.7 mb
σ_{inel}, PDG	30.5 mb	31.0 mb	31.4 mb
σ_{inel}, DPMJET	30.5 mb	30.6 mb	30.9 mb

Table 46: Inelastic cross sections for pp interactions at 20, 58 and 84 GeV/c. Our result for the momentum of 20 GeV/c is 30% below of expectation. Partially it can be explained by presence of 25% of pions in beam, where the $\sigma_{inel}(\pi^+ p)$=20 mb

Figure 149 shows the comparison of the σ_{inel} as a function of the charged track multiplicity for data and MC using p+p interactions at 20, 58 and 84 GeV/c.

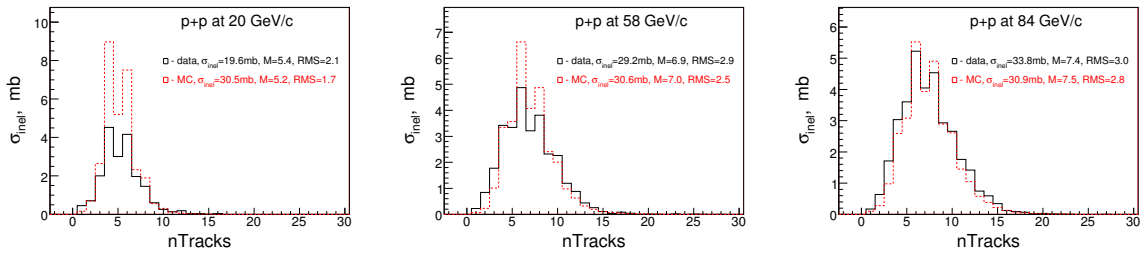

Figure 149: Comparison of the σ_{inel} as a function of the charged track multiplicity for data and MC using p+p interactions at 20, 58 and 84 GeV/c

Below we present the inelastic cross section results for heavier targets. The input numbers and the σ_{inel} for pC and pBi interactions at 58 and 120 GeV/c proton beams are shown in Table 47.

Figure 150 shows the pC and pPb σ_{inel} world data presented as a function of the proton momentum.

	p+C	p+C	p+Bi	p+Bi
P_{beam}	58 GeV/c	120 GeV/c	58 GeV/c	120 GeV/c
N_{beam}	8.7518e+06	5.5421e+06	2.1832e+07	2.8955e+07
$N_{inel}(t-in)$	199944	101513	261096	282351
$N_{inel}(t-out)$	46797*0.545	26592*0.665	58942*1.239	35096*2.579
ϵ_{trig}	0.82±0.07	0.85±0.02	0.84±0.04	0.78±0.02
n_t	0.8408	0.8408	0.0487	0.0487
σ_{inel}, our	289 mb	212 mb	2108 mb	1736 mb
σ_{inel},FLUKA	286 mb	287 mb	1875 mb	1880 mb
σ_{inel},LAQGSM	265 mb	266 mb	1674 mb	1676 mb

Table 47: Inelastic cross sections for pC and pBi interactions at 58 and 120 GeV/c. Note: p+Bi data calculated w/o nTrack<30 and $p_{sum} < 1.1 * P_{beam}$ cuts.

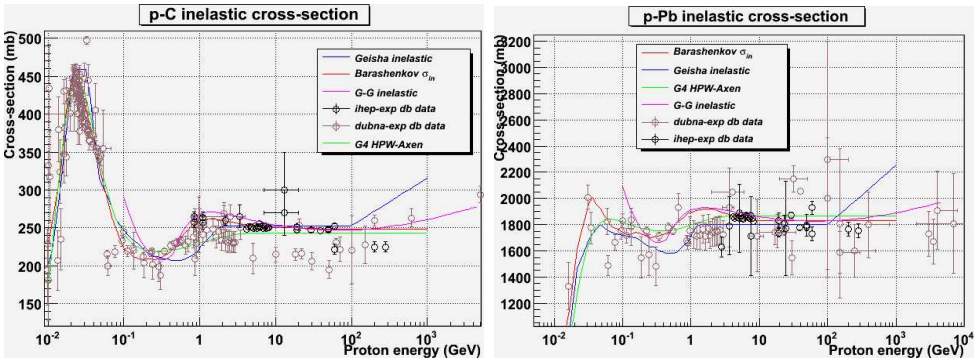

Figure 150: pC and pPb inelastic cross section world data presented as a function of the proton momentum.

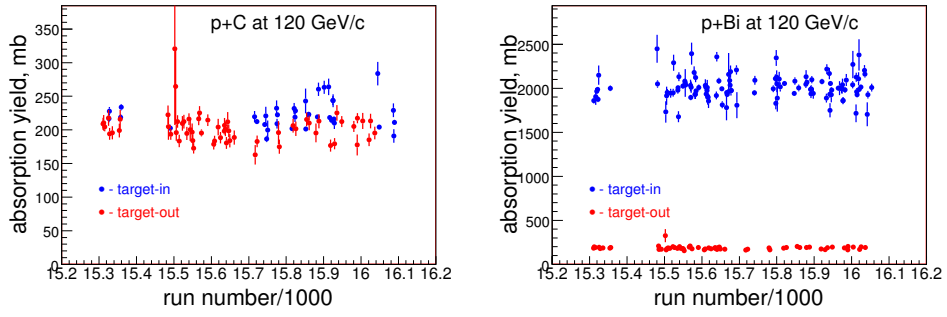

Figure 151: Absorption rate as a function of the run number for 120 GeV beam momentum. Blue: the trigger efficiency and target-out subtraction were NOT applied. Red: interactions with the trigger scintillator.

Figure 151 shows the pC and pBi absorption rates as a function of the run number.

Figure 152 shows the comparison of the σ_{inel} as a function of the charged track multiplicity for data and MC using p+p interactions at 20, 58 and 84 GeV/c.

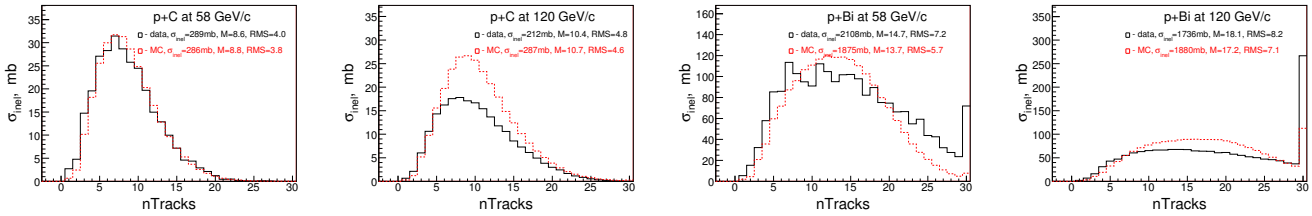

Figure 152: Comparison of the σ_{inel} as a function of the charged track multiplicity for data and MC using p+C and p+Bi interactions at 58 and 120 GeV/c

21.2 Cross section with the calorimeter's geometrical acceptance correction applied

The forward neutron production cross section calculated as:

$$\frac{d\sigma_n}{dp} = \frac{N_n(t-in)-N_n(t-out)-N_n(backgr)}{N_{beam}\times\epsilon_{trig}\times\epsilon_{hcal}\times\epsilon_{cuts}\times\Delta p} \times \frac{1}{n_t} \times 10^4, \text{ mb/(GeV/c)}$$

where, N_n is number of the neutron candidates passing the selection requirements, where t-in and t-out are target-in and target-out respectively. $N_n(backgr)$ is the background, N_{beam} is the number of incident protons, ϵ_{trig} is the trigger efficiency, ϵ_{hcal} is the calorimeter acceptance, ϵ_{cuts} is the neutron selection efficiency, Δp is momentum bin width. Quantity n_t is number of target particles per cm^2, details are on Table 1. The factor 10^4 is to bring the cross section in mbarns units.

The inclusive forward neutron production cross sections are summarized in Table 48.

	σ_n(detect)	σ_n(corr)	stat.	tot.syst.	syst-2
H_2-20	0.7	18.0	±1.0	±5.4	±2.5
H_2-58	5.2	16.4	±0.2	±3.2	±2.1
Be-58	39.8	109.6	±6.5	±24.0	±17.1
C-58	44.3	126.2	±3.0	±25.4	±14.6
Bi-58	213.7	792.9	±18.0	±196.2	±112.2
U-58	199.5	730.3	±10.0	±183.4	±107.0
H_2-84	8.7	16.9	±0.2	±2.5	±2.1
Be-120	64.8	84.2	±0.3	±13.0	±12.1
C-120	76.3	99.8	±0.5	±14.0	±12.7
Bi-120	379.3	555.7	±2.0	±108.4	±94.7

Table 48: The inclusive forward neutron production cross section within the neutron momentum range from p_{min} up to the beam momentum value using p+A collisions at different momentum of the incident protons. The cross section units are in mbarn. Last column represents the total systematics without HCAL acceptance uncertainty included.

Figure 153 shows the forward neutron production cross section for p+p interactions at 20, 58 and 84 GeV/c with the total systematic uncertainties superimposed.

Figure 154 shows the forward neutron production cross section for p+Be and p+C interactions at 58 GeV/c with the total systematic uncertainties superimposed.

Figure 155 shows the forward neutron production cross section for p+Bi and p+U interactions at 58 GeV/c with the total systematic uncertainties superimposed.

Figure 156 shows the forward neutron production cross section for p+Be, p+C and p+Bi interactions at 120 GeV/c with the total systematic uncertainties superimposed.

Figure 157 shows the forward neutron production cross section as a function of the target atomic weight.

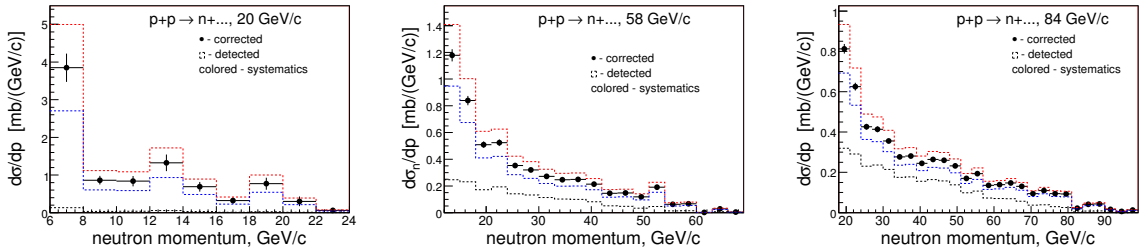

Figure 153: The forward neutron production cross section for p+p interactions at 20 (left), 58 (middle) and 84 GeV/c with the total systematic uncertainties superimposed.

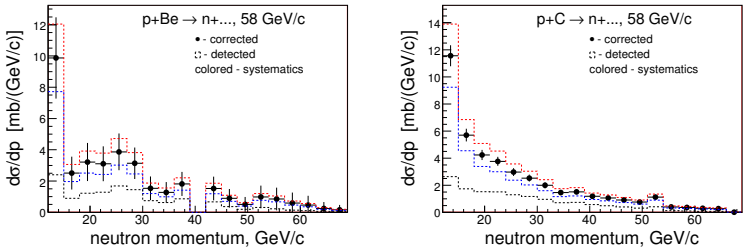

Figure 154: The forward neutron production cross section for p+Be (left) and p+C (right) interactions at 58 GeV/c with the total systematic uncertainties superimposed.

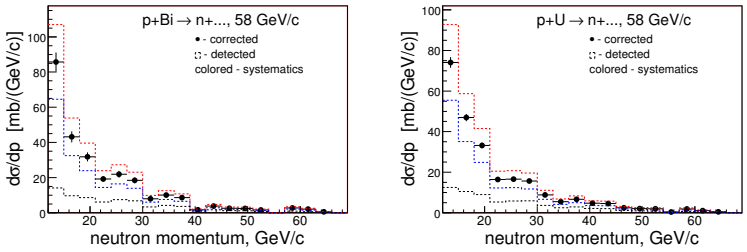

Figure 155: The forward neutron production cross section for p+Bi (left) and p+U (right) interactions at 58 GeV/c with the total systematic uncertainties superimposed.

58 GeV/c	coefficient	power
Total syst	28.4 ± 8.4	0.606 ± 0.075
w/o HCAL syst	28.2 ± 5.2	0.607 ± 0.046

Table 49: The fit parameters of the production cross section as a function of the target atomic weight using incident protons at 58 GeV/c.

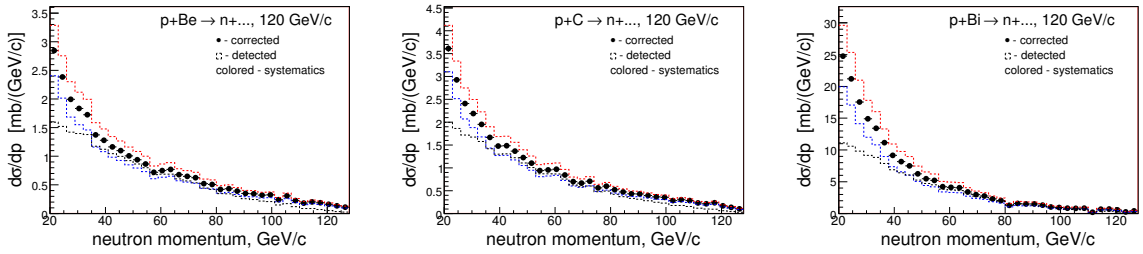

Figure 156: The forward neutron production cross section for p+Be (left), p+C (middle) and p+Bi(right) interactions at 120 GeV/c with the total systematic uncertainties superimposed.

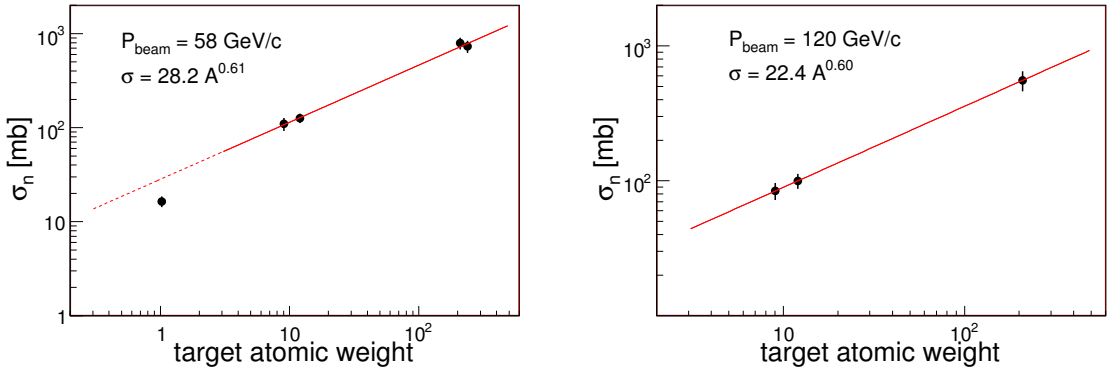

Figure 157: The forward neutron production cross section as a function of the target atomic weight with the incident proton momentum of 58 GeV/c (left) and 120 GeV/c (right), respectively. On left plot H_2 data point is not included to the fit.

The fit parameters for 58 GeV/c data are shown in Table 49.
The fit parameters for 120 GeV/c data are shown in Table 50.

120 GeV/c	coefficient	power
Total syst	22.4 ± 5.4	0.601 ± 0.074
w/o HCAL syst	22.4 ± 4.8	0.601 ± 0.065

Table 50: The fit parameters of the production cross section as a function of the target atomic weight using incident protons at 120 GeV/c.

21.3 Cross section for case when the geometrical acceptance correction was NOT applied

21.3.1 Results for data

The neutron production cross section for case without acceptance corrections was calculated as:

$$\frac{d\sigma_n}{dp} = \frac{N_n(t-in) - N_n(t-out) - N_n(backgr)}{N_{beam} \times \epsilon_{trig} \times \epsilon_{cuts} \times \Delta p} \times \frac{1}{n_t} \times 10^4, \text{ mb/(GeV/c)}$$

Figure 158 shows the forward neutron production cross section for case without geometrical acceptance corrections applied using p+p interactions at 20, 58 and 84 GeV/c.

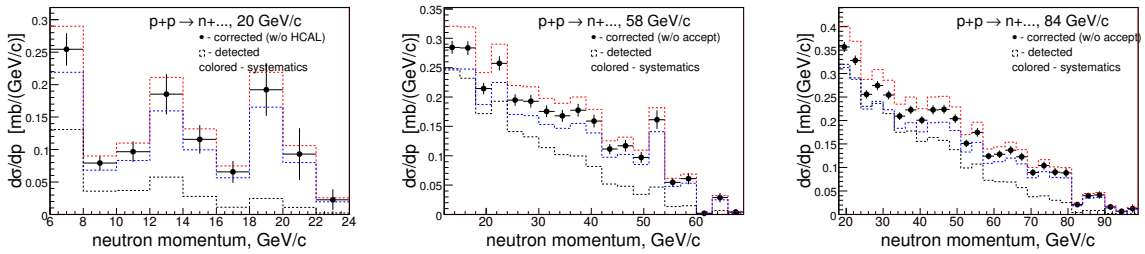

Figure 158: The forward neutron production cross section for case without geometrical acceptance corrections applied using p+p interactions at 20 (left), 58 (middle) and 84 GeV/c.

Figure 159 shows the forward neutron production cross section for case without geometrical acceptance corrections applied using p+Be and p+C interactions at 58 GeV/c.

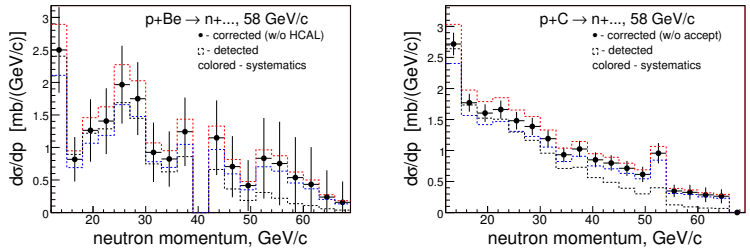

Figure 159: The forward neutron production cross section for case without geometrical acceptance corrections applied using p+Be (left) and p+C (right) interactions at 58 GeV/c.

Figure 160 shows the forward neutron production cross section for case without geometrical acceptance corrections applied using p+Bi and p+U interactions at 58 GeV/c.

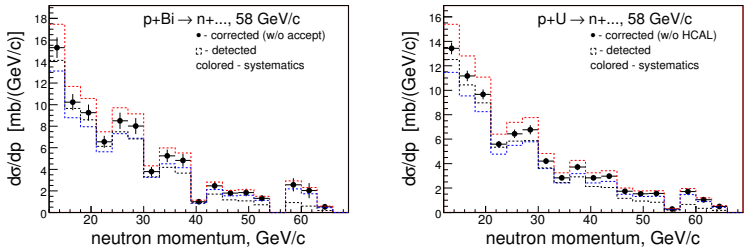

Figure 160: The forward neutron production cross section for case without geometrical acceptance corrections applied using p+Bi (left) and p+U (right) interactions at 58 GeV/c.

Figure 161 shows the forward neutron production cross section for case without geometrical acceptance corrections applied using p+Be, p+C and p+Bi interactions at 120 GeV/c.

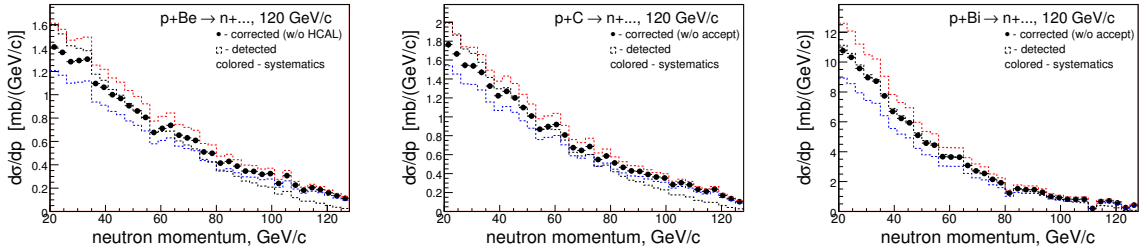

Figure 161: The forward neutron production cross section for case without geometrical acceptance corrections applied using p+Be (left), p+C (middle) and p+Bi(right) interactions at 120 GeV/c.

The inclusive forward neutron production cross sections for case without geometrical acceptance corrections applied are summarized in Table 51.

21.3.2 Comparison with NA49 results

Figure 162 shows comparison of our results from p+p at 58 and 84 GeV/c with results from p+p at 158 GeV/c, NA49 experiment.

21.3.3 Comparison with Monte Carlo

Below we will present comparison of the measured neutron cross section, where data NOT corrected for the HCAL acceptance, with Monte Carlo neutron cross section. Requirements for MC: neutrons within HCAL geometry and $p_n > p_{min}$. Figure 163 shows comparison of the forward neutron production cross section with Monte Carlo results using p+p, p+C and p+Bi interactions at 58 GeV/c.

	σ_n(detect)	σ_n(corr)	stat.	tot.syst.
H_2-20	0.7	2.2	$\pm$0.1	$\pm$0.3
H_2-58	5.2	8.2	$\pm$0.1	$\pm$1.0
Be-58	39.8	53.7	$\pm$3.2	$\pm$8.4
C-58	44.3	56.8	$\pm$1.3	$\pm$6.6
Bi-58	213.7	255.9	$\pm$5.8	$\pm$36.2
U-58	199.5	234.0	$\pm$3.2	$\pm$34.3
H_2-84	8.7	12.3	$\pm$0.1	$\pm$1.5
Be-120	64.8	68.1	$\pm$0.2	$\pm$9.8
C-120	76.3	79.9	$\pm$0.4	$\pm$10.1
Bi-120	379.3	379.7	$\pm$1.4	$\pm$64.7

Table 51: The inclusive forward neutron production cross section calculated without HCAL geometrical acceptance corrections applied.

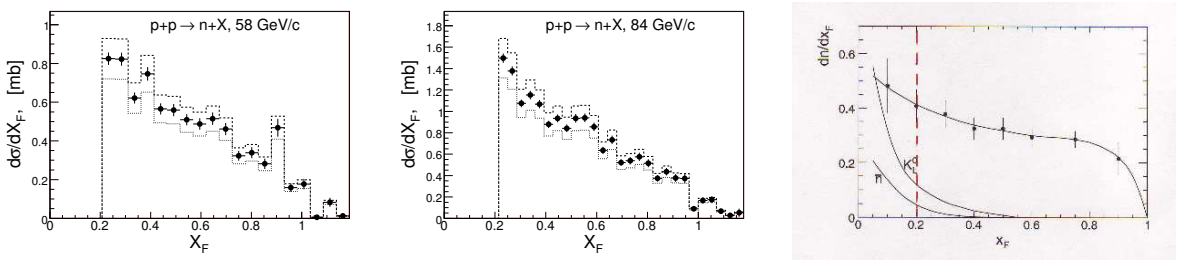

Figure 162: The comparison of our results from p+p at 58 (left) and at 84 GeV/c (middle) with results from p+p at 158 GeV/c, NA49, (right).

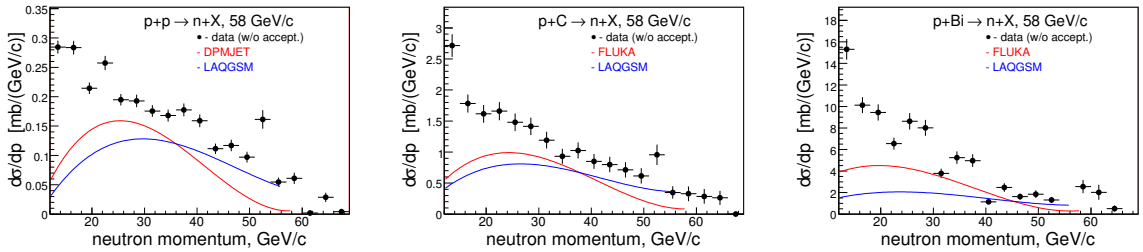

Figure 163: The comparison of forward neutron production cross section from data with Monte Carlo cross section using p+p (left), p+C (middle) and p+Bi (right) interactions at 58 GeV/c. Data were corrected for everything, except HCAL acceptance. Requirements for MC: neutrons within HCAL geometry and $p_n > p_{min}$.

Figure 164 shows comparison of the forward neutron production cross section with Monte Carlo results using p+p at 84 GeV/c and p+C and p+Bi interactions at 120 GeV/c. .

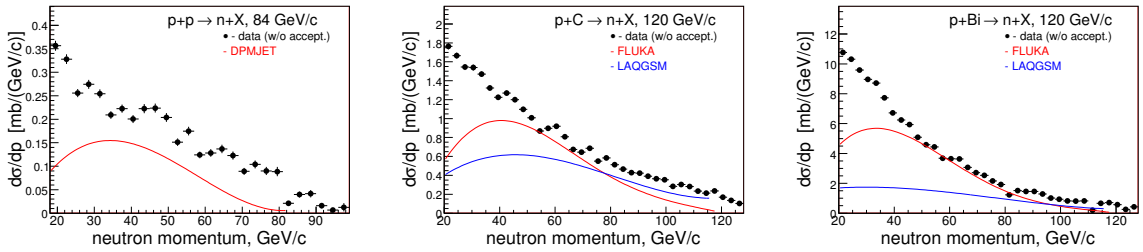

Figure 164: The comparison of forward neutron production cross section with Monte Carlo results using p+p at 84 GeV/c (left), p+C (middle) and p+Bi (right) interactions at 120 GeV/c. Data were corrected for everything, except HCAL acceptance. Requirements for MC: neutrons within HCAL geometry and $p_n > p_{min}$..

Comparison of the production cross sections for case without geometrical acceptance corrections applied with Monte Carlo cross section are presented in Table 52.

	σ_n(data), mb	$\sigma_n(^{DPMJET}_{orFLUKA})$, mb	σ_n(LAQGSM), mb
H_2-20	2.2±0.3	0.80	
H_2-58	8.2±1.0	4.4	4.2
Be-58	53.7±9.0	16.5	
C-58	56.8±6.6	29.0	27.7
Bi-58	255.9±36.2	123.7	70.7
U-58	234.0±34.3	142.7	
H_2-84	12.3±1.5	6.0	
Be-120	68.1±9.8	29.7	
C-120	79.9±10.1	53.0	39.5
Bi-120	379.7±64.7	273.5	100.1

Table 52: Comparison of the neutron production cross sections for case without geometrical acceptance corrections applied with Monte Carlo cross section.

Figure 165 shows comparison of the MC neutron production cross section as function of the target atomic weight for FLUKA and LAQGSM at 58 and 120 GeV/c beam momenta. Requirements for Monte Carlo neutrons: within HCAL geometry and $p_n > p_{min}$.

21.3.4 Neutrals total cross section: data vs MC. More on K^o_L background

Figure 166 shows Monte Carlo neutrals multiplicities per single pp interactions at 20 GeV/c and comparison of K^o_L with $K^{\pm}$ spectra vs x_F variable.

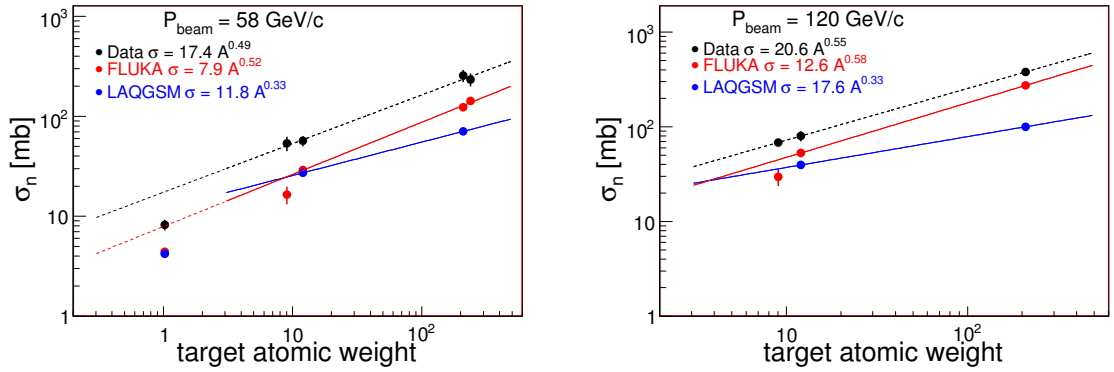

Figure 165: The data vs MC comparison of the neutron production cross section as function of the target atomic weight at 58 (left) and 120 (right) GeV/c beam momenta. Requirements for Monte Carlo neutrons: within HCAL geometry and $p_n > p_{min}$.

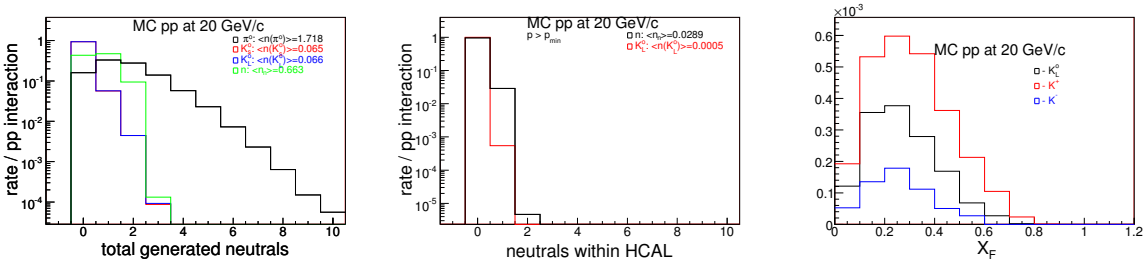

Figure 166: The neutrals multiplicities distributions per single inelastic pp interaction at 20 GeV/c: left - without cuts, middle - neutrals required to be pointing to HCAL volume and p>p_{min}. Right - comparison of K^o_L with $K^{\pm}$ spectra vs x_F variable

Neutrals average multiplicities per single pp interactions and total cross sections at 20 GeV/c are summarized in Table 53.

	$< n_{MC} >$	$< n_{data-W} >$	σ_{MC}	σ_{data-W}
π^o	1.719	1.55	52.4 mb	45±4 mb
K^o_s	0.065	0.05	2.0 mb	1.3±? mb
K^o_L	0.066	n/a	2.0 mb	1.3 mb(pred)
n	0.663	n/a	20.2 mb	n/a

Table 53: Neutrals average multiplicities per single pp interactions and total cross sections at 20 GeV/c. MC prod. cross section: 30.5 mb. $< \pi^o >$ in data was calculated as: $< \pi^o >$ = -0.82 + 0.79*ln(p_{lab}) - J.Withmore Physics Reports 27, No.5 (1976) 187-273. $\sigma_{MC} =< n_{MC} >$ * 30.5 mb

Neutron and K^o_L average multiplicities per single pp interactions and cross sections at 20 GeV/c are summarized in Table 54.

	$< n >$	σ_{MC}	$\sigma_{data}(\int \frac{d\sigma}{dp})$
n	0.0289	0.88 mb	2.2±0.3 mb
K^o_L	0.0005	0.015 mb	n/a
K^o_L/n	0.017		

Table 54: n and K^o_L are within HCAL and p>p_{min}. Background level is 0.007 per neutron. It looks like that 0.01 of K^o_L contribution is remained there.

Figure 167 shows Monte Carlo neutrals multiplicities per single pp interactions at 58 GeV/c and comparison of K^o_L with $K^{\pm}$ spectra vs x_F variable.

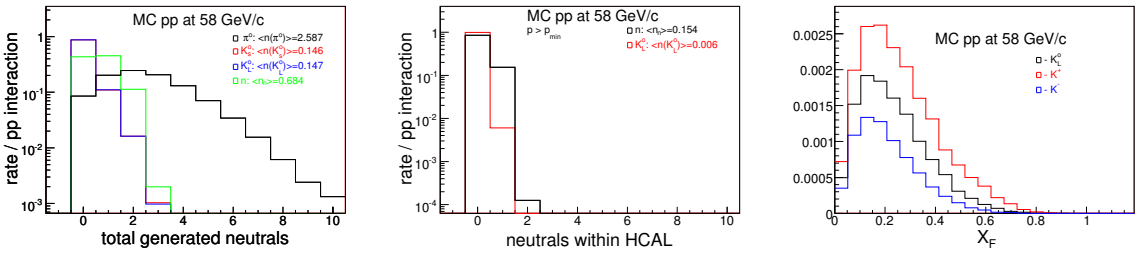

Figure 167: The neutrals multiplicities distributions per single inelastic pp interaction at 58 GeV/c: left - without cuts, middle - neutrals required to be pointing to HCAL volume and p>p_{min}. Right - comparison of K^o_L with $K^{\pm}$ spectra vs x_F variable

Neutrals average multiplicities per single pp interactions and total cross sections at 58 GeV/c are summarized in Table 55.

Neutron and K^o_L average multiplicities per single pp interactions and cross sections at 58 GeV/c are summarized in Table 56.

	$< n_{MC} >$	$< n_{data-W} >$	σ_{MC}	σ_{data-W}
π^o	2.587	2.39	79.2 mb	81±4 mb (69GeV)
K_s^o	0.146	0.13±0.03	4.5 mb	4±1 mb (69GeV)
K_L^o	0.147	n/a	4.5 mb	4±1 mb(pred)
n	0.684	n/a	20.9 mb	n/a

Table 55: Neutrals average multiplicities per single pp interactions and total cross sections at 58 GeV/c. MC prod. cross section: 30.6 mb. $< \pi^o >$ in data was calculated as: $< \pi^o >$ = -0.82 + 0.79*ln(p_{lab}). $\sigma_{MC} =< n_{MC} >$ * 30.6 mb

	$< n >$	σ_{MC}	$\sigma_{data}(\int \frac{d\sigma}{dp})$
n	0.154	4.7 mb	8.2±1.0 mb
K_L^o	0.006	0.18 mb	n/a
K_L^o/n	0.04		

Table 56: n and K_L^o are within HCAL and p>p_{min}. Estimated background level for this data is 0.082 per single neutron candidate.

Figure 168 shows Monte Carlo neutrals multiplicities per single pp interactions at 84 GeV/c and comparison of K_L^o with $K^{\pm}$ spectra vs x_F variable.

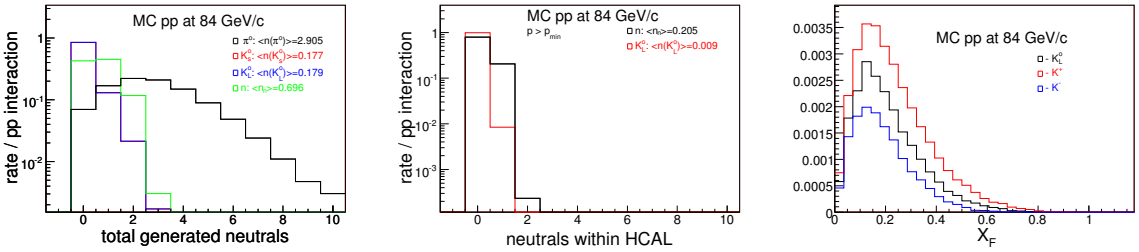

Figure 168: The neutrals multiplicities distributions per single inelastic pp interaction at 84 GeV/c: left - without cuts, middle - neutrals required to be pointing to HCAL volume and p>p_{min}. Right - comparison of K_L^o with $K^{\pm}$ spectra vs x_F variable

Neutrals average multiplicities per single pp interactions and total cross sections at 84 GeV/c are summarized in Table 57.

Neutron and K_L^o average multiplicities per single pp interactions and cross sections at 84 GeV/c are summarized in Table 58.

From above studies we observed:

- the neutron production cross section in our data, ($\int \frac{d\sigma}{dp}$), systematically higher than the prediction from DPMJET, by factor 2.
- K_s^o/K_L^o production cross section in DPMJET is slightly higher than the existing inclusive K_s^o production data, J.Whitmore Physics Reports 27, No.5 (1976) 187-273.

	$< n_{MC} >$	$< n_{data-W} >$	σ_{MC}	σ_{data-W}
π^o	2.905	2.68	89.6 mb	83±4 mb ($\frac{69+102}{2}$GeV)
K_s^o	0.177	0.14±0.02	5.5 mb	4.3±1 mb ($\frac{69+102}{2}$GeV)
K_L^o	0.179	n/a	5.5 mb	4.3±1 mb(pred)
n	0.696	n/a	21.5 mb	n/a

Table 57: Neutrals average multiplicities per single pp interactions and total cross sections at 84 GeV/c. MC prod. cross section: 30.9 mb. $< \pi^o >$ in data was calculated as: $< \pi^o >$ = -0.82 + 0.79*ln(p_{lab}). $\sigma_{MC} =< n_{MC} >$ * 30.9 mb

	$< n >$	σ_{MC}	$\sigma_{data}(\int \frac{d\sigma}{dp})$
n	0.205	6.5 mb	12.3±1.5 mb
K_L^o	0.009	0.28 mb	n/a
K_L^o/n	0.04		

Table 58: n and K_L^o are within HCAL and p>p_{min}. Estimated background level for this data is 0.117 per single neutron candidate.

- our background estimates covers well the K_L^o contribution. It is consistent for 20 GeV/c data within 1-2% level. For 58 and 84 GeV/c data predicted K_L^o contributions are not greater than half of what we considering as the total background.

One can conclude that K_L^o contribution in our data is not underestimated.

21.4 Invariant cross section with the calorimeter's solid angle included

The invariant inclusive neutron production cross section was calculated as:

$$\frac{E}{p^2\Omega}\frac{d\sigma}{dp} = \frac{E}{p^2\Omega} \times \frac{n_n(t-in)-n_n(t-out)-n_n(backgr)}{N_{beam}\times\epsilon_{trig}\times\epsilon_{cuts}\times\Delta p} \times \frac{1}{n_t} \times 10^4, \text{ mb/(GeV/c)}^2\text{/sr}$$

where Ω is the calorimeter's solid angle, presented in Table 28

Figure 169 shows the forward neutron production cross section for p+p interactions at 20, 58 and 84 GeV/c with the total systematic uncertainties superimposed.

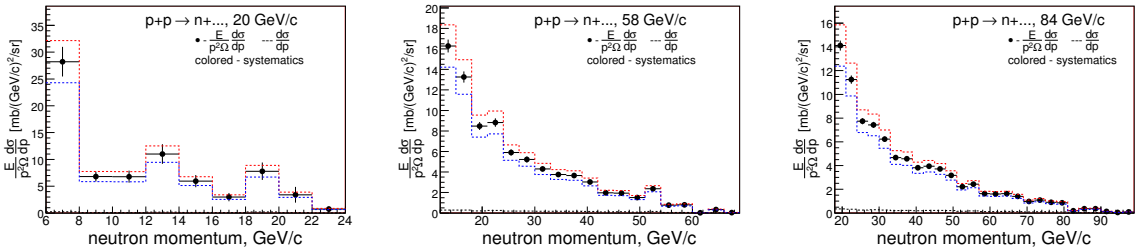

Figure 169: The forward neutron production cross section for p+p interactions at 20 (left), 58 (middle) and 84 GeV/c with the total systematic uncertainties superimposed.

Figure 170 shows the forward neutron production cross section for p+Be and p+C interactions at 58 GeV/c with the total systematic uncertainties superimposed.

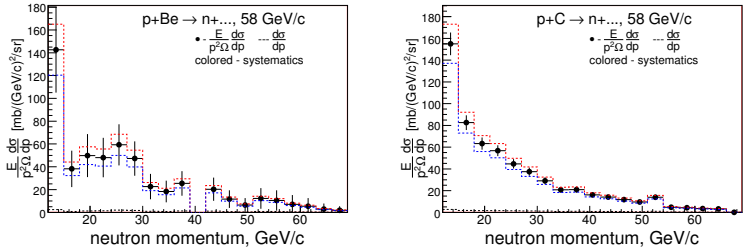

Figure 170: The forward neutron production cross section for p+Be (left) and p+C (right) interactions at 58 GeV/c with the total systematic uncertainties superimposed.

Figure 171 shows the forward neutron production cross section for p+Bi and p+U interactions at 58 GeV/c with the total systematic uncertainties superimposed.

Figure 172 shows the forward neutron production cross section for p+Be, p+C and p+Bi interactions at 120 GeV/c with the total systematic uncertainties superimposed.

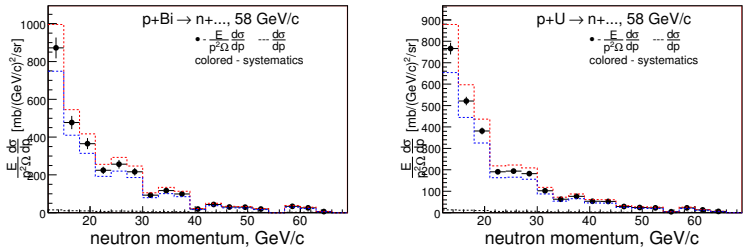

Figure 171: The forward neutron production cross section for p+Bi (left) and p+U (right) interactions at 58 GeV/c with the total systematic uncertainties superimposed.

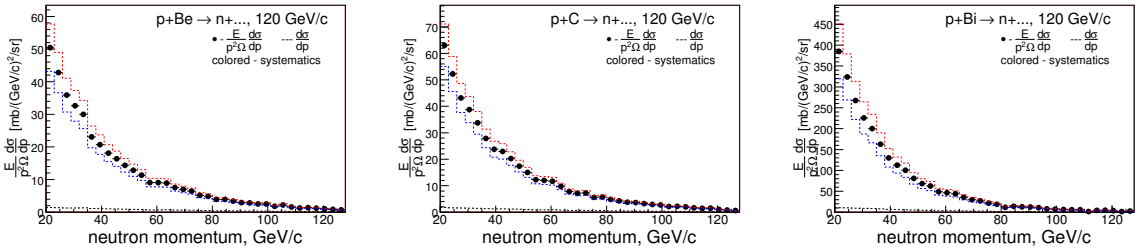

Figure 172: The forward neutron production cross section for p+Be (left), p+C (middle) and p+Bi(right) interactions at 120 GeV/c with the total systematic uncertainties superimposed.

21.5 Cross section as a function of the variable x_F

21.5.1 Cross section when the geometrical acceptance correction was NOT applied

The neutron production cross section (without acceptance corrections) as a function of variable x_F was calculated as:

$$\frac{d\sigma}{dX_F} = \frac{[N_n(t-in)-N_n(t-out)-N_n(backgr)]\times p_{max}}{N_{beam}\times\epsilon_{trig}\times\epsilon_{cuts}\times p_n} \times \frac{1}{n_t} \times 10^4, \text{ mb}$$

where p_n is neutron momentum, p_{max} is the beam momentum in lab system. The initial cross section calculations made for the neutron momentum bin width, Δp_n, of 2, 3, 3 and 3 GeV/c for 20, 58, 84 and 120 GeV/c data, respectively. If we want to use the same target-out, background and neutron selection efficiencies as before, then the corresponding X_F bin widths would be 0.10, 0.0517, 0.0357 and 0.025, respectively. For purpose to compare results from different momenta and targets, the $\frac{d\sigma}{dX_F}$ values were calculated for the single unified bin width: 0.05. NOTE: if someone want to calculate the integral cross section from the plot, then the result would be not consistent with what presented in Table 51.

Figure 173 shows the forward neutron production cross section vs variable x_F using p+p interactions at 20, 58 and 84 GeV/c. The geometrical acceptance corrections NOT applied.

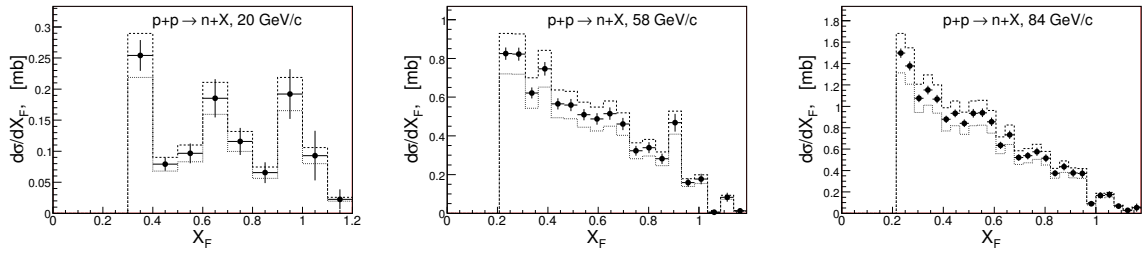

Figure 173: The forward neutron production cross section vs variable x_F using p+p interactions at 20 (left), 58 (middle) and 84 GeV/c. The geometrical acceptance corrections NOT applied.

Figure 174 shows the forward neutron production cross section vs variable x_F using p+Be and p+C interactions at 58 GeV/c. The geometrical acceptance corrections NOT applied.

Figure 175 shows the forward neutron production cross section vs variable x_F using p+Bi and p+U interactions at 58 GeV/c. The geometrical acceptance corrections NOT applied.

Figure 176 shows the forward neutron production cross section vs variable x_F using p+Be, p+C and p+Bi interactions at 120 GeV/c. The geometrical acceptance corrections NOT applied.

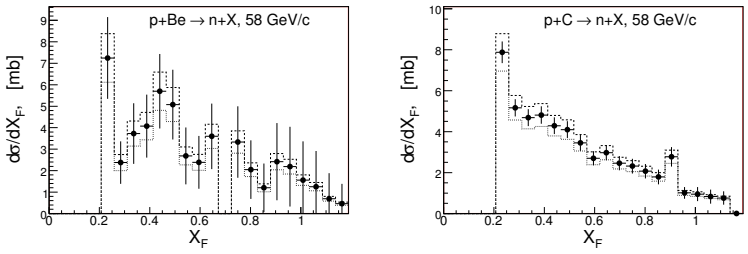

Figure 174: The forward neutron production cross section vs variable x_F using p+Be (left) and p+C (right) interactions at 58 GeV/c. The geometrical acceptance corrections NOT applied.

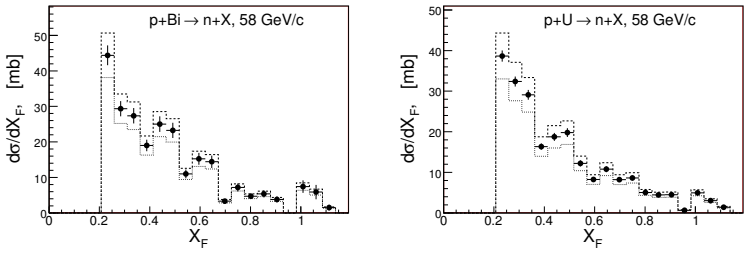

Figure 175: The forward neutron production cross section vs variable x_F using p+Bi (left) and p+U (right) interactions at 58 GeV/c. The geometrical acceptance corrections NOT applied.

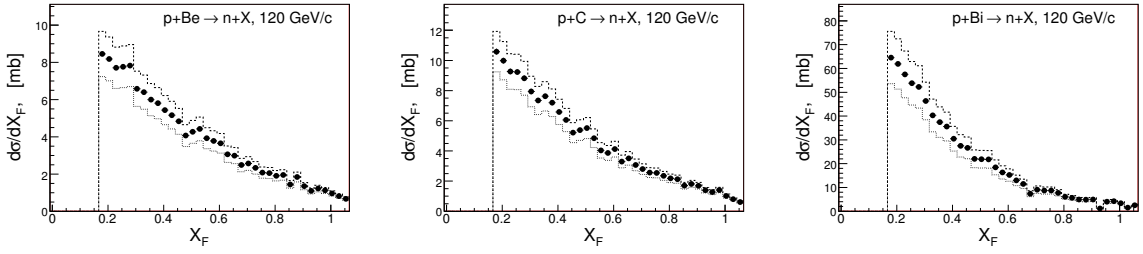

Figure 176: The forward neutron production cross section vs variable x_F using p+Be (left), p+C (center) and p+Bi (right) interactions at 120 GeV/c. The geometrical acceptance corrections NOT applied.

21.5.2 Cross section corrected for the geometrical acceptance

The neutron production cross section with acceptance corrections applied as a function of variable x_F was calculated as:

$$\frac{d\sigma}{dX_F} = \frac{[N_n(t-in) - N_n(t-out) - N_n(backgr)] \times p_{max}}{N_{beam} \times \epsilon_{trig} \times \epsilon_{cuts} \times \epsilon_{hcal} \times p_n} \times \frac{1}{n_t} \times 10^4, \text{ mb}$$

Figure 177 shows the forward neutron production cross section vs variable x_F using p+p interactions at 20, 58 and 84 GeV/c. The geometrical acceptance corrections were applied.

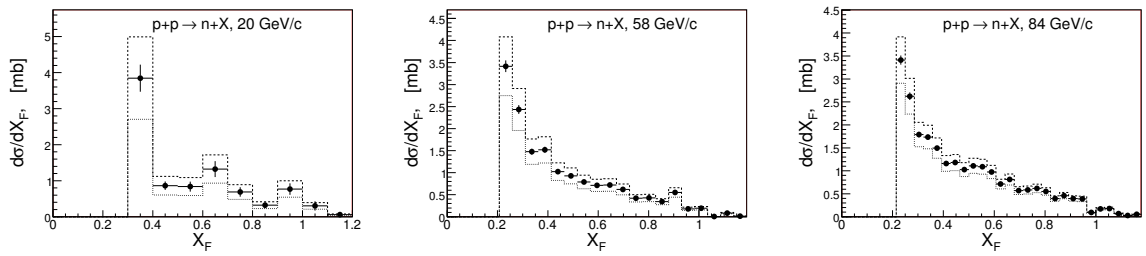

Figure 177: The forward neutron production cross section vs variable x_F using p+p interactions at 20 (left), 58 (middle) and 84 GeV/c. The geometrical acceptance corrections were applied.

Figure 178 shows the forward neutron production cross section vs variable x_F using p+Be and p+C interactions at 58 GeV/c. The geometrical acceptance corrections were applied.

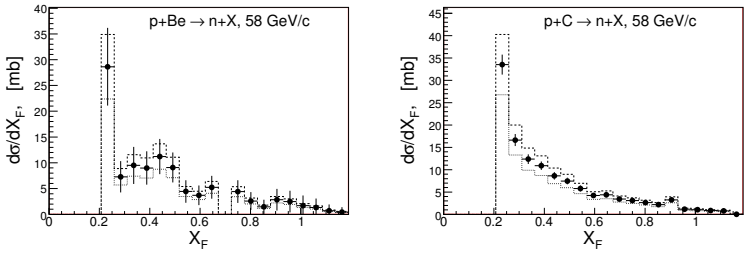

Figure 178: The forward neutron production cross section vs variable x_F using p+Be (left) and p+C (right) interactions at 58 GeV/c. The geometrical acceptance corrections were applied.

Figure 179 shows the forward neutron production cross section vs variable x_F using p+Bi and p+U interactions at 58 GeV/c. The geometrical acceptance corrections were applied.

Figure 180 shows the forward neutron production cross section vs variable x_F using p+Be, p+C and p+Bi interactions at 120 GeV/c. The geometrical acceptance corrections were applied.

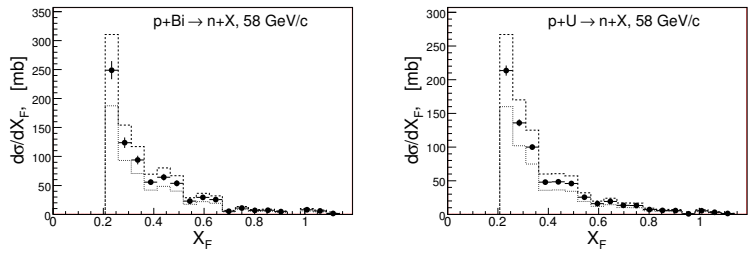

Figure 179: The forward neutron production cross section vs variable x_F using p+Bi (left) and p+U (right) interactions at 58 GeV/c. The geometrical acceptance corrections were applied.

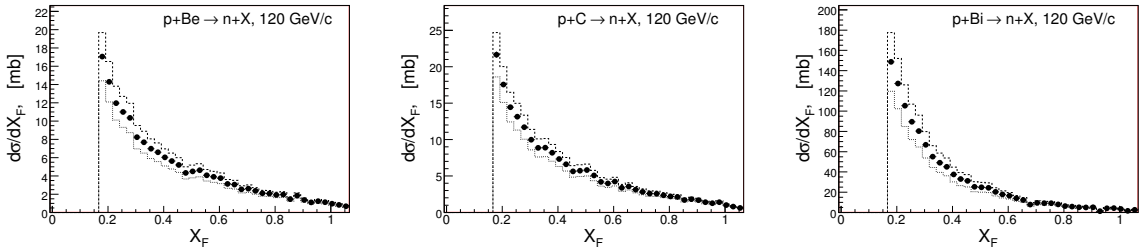

Figure 180: The forward neutron production cross section vs variable x_F using p+Be (left), p+C (center) and p+Bi (right) interactions at 120 GeV/c. The geometrical acceptance corrections were applied.

21.5.3 Invariant cross section

The invariant inclusive neutron production cross section as the function of variable x_F was calculated as:

$$\frac{E}{p^2\Omega}\frac{d\sigma}{dx_F} = \frac{E}{p^2\Omega} \times \frac{[N_n(t-in)-N_n(t-out)-N_n(backgr)]\times p_{max}}{N_{beam}\times\epsilon_{trig}\times\epsilon_{cuts}\times p_n} \times \frac{1}{n_t} \times 10^4, \text{ mb/(GeV/c)/sr}$$

Figure 181 shows the forward neutron production cross section for p+p interactions at 20, 58 and 84 GeV/c as the function of variable x_F.

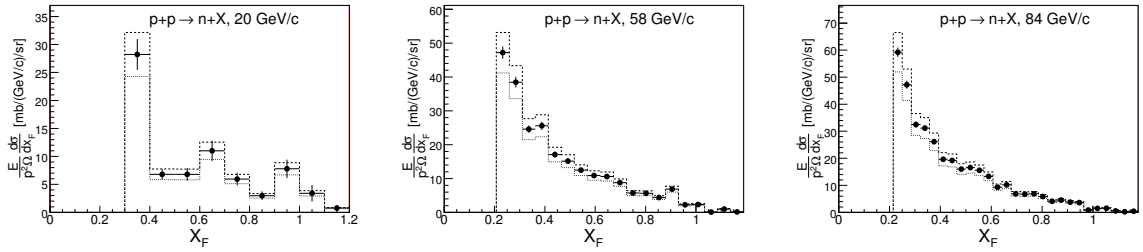

Figure 181: The neutron invariant cross section for p+p interactions at 20 (left), 58 (middle) and 84 GeV/c as the function of variable x_F.

Figure 182 shows the forward neutron production cross section for p+Be and p+C interactions at 58 GeV/c as the function of variable x_F.

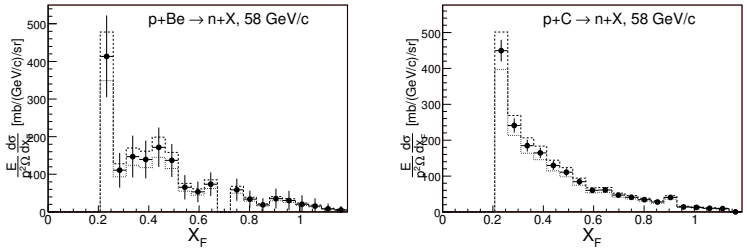

Figure 182: The neutron invariant cross section for p+Be (left) and p+C (right) interactions at 58 GeV/c as the function of variable x_F.

Figure 183 shows the forward neutron production cross section for p+Bi and p+U interactions at 58 GeV/c as the function of variable x_F.

Figure 184 shows the forward neutron production cross section for p+Be, p+C and p+Bi interactions at 120 GeV/c as the function of variable x_F.

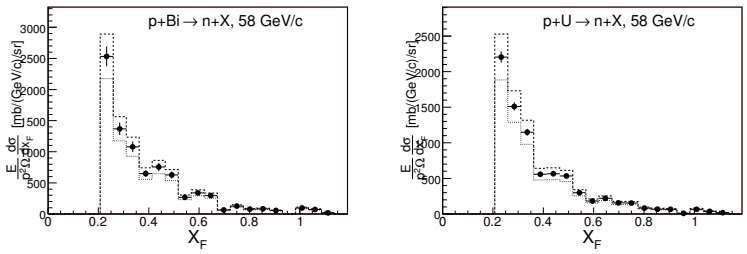

Figure 183: The neutron invariant cross section for p+Bi (left) and p+U (right) interactions at 58 GeV/c as the function of variable x_F.

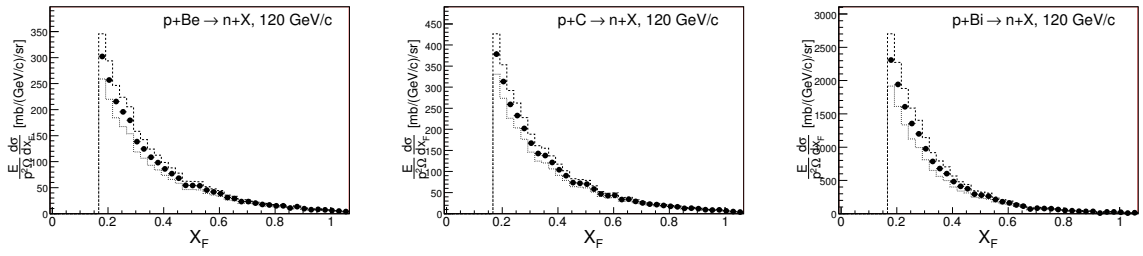

Figure 184: The neutron invariant cross section for p+Be (left), p+C (middle) and p+Bi(right) interactions at 120 GeV/c as the function of variable x_F.

22 Neutron Angular Distribution

22.1 Measurements with data

The neutron angular measurements using data is based on the unmatched shower position at EMCAL. All events passed the neutron selection requirements.

The angular distributions of the neutrons from the Be and C targets at 58 GeV/c are shown in Figure 185.

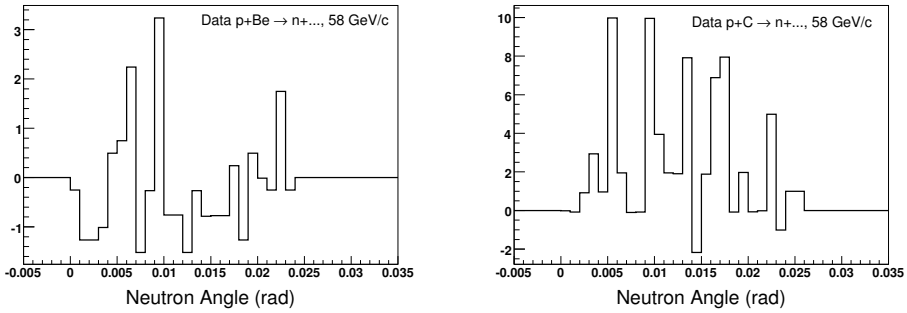

Figure 185: The neutron angular distributions from the Be and C targets at 58 GeV/c. The neutron angular measurements using data is based on the unmatched shower position at EMCAL. All events passed the neutron selection requirements.

The angular distributions of the neutrons from the Bi and U targets at 58 GeV/c are shown in Figure 186.

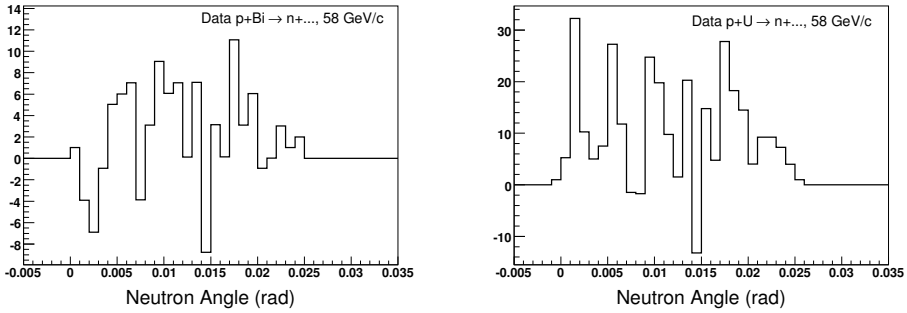

Figure 186: The neutron angular distributions from the Bi and U targets at 58 GeV/c. The neutron angular measurements using data is based on the unmatched shower position at EMCAL. All events passed the neutron selection requirements.

The angular distributions for the liquid hydrogen, 58 and 84 GeV/c momenta (on left), and thin targets at 120 GeV/c (on right) are shown in Figure 187.

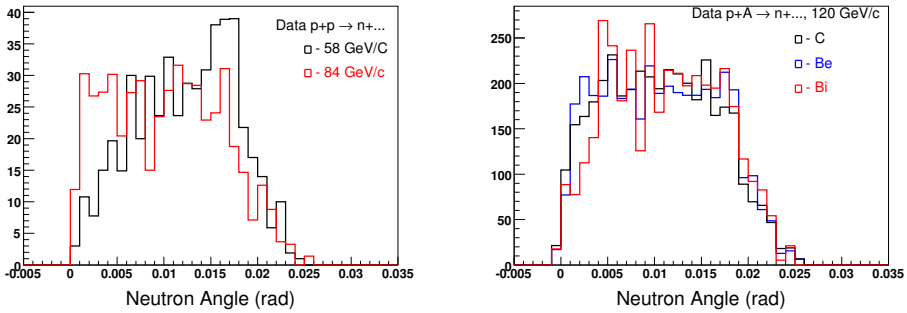

Figure 187: The neutron angular distributions for the liquid hydrogen target at 58 and 84 GeV/c (on left) and Be, C and Bi targets at 120 GeV/c (on right). The neutron angular measurements using data is based on the unmatched shower position at EMCAL. All events passed the neutron selection requirements. All distributions are brought to the same area size.

22.2 Neutron angle: data vs Monte Carlo

Below we will compare the neutron angular distributions from data with Monte Carlo. The angular distributions of the neutrons from Be, C and Bi targets at 120 GeV/c proton beam momentum are shown in Figure 188.

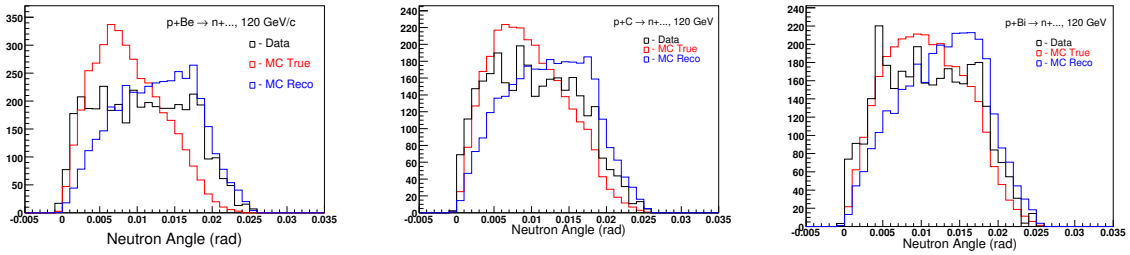

Figure 188: The neutron angular distributions for data and MC superimposed: from p+Be (left), p+C (middle) and p+Bi (right) interactions, respectively. The proton beam momentum is 120 GeV/c.

The neutron angular distributions, true vs reco MC comparison, from p+C and p+Bi interactions at 120 GeV/c are shown in Figure 189.

Unmatched shower position distributions in X-view from p+C and p+Bi interactions at 120 GeV/c are shown in Figure 190.

Unmatched shower position distributions in Y-view from p+C and p+Bi interactions at 120 GeV/c are shown in Figure 191.

Unmatched shower width distributions in X-view from p+C and p+Bi interactions at 120 GeV/c are shown in Figure 192.

Unmatched shower width distributions in Y-view from p+C and p+Bi interactions

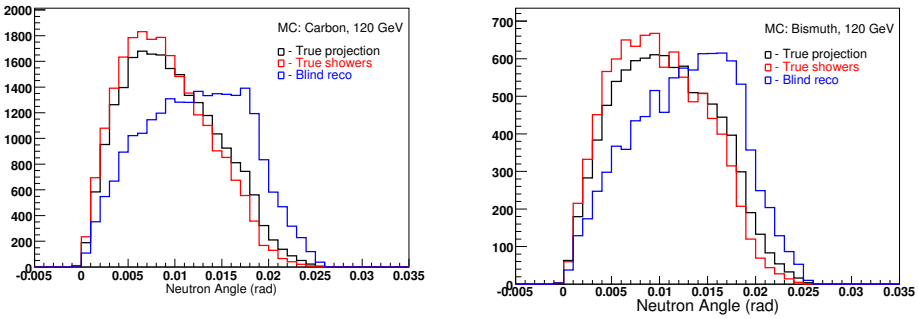

Figure 189: The neutron angular distributions, true vs reco MC comparison, from p+C and p+Bi interactions at 120 GeV/c. Fraction of neutrons that have a shower matched with projection = 23%.

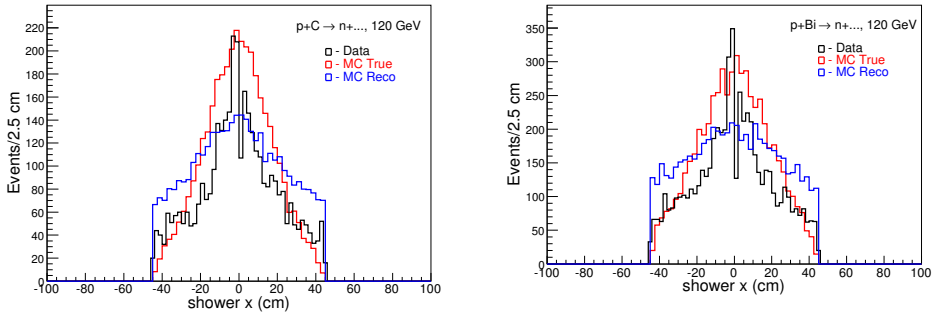

Figure 190: Unmatched shower position distributions in X-view from p+C and p+Bi interactions at 120 GeV/c

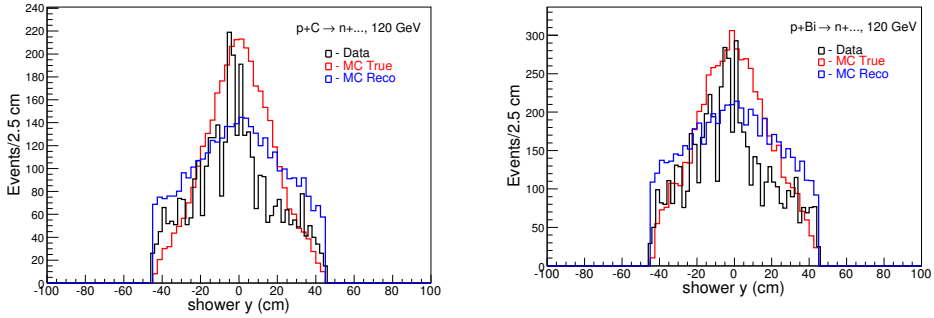

Figure 191: Unmatched shower position distributions in Y-view from p+C and p+Bi interactions at 120 GeV/c

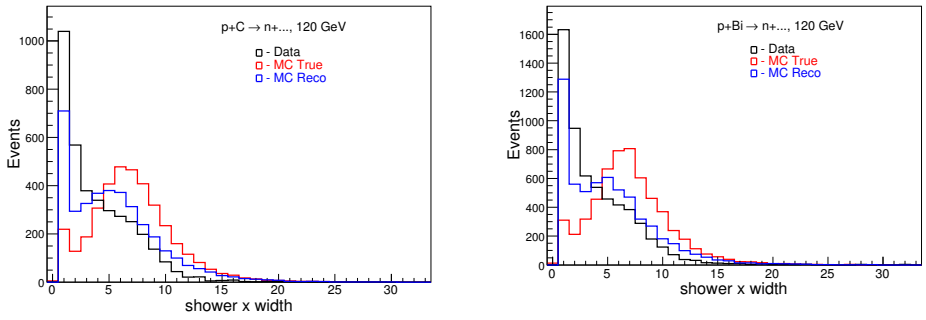

Figure 192: Unmatched shower width distributions in X-view from p+C and p+Bi interactions at 120 GeV/c

at 120 GeV/c are shown in Figure 193.

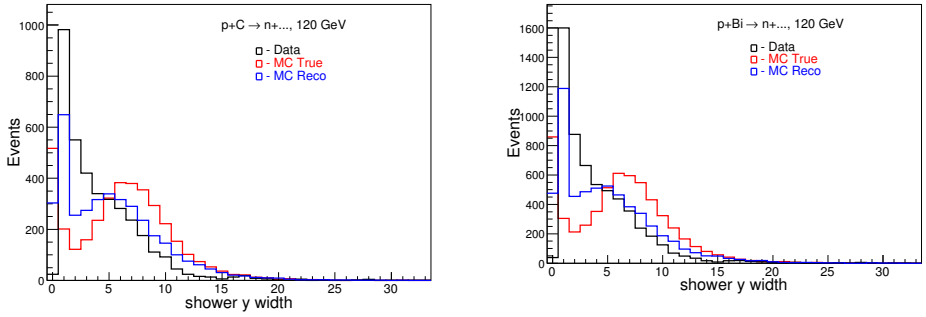

Figure 193: Unmatched shower width distributions in Y-view from p+C and p+Bi interactions at 120 GeV/c

Unmatched shower energy fractions, EMCAL/HCAL ratio, distributions from p+C and p+Bi interactions at 120 GeV/c are shown in Figure 194.

Unmatched shower energy fractions, EMCAL/HCAL ratio, distributions from p+C and p+Bi interactions at 120 GeV/c are shown in Figure 195.

Unmatched shower longitudinal profile in EMCal from p+C and p+Bi interactions at 120 GeV/c are shown in Figure 196.

23 Conclusion

We have performed...

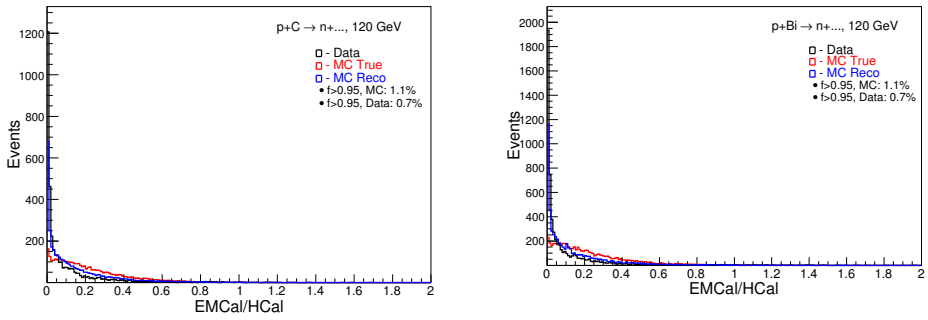

Figure 194: Unmatched shower energy fractions, EMCAL/HCAL ratio, distributions from p+C and p+Bi interactions at 120 GeV/c

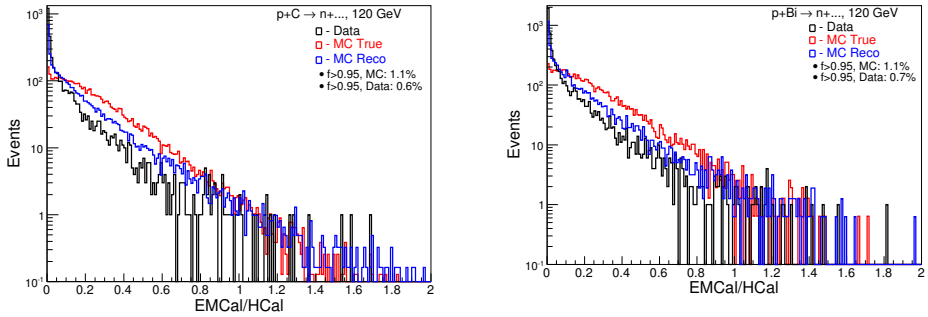

Figure 195: Unmatched shower energy fractions, EMCAL/HCAL ratio, distributions from p+C and p+Bi interactions at 120 GeV/c

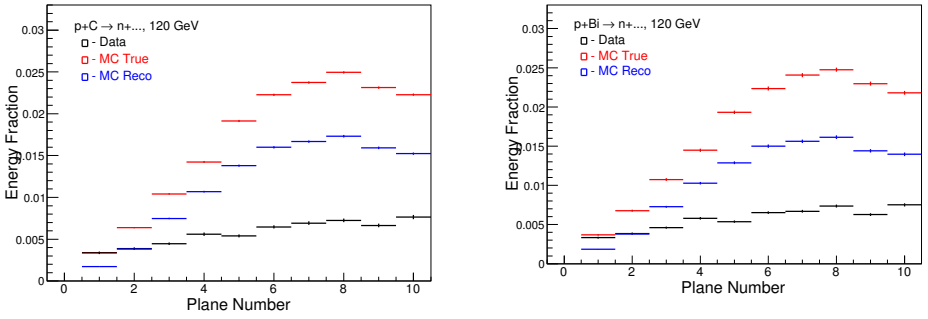

Figure 196: Unmatched shower longitudinal profile in EMCal from p+C and p+Bi interactions at 120 GeV/c

References

[1] T.S.Nigmanov et al. Electromagnetic and Hadron calorimeters in the MIPP experiment. NIM A 598 (2009) 394-399.

[2] T.Anticic at al. Inclusive production of protons, anti-protons and neutrons in p+p collisions at 158 GeV/c beam momentum. The NA49 Collaboration. arXiv:0904.2708v1 [hep-ex] 17 Apr 2009.

[3] Holger Meyer, MIPP software analysis meeting 3-27-09, page 8

[4] Jon Paley, MIPP software library - add summaries of unmatched segment tracks to DST., Dec., 2008.

[5] K.K. Gudima, S.G. Mashnik, and A.J. Sierk, User Manual for the Code LAQGSM, LANL Report LA-UR-01-6804, Los Alamos, 2001.

[6] S.G. Mashnik, K.K. Gudima, R.E. Prael, A.J. Sierk, M.I. Baznat, and N.V. Mokhov, EM03.03 and LAQGSM03.03 Event Generators for the MCNP6, MCNPX, and MARS15 Transport Codes,Invited lectures presented at the Joint ICTP-IAEA Advanced Workshop on Model Codes for Spallation Reactions, February 4, 2008, ICTP, Trieste, Italy, LA-UR-08-2931, Los Alamos (2008); E-print: arXiv:0805.0751v2 [nucl-th]; IAEA Report INDC(NDS)-0530, Distr. SC, Vienna, Austria, August 2008, p.51.

[7] S.G. Mashnik, K.K. Gudima, N.V. Mokhov, and R.E. Prael, AQGSM03.03 Upgrade and Its Validation,LANL Research Note X-3-RN(U)07-15, August 27, 2007; LANL Report LA-UR-07-6198, E-print: arXiv:0709.173.

Appendix

A Transverse position cut for the liquid hydrogen data

Figure 197 shows the longitudinal vertex position distributions for the interactions with the empty cryo target using π, K and p beam and interaction triggers.

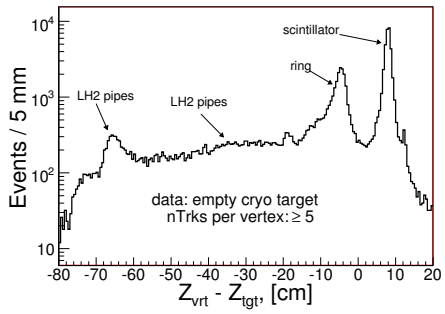

Figure 197: The longitudinal vertex position distributions for the interactions with the empty cryo target using π, K and p beam and interaction triggers

Figure 198 shows the transverse vertex position distributions for the interactions with the empty cryo target using π, K and p beam and interaction triggers.

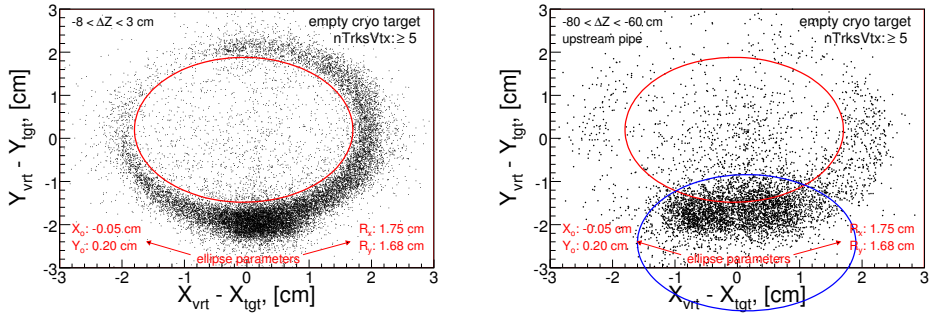

Figure 198: The transverse vertex position distributions for the interactions with the empty cryo target using π, K and p beam and interaction triggers. Plots made with different ΔZ_{vtx} cuts: -8< ΔZ_{vtx} <3 cm for the left plot which reflects the transverse slice of the hydrogen flask and -80< ΔZ_{vtx} <-60 cm for the right plot which represents the transverse slice at region of where a most upstream location of the transport pipes is appears to be close to the beam line.

Left plot on Figure 198 allow to see the interactions with the supporting aluminum(?) ring which holds the target flask. An ellipse (red circle) illustrates the

area which can be account as a liquid hydrogen volume. Right plot indicates that the liquid hydrogen transport pipes some how entering to the liquid hydrogen volume, see an overlapped area by both ellipses. The beam track transverse position cut would be: use those data points which is within the red ellipse and NOT within blue one.

The beam transverse positions at Z=Z_{tgt} shown in Figure 199 for 58 GeV/c liquid hydrogen and empty cryo target data. The red lines show what was selected as hydrogen flask center in horizontal and vertical plane, respectively. Their were defined from the empty cryo studies.

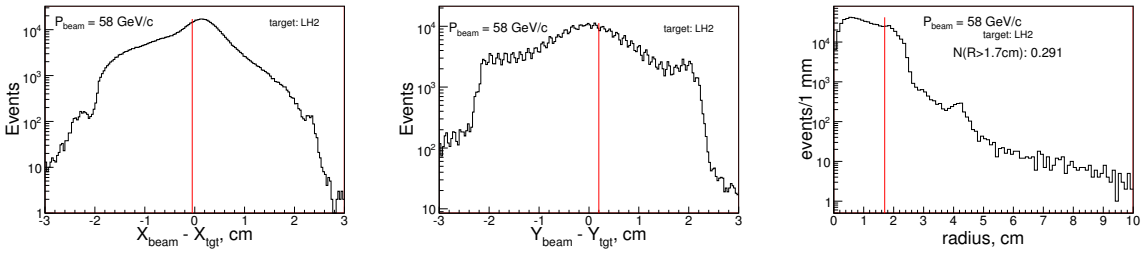

Figure 199: The beam track position distributions at Z of liquid hydrogen target center using 58 GeV/c particles. The red lines on left and in middle plots illustrate the horizontal and vertical centers of hydrogen flask. The right plot shows the distance between target center and the position of the particle distribution. The red line there shows the ellipse radius cut position.

B Calorimeter's Energy Scale in data

B.1 Projected neutron energy losses in EMCAL

The projected neutron energy losses in EMCAL was estimated with an assumption that it is the same as proton losses. Figure 200 shows the proton energy losses in calorimeters and momentum distribution of 20 GeV/c beam tracks.

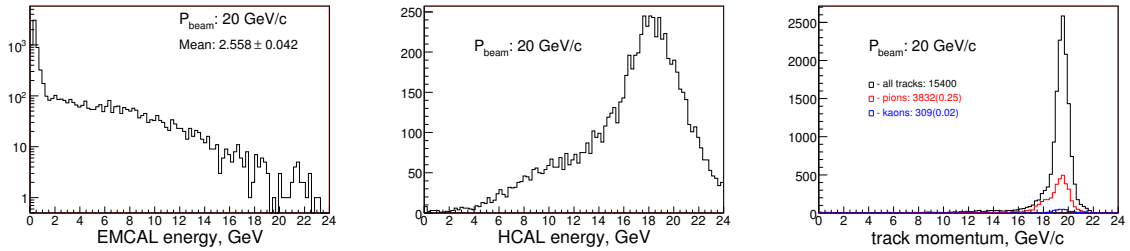

Figure 200: The proton energy losses in calorimeters and momentum distribution of 20 GeV/c beam tracks. Requirements: proton beam trigger, single track, LH2 target. The track momentum plot (left) shows the pion (red) and kaon (blue) contamination in proton beam which was identified by RICH detector.

Figure 201 shows the proton energy losses in calorimeters and momentum distribution of 58 GeV/c beam tracks.

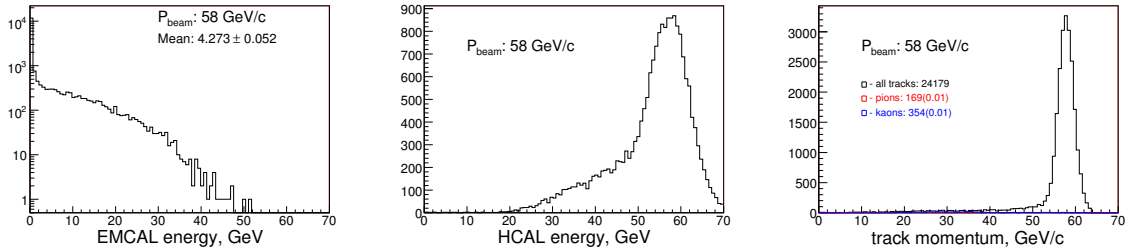

Figure 201: The proton energy losses in calorimeters and momentum distribution of 58 GeV/c beam tracks. Requirements: proton beam trigger, single track, U target

Figure 202 shows the proton energy losses in calorimeters and momentum distribution of 84 GeV/c beam tracks.

Figure 203 shows the proton energy losses in calorimeters and momentum distribution of 120 GeV/c beam tracks.

Figure 204 shows the proton energy mean losses in EMCAL as the function of the proton momentum.

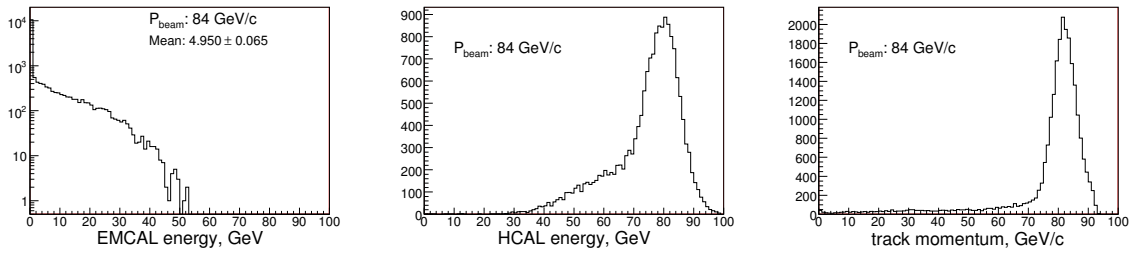

Figure 202: The proton energy losses in calorimeters and momentum distribution of 84 GeV/c beam tracks. Requirements: proton beam trigger, single track, LH2 target

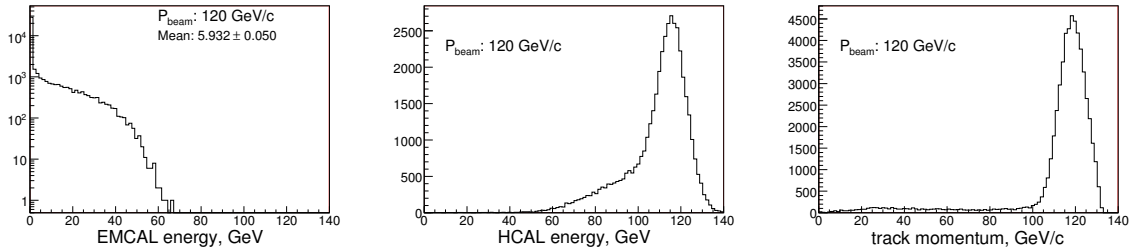

Figure 203: The proton energy losses in calorimeters and momentum distribution of 120 GeV/c beam tracks. Requirements: proton beam trigger, single track, Bi target

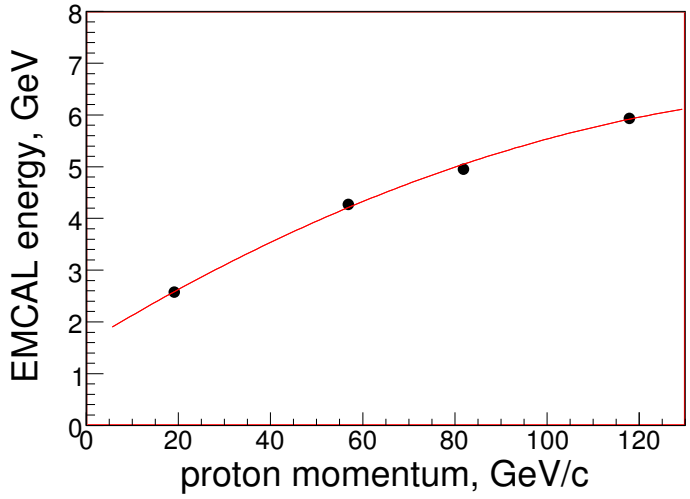

Figure 204: The proton energy mean losses in EMCAL as the function of the proton momentum. Red curve is fit with 2-nd order polynomial. Fit parameters: a free parameter is 1.60±0.08, linear term is 0.055±0.003 and quadratic term is -0.00015±0.00002.

B.2 How well the Calorimeter's energy scale?

How well the neutron/calorimeters energy scale was tuned can be viewed through the E_{e+h}/p_{trk} ratio. If tuning was done correctly, then this ratio would be equal to 1. Figure 205 shows the E_{e+h}/p_{trk} ratio distributions for 20 and 58 GeV/c proton beams.

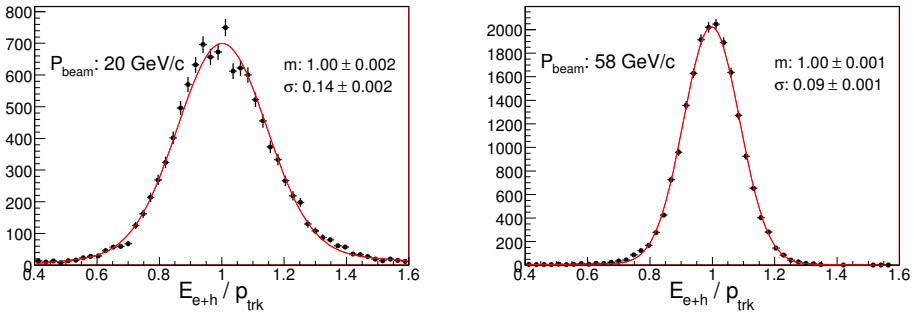

Figure 205: The E_{e+h}/p_{trk} ratio distributions for 20 and 58 GeV/c proton beams. The captions in plots indicates that the mean values of the E_{e+h}/p_{trk} are equal to 1 within given uncertainties.

Figure 206 shows the E_{e+h}/p_{trk} ratio distributions for 84 and 120 GeV/c proton beams.

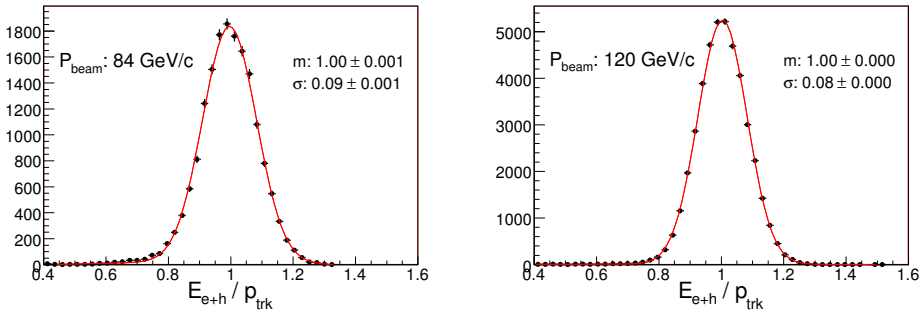

Figure 206: The E_{e+h}/p_{trk} ratio distributions for 84 and 120 GeV/c proton beams. The captions in plots indicates that the mean values of the E_{e+h}/p_{trk} are equal to 1 within given uncertainties.

B.3 Pion contamination in proton beam triggers

The track momentum plot on 20 GeV/c data shows about 25% of pion contamination in proton beam which was identified by RICH detector, see Figure 200. What the beam Cerenkov detectors tells about the pions?

C Calorimeter's energy scale in MC

C.1 Updated EMCal gas material

Figure 207 shows the EMCal and HCAL responses and E_{e+h}/E_p ratio distribution for the beam momentum protons both data and MC using pC interactions at 58 GeV/c. EMCal gas material in MC has been updated.

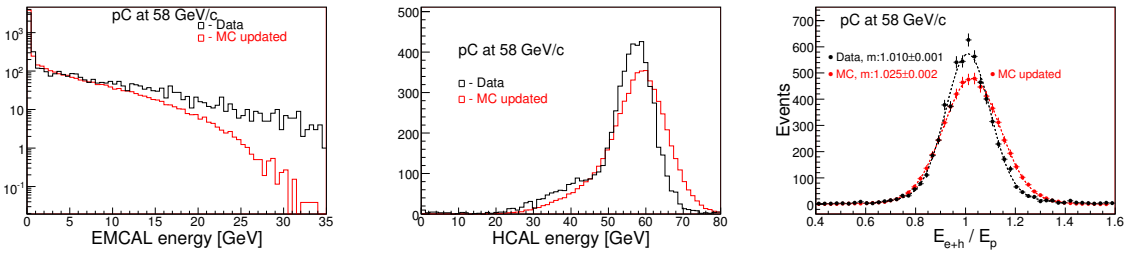

Figure 207: The EMCal and HCAL responses and E_{e+h}/E_p ratio distribution for the beam momentum protons both data and MC using pC interactions at 58 GeV/c. EMCal gas material in MC has been updated.

Figure 208 shows the EMCal and HCAL responses and E_{e+h}/E_p ratio distribution for the beam momentum protons both data and MC using pC interactions at 120 GeV/c. EMCal gas material in MC has been updated.

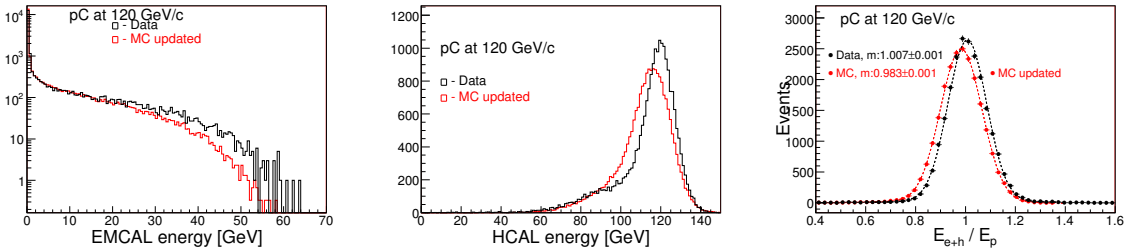

Figure 208: The EMCal and HCAL responses and E_{e+h}/E_p ratio distribution for the beam momentum protons both data and MC using pC interactions at 120 GeV/c. EMCal gas material in MC has been updated.

C.2 With previous EMCal gas material assignment

Figure 209 shows the EMCal and HCAL responses and E_{e+h}/E_p ratio distribution for the beam momentum protons both data and MC using pC interactions at 58 GeV/c. Previous EMCal gas material assignment.

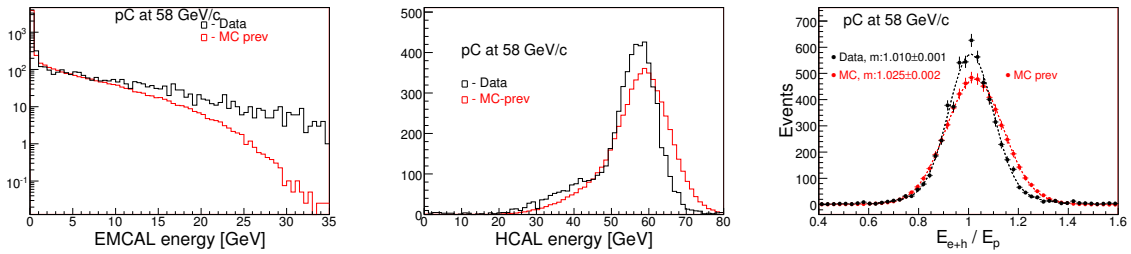

Figure 209: The EMCal and HCAL responses and E_{e+h}/E_p ratio distribution for the beam momentum protons both data and MC using pC interactions at 58 GeV/c. Previous EMCal gas material assignment.

Figure 210 shows the EMCal and HCAL responses and E_{e+h}/E_p ratio distribution for the beam momentum protons both data and MC using pC interactions at 120 GeV/c. Previous EMCal gas material assignment

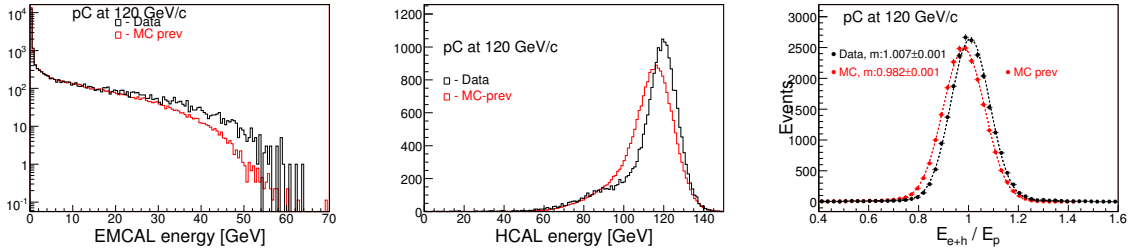

Figure 210: The EMCal and HCAL responses and E_{e+h}/E_p ratio distribution for the beam momentum protons both data and MC using pC interactions at 120 GeV/c. Previous EMCal gas material assignment

Table 59 summarizes the calorimeter's energy scale for previous and updated versions of Monte Carlo.

	previous MC	updated MC
C-58 GeV/c	+0.025	+0.025
C-120 GeV/c	-0.018	-0.017

Table 59: Summary of the calorimeter's energy scale offsets for previous and updated versions of Monte Carlo.

Figure 211 shows the E_{e+h}/E_p ratio distributions with MC HCAL energy scale corrected. Updated EMCal gas material assignment.

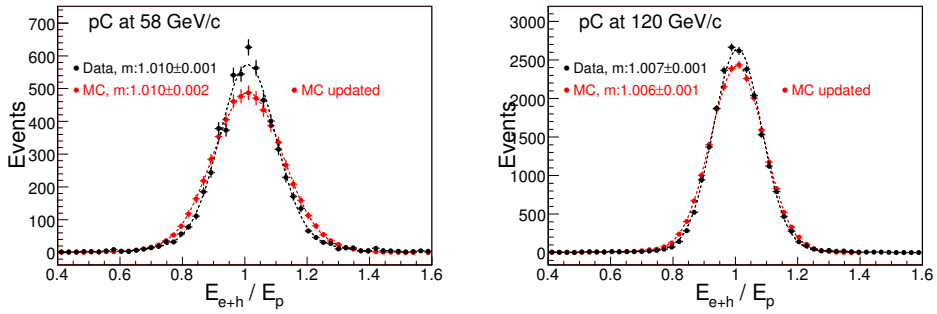

Figure 211: E_{e+h}/E_p ratio distributions with MC HCAL energy scale corrected. Updated EMCal gas material assignment.

C.3 Neutron fake rate variation due to EMCal gas update

Figure 212 shows the neutron fake rates as a function of the neutron momentum for pC interactions at 58 and 120 GeV/c. EMCal gas material has been updated.

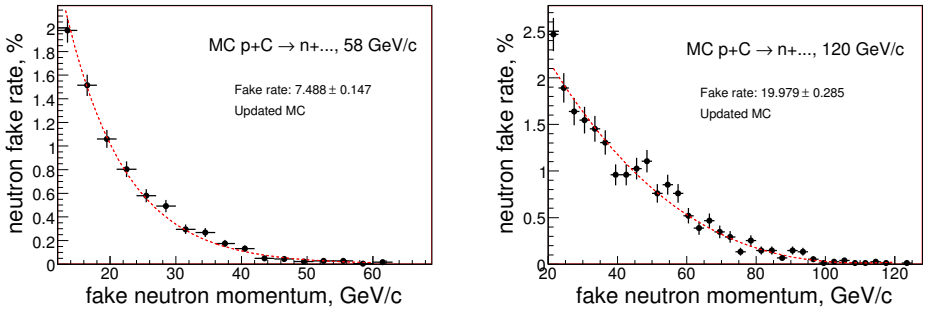

Figure 212: The neutron fake rates as a function of the neutron momentum for pC interactions at 58 (left) and 120 (right) GeV/c. EMCal gas material has been updated

Figure 213 shows the neutron fake rates as a function of the neutron momentum for pBi interactions at 58 and 120 GeV/c. EMCal gas material has been updated.

Table 60 summarizes the neutron fake rate variation from the previous to updated EMCal gas assognements in MC.

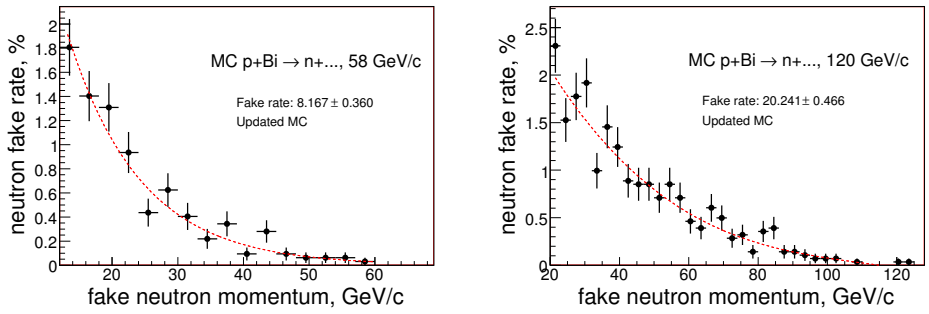

Figure 213: The neutron fake rates as a function of the neutron momentum for pBi interactions at 58 (left) and 120 (right) GeV/c. EMCal gas material has been updated.

	previous MC	updated MC
C-58 GeV/c	6.65±0.07	7.49±0.15
Bi-58 GeV/c	10.08±0.18	8.17±0.36
C-120 GeV/c	16.91±0.09	19.98±0.29
Bi-120 GeV/c	21.76±0.19	20.24±0.47

Table 60: Summary of the neutron fake rate variations from the previous to updated EMCal gas assignments in Monte Carlo. Fake rates are in %.

D Track Multiplicity for Data: proton interactions

The trigger efficiency is a function depending on the track multiplicity and the trigger scintillator acceptance. Due to of that we will consider the multiplicity for those tracks, which passed through the scintillator.

Below we present the charged track multiplicity for different targets and beam momenta using the transverse momentum cut as Δp_T >0.15 GeV/c. Figure 214 shows the charged track multiplicity for p+p interactions at 58 GeV/c for both target-in and target-out (on left) and the case when target-out subtraction is applied (on right).

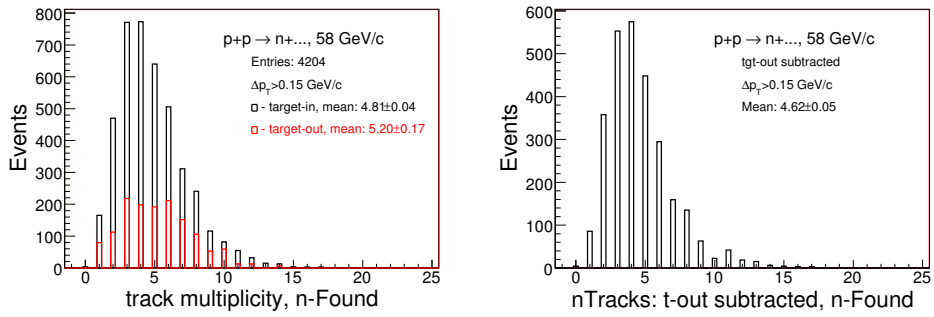

Figure 214: The charged track multiplicity for p+p interactions at 58 GeV/c for both target-in and target-out (on left) and the case when target-out subtraction is applied (on right). Requirements: all events passed the neutron selection cuts.

Figure 215 shows the charged track multiplicity for p+Be interactions at 58 GeV/c for both target-in and target-out (on left) and the case when target-out subtraction is applied (on right).

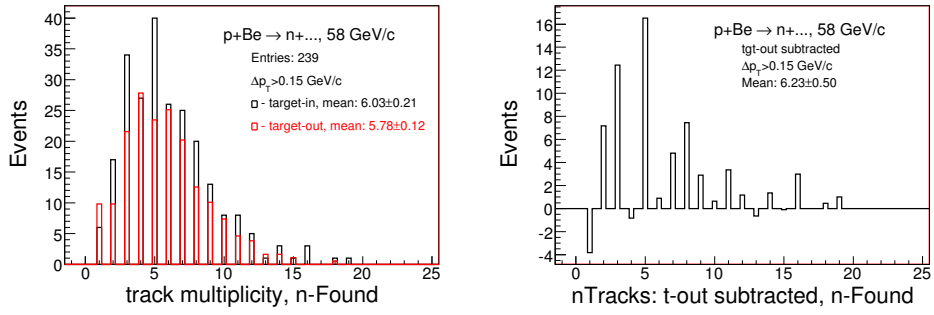

Figure 215: The charged track multiplicity for p+Be interactions at 58 GeV/c for both target-in and target-out (on left) and the case when target-out subtraction is applied (on right). Requirements: all events passed the neutron selection cuts.

Figure 216 shows the charged track multiplicity for p+C interactions at 58 GeV/c for both target-in and target-out (on left) and the case when target-out subtraction

is applied (on right).

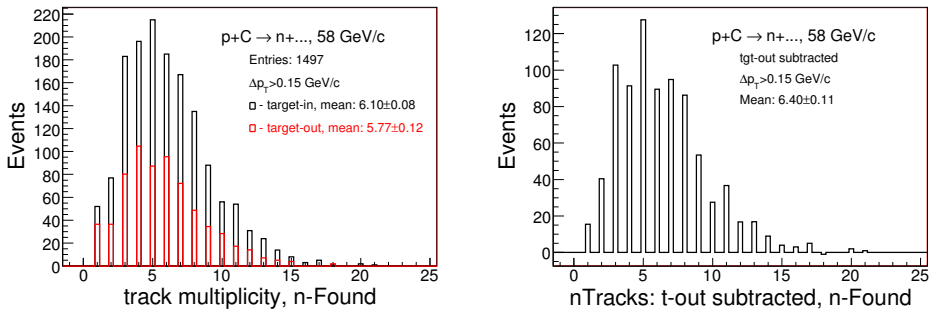

Figure 216: The charged track multiplicity for p+C interactions at 58 GeV/c for both target-in and target-out (on left) and the case when target-out subtraction is applied (on right). Requirements: all events passed the neutron selection cuts.

Figure 217 shows the charged track multiplicity for p+Bi interactions at 58 GeV/c for both target-in and target-out (on left) and the case when target-out subtraction is applied (on right).

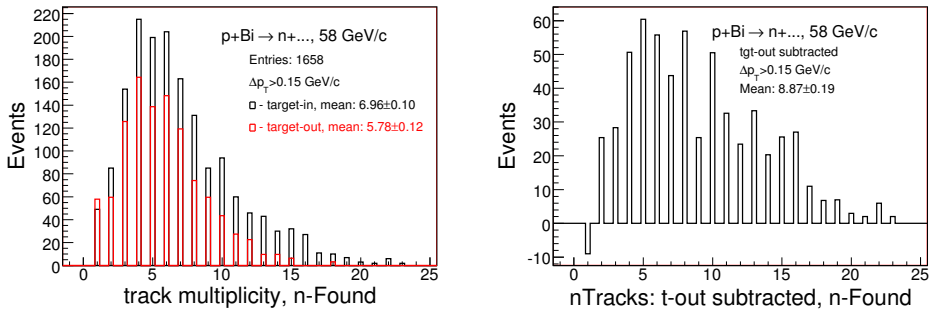

Figure 217: The charged track multiplicity for p+Bi interactions at 58 GeV/c for both target-in and target-out (on left) and the case when target-out subtraction is applied (on right). Requirements: all events passed the neutron selection cuts.

Figure 218 shows the charged track multiplicity for p+U interactions at 58 GeV/c for both target-in and target-out (on left) and the case when target-out subtraction is applied (on right).

Figure 219 shows the charged track multiplicity for p+p interactions at 84 GeV/c for both target-in and target-out (on left) and the case when target-out subtraction is applied (on right).

Figure 220 shows the charged track multiplicity for p+Be interactions at 120 GeV/c for both target-in and target-out (on left) and the case when target-out subtraction is applied (on right).

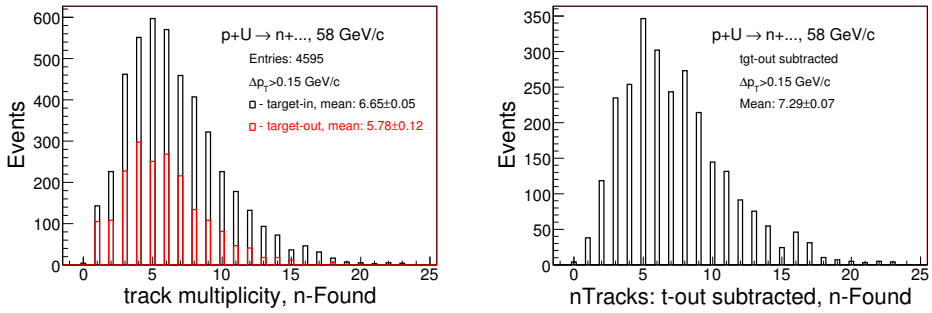

Figure 218: The charged track multiplicity for p+U interactions at 58 GeV/c for both target-in and target-out (on left) and the case when target-out subtraction is applied (on right). Requirements: all events passed the neutron selection cuts.

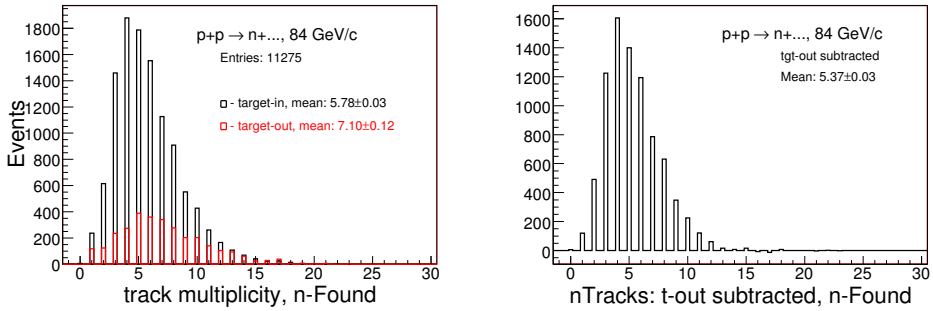

Figure 219: The charged track multiplicity for p+p interactions at 84 GeV/c for both target-in and target-out (on left) and the case when target-out subtraction is applied (on right). Requirements: all events passed the neutron selection cuts.

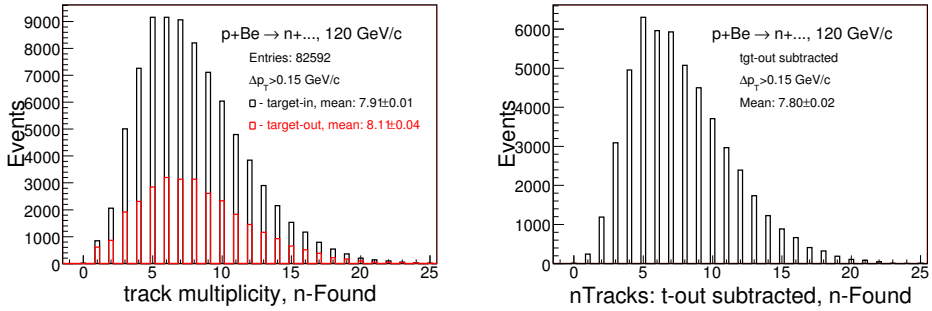

Figure 220: The charged track multiplicity for p+Be interactions at 120 GeV/c for both target-in and target-out (on left) and the case when target-out subtraction is applied (on right). Requirements: all events passed the neutron selection cuts.

Figure 221 shows the charged track multiplicity for p+C interactions at 120 GeV/c for both target-in and target-out (on left) and the case when target-out subtraction is applied (on right).

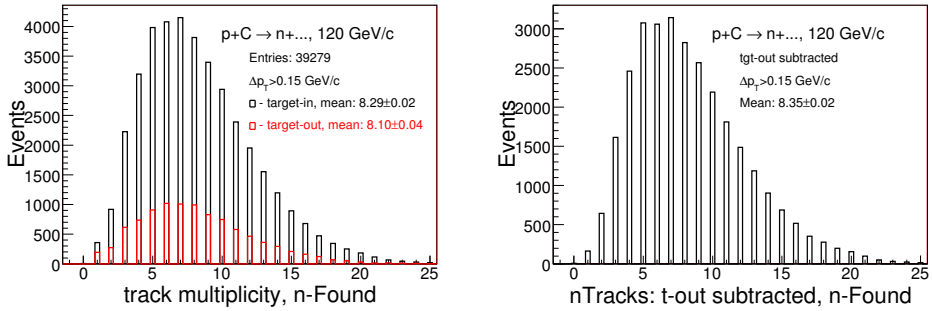

Figure 221: The charged track multiplicity for p+C interactions at 120 GeV/c for both target-in and target-out (on left) and the case when target-out subtraction is applied (on right). Requirements: all events passed the neutron selection cuts.

Figure 222 shows the charged track multiplicity for p+Bi interactions at 120 GeV/c for both target-in and target-out (on left) and the case when target-out subtraction is applied (on right).

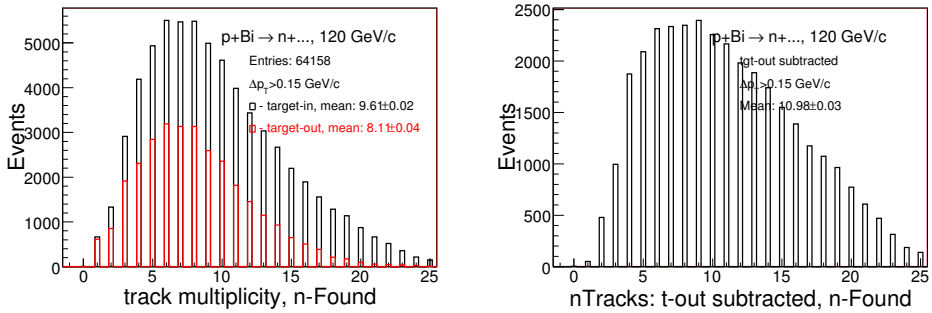

Figure 222: The charged track multiplicity for p+Bi interactions at 120 GeV/c for both target-in and target-out (on left) and the case when target-out subtraction is applied (on right). Requirements: all events passed the neutron selection cuts.

The charged track multiplicity for the proton interaction trigger data with SciHi is on are summarized in Table 61.

E Non-neutron multiplicities

Figure 223 shows the multiplicities for p+C at 58 GeV/c and at 120 GeV/c.

	target-in	target-out	Subtr.	beamTrig
H_2-58 GeV/c	4.81±0.04	5.20±0.17	4.62±0.04	4.6(5.1)±0.4
Be-58 GeV/c	6.03±0.08	5.78±0.12	6.23±0.32	8.7(8.1)±3.0
C-58 GeV/c	6.10±0.08	5.77±0.12	6.40±0.10	5.0(5.4)±1.7
Bi-58 GeV/c	6.96±0.10	5.78±0.12	8.87±0.20	7.6(6.8)±2.9
U-58 GeV/c	6.65±0.05	5.78±0.12	7.29±0.07	5.2(5.7)±0.5
H_2-84 GeV/c	5.78±0.03	7.10±0.12	5.37±0.03	3.7(5.5)±0.2
Be-120 GeV/c	7.91±0.01	8.11±0.04	7.80±0.02	7.1(7.2)±0.3
C-120 GeV/c	8.29±0.02	8.10±0.04	8.35±0.02	7.2(7.4)±0.4
Bi-120 GeV/c	9.61±0.02	8.10±0.04	10.98±0.03	8.5(10.1)±0.4

Table 61: The charged track multiplicity passing through the trigger scintillator using the proton interaction trigger data with SciHi is on. The multiplicities are shown for target-in, target-out and subtraction applied cases using the transverse momentum cut as Δp_T >0.15 GeV/c. Last column represents the multiplicities for the beam trigger without SciHi requirements. All events passed the neutron selection cuts.

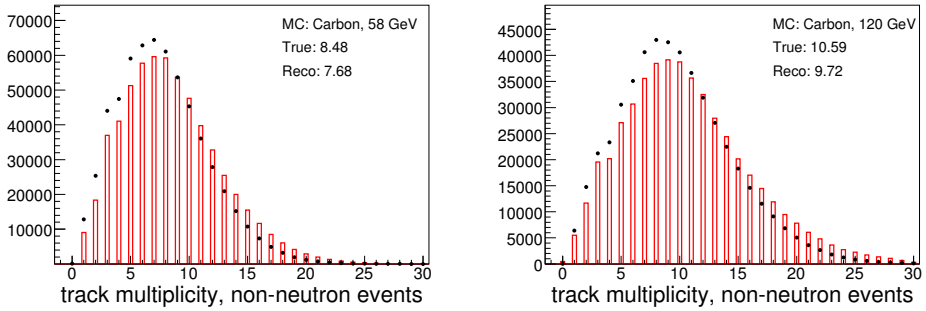

Figure 223: The multiplicities for p+C at 58 GeV/c (left) and at 120 GeV/c (right), respectively.

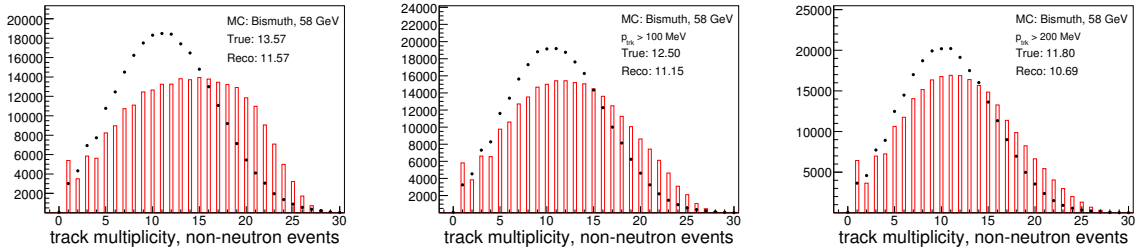

Figure 224: The multiplicities for p+Bi at 58 GeV/c interactions with different track momentum cut: 0 MeV/c (left), 100 MeV/c (middle) and 200 MeV/c (right), respectively.

Figure 224 shows the multiplicities for p+Bi at 58 GeV/c with different track momentum cut: 0 MeV/c, 100 MeV/c and 200 MeV/c.

Figure 225 shows the multiplicities for p+U at 58 GeV/c with different track momentum cut: 0 MeV/c, 100 MeV/c and 200 MeV/c.

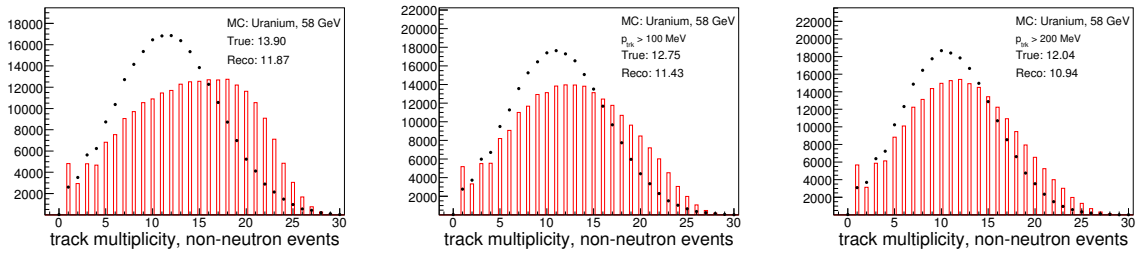

Figure 225: The multiplicities for p+U at 58 GeV/c interactions with different track momentum cut: 0 MeV/c (left), 100 MeV/c (middle) and 200 MeV/c (right), respectively.

Figure 226 shows the multiplicities for p+Bi at 120 GeV/c with different track momentum cut: 0 MeV/c, 100 MeV/c and 200 MeV/c.

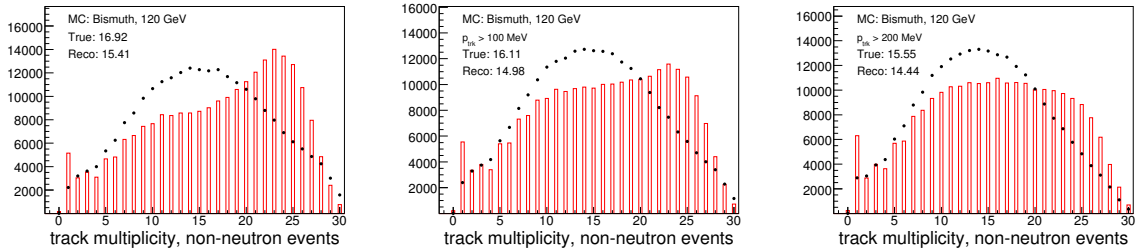

Figure 226: The multiplicities for p+Bi at 120 GeV/c interactions with different track momentum cut: 0 MeV/c (left), 100 MeV/c (middle) and 200 MeV/c (right), respectively.

The charged track multiplicities for the non-neutron samples are summarized in Table 62.

	True(Reco), 0 GeV/c	100 MeV/c	200 MeV/c
C-58 GeV/c	8.5 (7.7)	-	-
Bi-58 GeV/c	13.6 (11.6)	12.5 (11.1)	11.8 (10.7)
U-58 GeV/c	13.9 (11.9)	12.8 (11.4)	12.0 (10.9)
C-120 GeV/c	10.6 (9.7)	-	-
Bi-120 GeV/c	16.9 (15.4)	16.1 (15.0)	15.6 (14.4)

Table 62: The charged track multiplicities for the non-neutron samples with the different track momentum cuts: 0 MeV/c, 100 MeV/c and 200 MeV/c, respectively

F Neutral particles production positions and momenta distributions

Figure 227 illustrates the production positions in Z and momenta distributions of the neutrals in p+p interactions at 58 GeV/c.

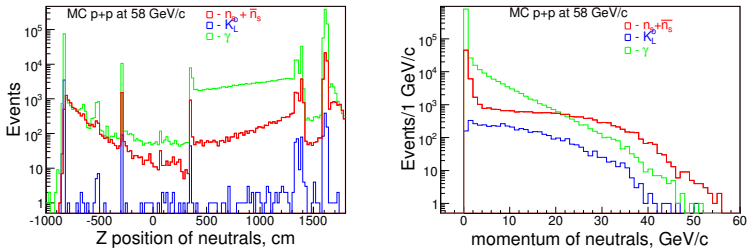

Figure 227: The production positions in Z and momenta distributions of the neutrals in p+p interactions at 58 GeV/c. Requirements: non-neutron events with trigger is on. Left plots illustrates the Z position distributions, where the neutrals were produced: Z=-830 is the primary target position, Z=-300 is ToF, Z=330 is the RICH front wall, Z=1330 is RICH end wall, Z=1650 is middle of EMCAL. Right plot: the truth momenta distributions of each neutrals.

Figure 228 illustrates the production positions in Z and momenta distributions of the neutrals in p+Be interactions at 58 GeV/c.

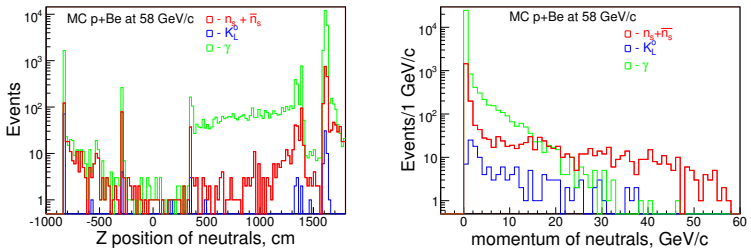

Figure 228: The production positions in Z and momenta distributions of the neutrals in p+Be interactions at 58 GeV/c. Requirements: non-neutron events with trigger is on. Left plots illustrates the Z position distributions, where the neutrals were produced. Right plot: the truth momentum distribution of each neutrals.

Figure 229 illustrates the production positions in Z and momenta distributions of the neutrals in p+C interactions at 58 GeV/c.

Figure 230 illustrates the production positions in Z and momenta distributions of the neutrals in p+Bi interactions at 58 GeV/c.

Figure 231 illustrates the production positions in Z and momenta distributions of the neutrals in p+U interactions at 58 GeV/c.

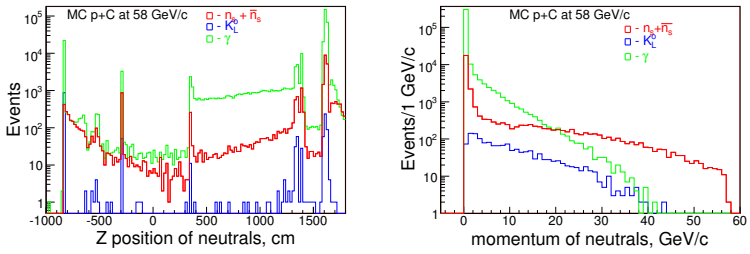

Figure 229: The production positions in Z and momenta distributions of the neutrals in p+C interactions at 58 GeV/c. Requirements: non-neutron events with trigger is on. Left plots illustrates the Z position distributions, where the neutrals were produced. Right plot: the truth momentum distribution of each neutrals.

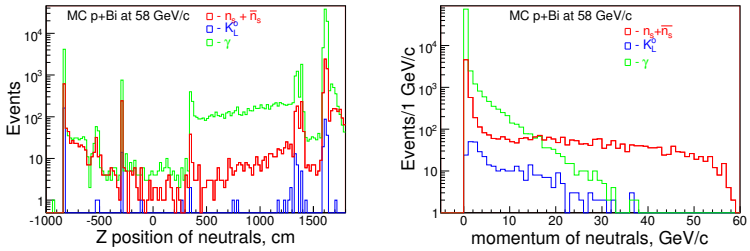

Figure 230: The production positions in Z and momenta distributions of the neutrals in p+Bi interactions at 58 GeV/c. Requirements: non-neutron events with trigger is on. Left plots illustrates the Z position distributions, where the neutrals were produced. Right plot: the truth momentum distribution of each neutrals.

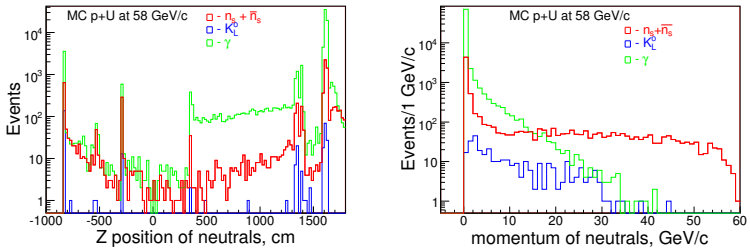

Figure 231: The production positions in Z and momenta distributions of the neutrals in p+U interactions at 58 GeV/c. Requirements: non-neutron events with trigger is on. Left plots illustrates the Z position distributions, where the neutrals were produced. Right plot: the truth momentum distribution of each neutrals.

Figure 232 illustrates the production positions in Z and momenta distributions of the neutrals in p+Be interactions at 120 GeV/c.

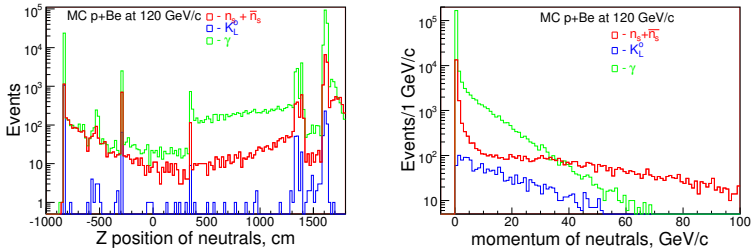

Figure 232: The production positions in Z and momenta distributions of the neutrals in p+Be interactions at 120 GeV/c. Requirements: non-neutron events with trigger is on. Left plots illustrates the Z position distributions, where the neutrals were produced. Right plot: the truth momentum distribution of each neutrals.

Figure 233 illustrates the production positions in Z and momenta distributions of the neutrals in p+C interactions at 120 GeV/c.

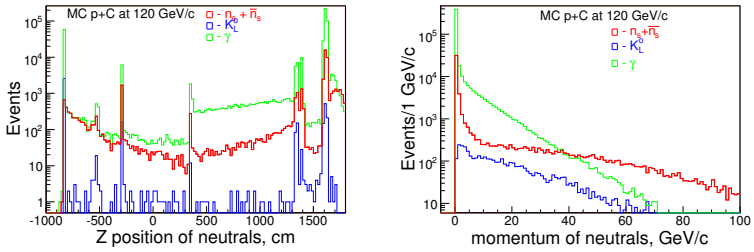

Figure 233: The production positions in Z and momenta distributions of the neutrals in p+C interactions at 120 GeV/c. Requirements: non-neutron events with trigger is on. Left plots illustrates the Z position distributions, where the neutrals were produced. Right plot: the truth momentum distribution of each neutrals.

Figure 234 illustrates the production positions in Z and momenta distributions of the neutrals in p+Bi interactions at 120 GeV/c.

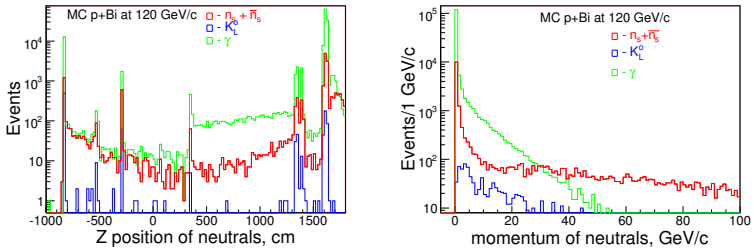

Figure 234: The production positions in Z and momenta distributions of the neutrals in p+Bi interactions at 120 GeV/c. Requirements: non-neutron events with trigger is on. Left plots illustrates the Z position distributions, where the neutrals were produced. Right plot: the truth momentum distribution of each neutrals.

G Neutron's raw spectrum: data vs MC

Below we compare data vs MC raw spectrum - when no any correction were applied. Figure 235 illustrates the comparison for p+A interactions at 58 GeV/c.

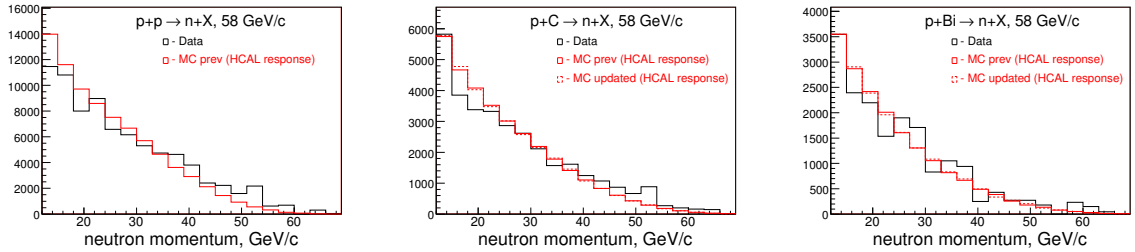

Figure 235: Comparison of the raw neutron spectrum, when no any correction were applied. Distributions are based on HCAL responses for p+A interactions at 58 GeV/c.

Figure 236 illustrates the comparison for p+A interactions at 84 and at 120 GeV/c.

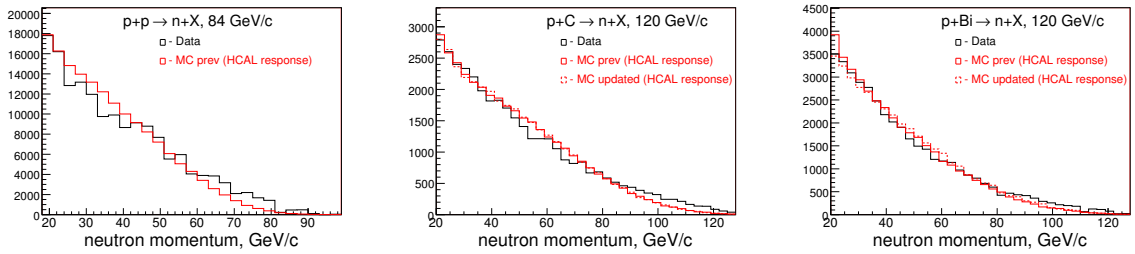

Figure 236: Comparison of the raw neutron spectrum, when no any correction were applied. Distributions are based on HCAL responses for p+A interactions at 84 and at 120 GeV/c.

We do not know what the true spectrum look like in data. But we see that the raw spectrum in MC is much differ from the true one. Why it so distorted? Because the neutron cross section in MC is relatively small in compare with the total inelastic cross section: Table 63 illustrates the comparison of the inelastic cross section fractions of the neutrons and non-neutrons.

H MC HCAL's responses for true neutrons

Figure 237 illustrates the set of neutron spectra: generated within calorimeter acceptance, reconstructed by HCAL using both: whole and only neutron MC samples for p+A interactions at 58 GeV/c.

	σ_{inel}	σ_n MC
H_2-58	31.0 mb	4.4 mb (0.14)
C-58	286 mb	29.0 mb (0.10)
Bi-58	1875 mb	123.7 mb (0.07)
H_2-84	31.4 mb	6.0 mb (0.19)
C-120	287 mb	53.0 mb (0.18)
Bi-120	1880 mb	273.5 mb (0.15)

Table 63: Comparison of the total inelastic and neutron cross sections. Major source of the backgrounds are the neutrals from the total inelastic processes.

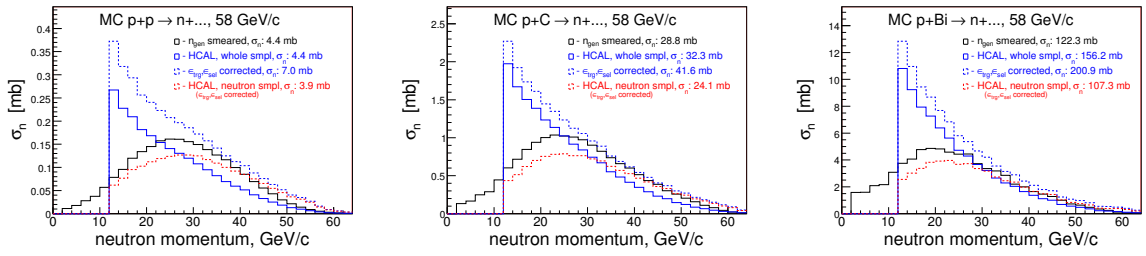

Figure 237: The set of neutron spectra: generated within calorimeter acceptance, reconstructed by HCAL using both: whole and only neutron MC samples for p+A interactions at 58 GeV/c.

Figure 238 illustrates the set of neutron spectra: generated within calorimeter acceptance, reconstructed by HCAL using both: whole and only neutron MC samples for p+A interactions at 58 and 120 GeV/c.

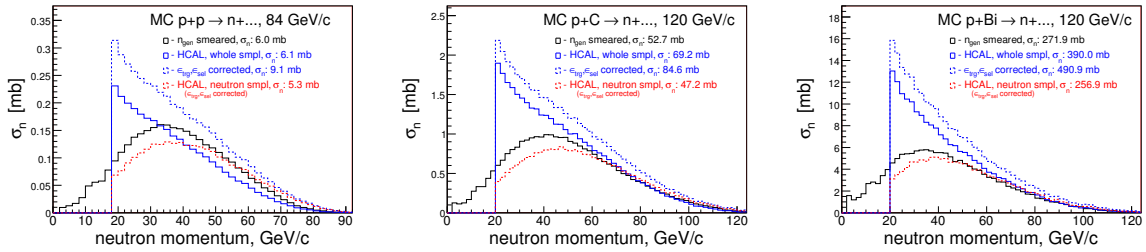

Figure 238: The set of neutron spectra: generated within calorimeter acceptance, reconstructed by HCAL using both: whole and only neutron MC samples for p+A interactions at 58 and 120 GeV/c.

Perspective background level illustrated in Table 64

	persp. backg.	prev. backgr.
H_2-58	0.37	0.08
C-58	0.31	0.07
Bi-58	0.39	0.10
H_2-84	0.34	0.12
C-120	0.38	0.17
Bi-120	0.45	0.22

Table 64: Perspective background level

I Study of MC neutron losses in setup material

Figure 239 illustrates the primary neutron production and interaction Z positions with the setup material and the resulting primary neutron spectrum in front face of EMCAL. The primary neutrons are from p+C at 58 GeV/c.

Figure 240 illustrates the primary neutron production and interaction Z positions with the setup material and the resulting primary neutron spectrum in front face of EMCAL. The primary neutrons are from p+Bi at 58 GeV/c.

Figure 241 illustrates the primary neutron production and interaction Z positions with the setup material and the resulting primary neutron spectrum in front face of EMCAL. The primary neutrons are from p+C at 120 GeV/c.

Figure 242 illustrates the primary neutron production and interaction Z positions with the setup material and the resulting primary neutron spectrum in front face of EMCAL. The primary neutrons are from p+Bi at 120 GeV/c.

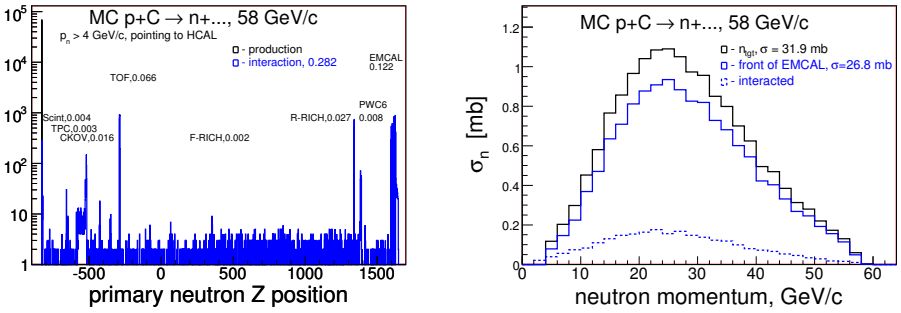

Figure 239: The primary neutron production/interaction Z positions with the setup material - left. Right plot illustrates the primary neutron spectrum from the target and resulting spectrum in front face of EMCAL. The primary neutrons are from p+C at 58 GeV/c.

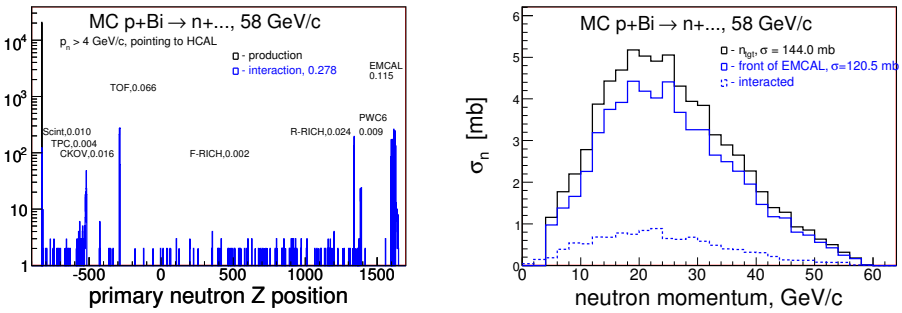

Figure 240: The primary neutron production/interaction Z positions with the setup material - left. Right plot illustrates the primary neutron spectrum from the target and resulting spectrum in front face of EMCAL. The primary neutrons are from p+C at 58 GeV/c.

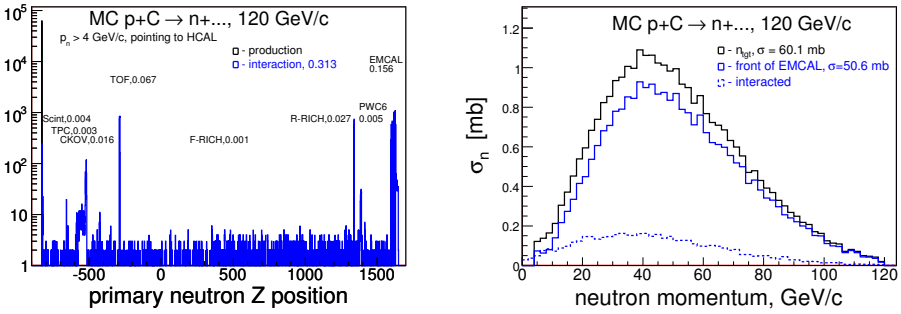

Figure 241: The primary neutron production/interaction Z positions with the setup material - left. Right plot illustrates the primary neutron spectrum from the target and resulting spectrum in front face of EMCAL. The primary neutrons are from p+C at 120 GeV/c.

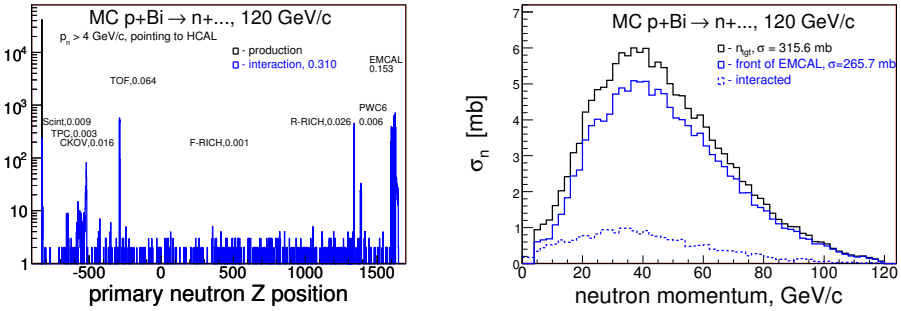

Figure 242: The primary neutron production/interaction Z positions with the setup material - left. Right plot illustrates the primary neutron spectrum from the target and resulting spectrum in front face of EMCAL. The primary neutrons are from p+C at 120 GeV/c.

Summary of the neutron losses due to interactions with the setup material illustrated in Table 65

	MC true	HCAL response
H_2-58	-	0.11
C-58	0.16	0.16
Bi-58	0.16	0.12
H_2-84	-	0.12
C-120	0.16	0.10
Bi-120	0.16	0.06

Table 65: An average neutron lost rate due to interactions with the setup material prior front of EMCAL. The estimate made in two ways: using the true neutrons and HCAL responses for the neutrons. Second estimate is bias to the trigger efficiency and possible backgrounds.

J MC neutron's true spectrum vs reconstructed proton spectrum

Figure 243 illustrates neutrons and proton spectrum from p+C p+Bi interactions at 58 GeV/c.

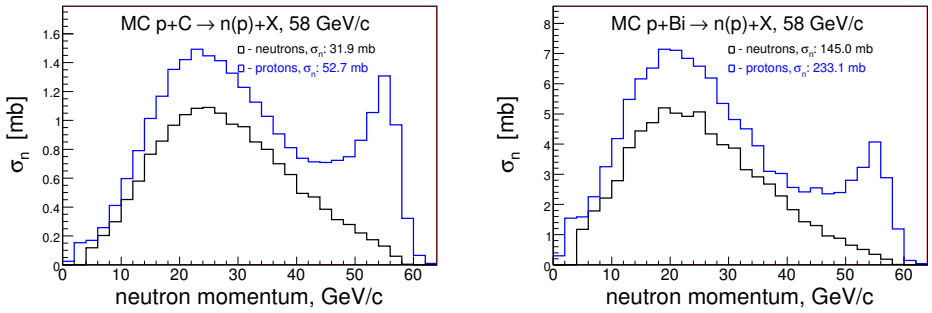

Figure 243: Neutrons and proton spectra from p+C (left) and p+Bi (right) interactions at 58 GeV/c. Neutrons - true, protons - reconstructed, id is based on MC truth info.

K Are elastic events in FLUKA generator?

What was found in first 100 events of p+p and p+C MC samples are summarized in Table 66.

	p+p,58 GeV/c	p+C 58 GeV/c
single proton exiting target	0	26
quasi elastic	0	4
hadron production	100	70

Table 66: